Università degli Studi di Milano-Bicocca

Facoltà di Scienze MM. FF. NN.
Ph.D. School in Nanostructures and Nanotechnologies
XXIV cycle 2009-2011

Density functional simulation of chalcogen doped silicon nanowires

Author: Guido Petretto
Matr. 039516

Advisor: Prof. Marco Fanciulli
Co-advisor: Dr. Alberto Debernardi
Coordinator: Prof. Gianfranco Pacchioni

Milano, January 26th 2012

Contents

Introduction

Nanoscience and nanotechnology are active and innovative fields of research that deal with the physical, chemical and biological properties of nanostructured materials. Their interest arises from the large variety of different structures that can be produced with such small sizes, each characterized by distinctive properties governed by the laws of quantum mechanics. The concrete possibility of producing and studying this kind of systems in a controlled way has opened the road to a lot of experimental and theoretical work, with the additional advantage that their results can be obtained on systems of the same size. *Ab-initio* calculations can thus provide a strong support for predicting and explaining the observed phenomena. This work follows this path, since it is performed in the framework of the ELIOS ("Elettronica a livello atomico in nanostrutture di silicio") project, founded by Fondazione Cariplo, which encompasses simulation, realization and functional characterization activities of silicon nanowires.

The aim of this thesis is to provide further insight in the understanding of the electronic properties of doped silicon nanowires by means of density functional simulations. In particular we have focused on chalcogens as substitutional defects inside the nanowire. The most important and original result concerns the calculation of hyperfine parameters for nanowires of different sizes and orientations, and with the defect in different positions with respect to the cross section of the nanowire. Based on our results, we have shown that hyperfine interactions increase at small diameters, as long as the nanowire is large enough to prevent surface distortion which modifies the symmetry of the donor wavefunction. Moreover, surface effects lead to strong differences in the hyperfine parameters depending on the chalcogen location inside the nanowire, allowing the identification of impurity site on the basis of the electron paramagnetic resonance spectra.

The rest of the thesis is organized as follows. Chapter 1 introduces the definition and basic properties of nanowires both from experimental and theoretical points of view. In Chapter 2 we give a brief overview of the methodologies and approximations employed in our work, along with our tests on the configuration parameters. Chapter 3 contains our results about pristine nanowires, illustrating the dependence of electronic properties not only on the size and orientation of the nanowires, but also on the presence or absence of surface reconstruction. In Chapter 4 we study the properties of chalcogen doped nanowires. We discuss the dopants distribution in the nanowires based on the formation energies that we have obtained from our simulations. Moreover, since the hyperfine parameters for chalcogen defects are non zero only in a singly ionized state, we verify the possibility to achieve this charge state. Finally, in Chapter 5 we present our results about the hyperfine structure of

the defects, highlighting the peculiar behaviour that we have observed in our silicon nanowires. Here, besides the comparison of hyperfine parameters for different nanowires structural properties and defect positions, we show their dependence on the strain of the system.

Chapter 1

Nanowires

A nanowire is usually defined as a one dimensional nanostructure with a diameter smaller than 100 nm. The possibility to shrink the dimension of semiconductor systems below this value has stimulated great interest towards nanowires and in particular semiconductor nanowires. Bulk semiconductors have dominated the industrial applications but with the progressive reduction of device size, nanostructures are gaining more and more importance in industry and research. In this race to the scaling down of the electronic components, semiconductor nanowires have been proposed as promising candidates for many applications, e.g. as interconnection in assembling nanoscale electron device, but also for thermoelectric and biological applications. In this chapter we review some basic properties of nanowires, and the results that have been obtained experimentally and theoretically, with a special care towards silicon nanowires.

1.1 Synthesis of silicon nanowires

The fabrication of nanowires is a challenging task that has been tackled in many ways and with different techniques. Nowadays, the methods for the production of silicon nanowires can be divided in two approaches: top-down and bottom-up. The former is based on the sequential decrease of object size by means of mechanical or chemical processing. The latter includes different procedures for the growth of nanowire adding individual atoms to build the final structure.

Here we want to outline the assembly procedure for these two approaches, focusing on the vapor-liquid-solid (VLS) deposition, which is one of the most successful techniques, because the nanowires produced in this way allow a more direct comparison with our simulations.

1.1.1 Top-down: Lithographic pattering

The top-down approach in general starts from a silicon wafer, where a thin layer of a resist will be spread. In this case a silicon on insulator (SOI) wafer can be suitable, having a buried etch stopping layer [1]. Depending on its properties, the resist can then be patterned with the aid of a mask through the exposure to an electron beam (electron-beam lithography) or UV-light (photolithography). At this point the resist can be developed with a suitable chemical agent, leaving a layer

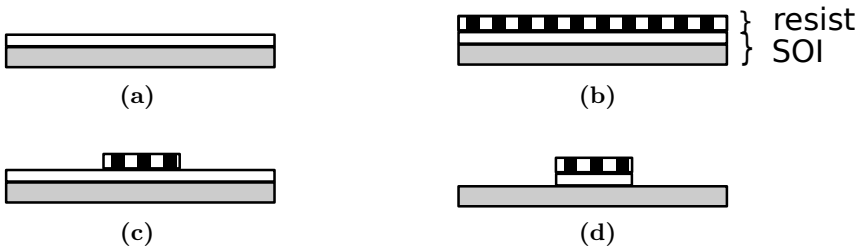

Figure 1.1: Schematic representation of the top-down process for the fabrication of silicon nanowires. The four steps refer to (a) clean SOI wafer, (b) resist deposition, (c) resist patterning and development, (d) etching process. The grey and white layer are the SOI wafer, while the dashed layer represents the resist.

of the patterned resist. The following etching process removes the silicon from the wafer surface, except for the area covered by the resist. In this way the mask can be transferred to the surface of the wafer. These steps are sketched in Figure 1.1.

The advantage of the nanowires produced with this technique is that contacts and gates can be applied easily on them, since their position can be determined thanks to appropriate alignment markers patterned on the sample. This is important in light of possible system integration. On the other hand, the possibility of scaling down the sizes relies on the ability of performing high resolution lithography and actually the size of top-down fabricated nanowire cannot be pushed down below 10 nm. A further reduction in size can be obtained through oxidation processes, but this can be done at the price of a degradation in size and shape control.

1.1.2 Bottom-up: vapor-liquid-solid growth

Bottom-up techniques include oxide-assisted growth (OAG), solution-based synthesis and VLS growth [2, 3], but the last one is the most well-established and widely used. VLS growth process can be broadly described as in Figure 1.2. As a first step, a droplet of a metallic catalyst (e.g. a gold nanoparticle) is deposited on a silicon substrate, next the temperature is raised in order to form a Au-Si alloy and the sample is then exposed to a silicon precursor (e.g. $SiCl_4$ or SiH_4). As a consequence, silicon atoms are adsorbed in the Au-Si droplet, bringing it in a supersaturation state, which induces silicon crystallization at the liquid-solid interface. The result is a vertical silicon nanowire with the catalyst droplet on the top of it.

The advantage of VLS growth over top-down approach is that it can produce silicon nanowires with controlled size and diameter ranging from few nm [4] to about 100 nm. The downside is that it can be hard to contact just a single nanowire and some unwanted effects can show during growth process, like, for example, a tapering of the nanowire due to the possible vapor-solid transition at the surface.

As stated above, the nanowires synthesized with these procedure can be more suitable to compare with our simulations, based on the fact that we use hydrogen atoms to passivate dangling bonds. In fact, not only we can find hydrogen passivated nanowire if SiH_4 is used as a precursor [5], but also the thin layer of SiO_2 on the surface of oxidized nanowires can be removed and replaced with hydrogen by etching

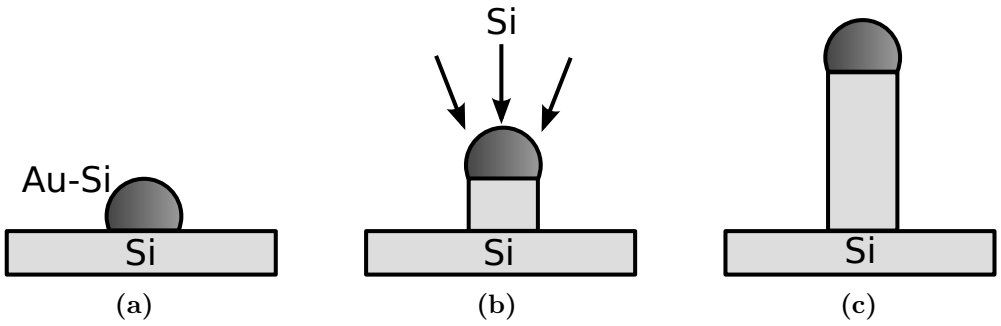

Figure 1.2: Schematic representation of VLS growth. (a) The Au droplet is firstly deposed on a silicon substrate and then (b) the nanowire grows from the nucleation of silicon adsorbed from the supersaturated Au-Si alloy until (c) the completion of the growth process.

with HF [4].

1.2 Quantum mechanics for nanostructure

In semiconductor nanostructure, when the electrons are confined in small regions of space, in the range of few tens of nanometers or below, the electrons are strongly affected by the confinement and quantum effects start to play a major role in the determination of the energy spectrum. The effects of confinement can be outlined using an idealized model for the nanowire, which relies on the semiconductor band structure and on effective mass approximation (EMA).

1.2.1 Quantum confinement

The simplest way to model a quantum wire is to consider a wire with a rectangular cross-section and with infinitely deep barriers in the directions orthogonal to the wire axis. This is schematically illustrated in Figure 1.3. It is known that an electron inside a crystal with an external potential applied can be well described, in first approximation, with the EMA and the envelope function approach. In this way the wavefunction can be written as the product of a Bloch factor at the minimum of the conduction band and an envelope function F:

$$\psi(\mathbf{r}) = u_{\mathbf{k}_0}(\mathbf{r})F(\mathbf{r}). \tag{1.1}$$

The function F satisfies

$$\left(-\frac{\hbar^2}{2m^*}\nabla^2 + V_{\text{ext}}(\mathbf{r})\right) F(\mathbf{r}) = E_F F(\mathbf{r}), \tag{1.2}$$

which is equivalent to a Schrödinger equation for an electron with effective mass m^* and V_{ext} is the applied external potential. (For detailed calculations see, e.g., Yu and Cardona [6])

In the case of the nanowire considered here, V_{ext} is the well known infinite well potential along the x and y directions and the eigenvalues of equation (1.2) are given

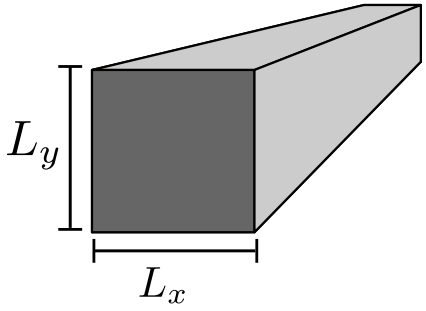

Figure 1.3: Quantum wire defined by an infinitely deep well in x and y directions.

by the sum of three components

$$E_F = \frac{\hbar^2}{2m^*}\left(E_{n_x} + E_{n_y} + k_z^2\right), \quad E_{n_i} = \left(\frac{n_i \pi}{L_i}\right)^2. \tag{1.3}$$

A similar calculation can be done for holes, leading to an increase of the bandgap of the nanowire, with respect to that of the bulk semiconductor, which is proportional to $\sim 1/L^2$, where L indicates the lateral size of the nanowire.

As a side result, one can obtain the density of state ρ for a nanowire of length L_z [7]:

$$\rho_{1\mathrm{D}} = \sum_{n_x,n_y} \frac{L_z}{\pi\hbar}\sqrt{2m^*}(E - E_{n_x} - E_{n_y})^{-1/2}. \tag{1.4}$$

From this expression it is evident that there are no states for energies below $E_{n_x} + E_{n_y}$ and that $\rho_{1\mathrm{D}}$ has divergences every time the energy equals $E_{n_x} + E_{n_y}$.

1.2.2 Band folding

Another important feature arising from the confinement of the nanostructure is the folding of the band structure in the confined directions. The phenomenon of band folding is well studied in the field of semiconductor technology, when the periodicity of the crystal is altered, for example in a superlattice [8]. In the case of nanowires, in the confined directions the periodicity becomes infinite and so, in the first Brillouin zone, the bands are folded back to the direction along the axis of the nanowire.

Let us consider what happens in the case of silicon nanowires. The conduction band of bulk silicon is known to have six equivalent minima near the X-points, located at $\pm(k_c, 0, 0)$, $\pm(0, k_c, 0)$, $\pm(0, 0, k_c)$ with $k_c = 0.852\pi/a_0$ and a_0 the silicon lattice parameter. The six valleys are depicted in Figure 1.4. Supposing that the nanowire is oriented along the direction [001], the other four valleys $\pm(k_c, 0, 0)$ and $\pm(0, k_c, 0)$ are folded to the Γ point.

As can be seen in equation (1.3), the effectiveness of quantum confinement in rising the bottom of the conduction band depends on the inverse of the effective mass. Since in silicon the longitudinal and transverse effective masses are different, the quantum confinement acts differently on the valleys that are folded and on the ones that are not. Given that $m_t = 0.19m_0$ and $m_l = 0.92m_0$, where m_0 is the mass

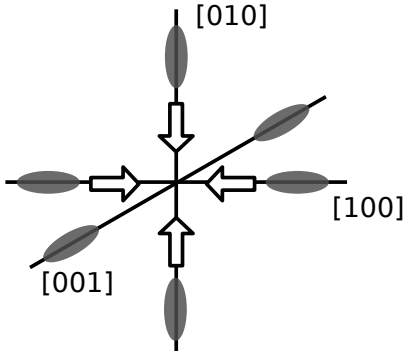

Figure 1.4: Iso-energy surfaces of the six equivalent valleys in bulk silicon conduction band. If the nanowire is oriented along the [001] direction, the valleys along the directions [100] and [010] are folded back to the Γ point, as indicated by the white arrows.

of a free electron, the valleys on the [001] direction have a light effective mass along the confinement directions, while the folded valleys have an heavy effective mass. In this way the quantum confinement upshifts the $\pm(0, 0, k_c)$ valleys more than it does for the other four, causing an indirect to direct transition in the bandgap structure.

The same idea can be applied to silicon nanowires with other orientations. In the case of [011] oriented nanowires, the situation is quite similar and a direct band gap is expected. In contrast, for a nanowire oriented along the [111] direction there is no conduction band minimum that can be folded to the Γ point and thus it is expected to produce an indirect band gap [9].

1.3 Nanowire properties

The results obtained with the aid of EMA can serve as basic tools to simplify our understanding of the system, but, when it comes to the prediction of specific properties of the nanowires, more sophisticated techniques are required. As a consequence, in the last years, a considerable effort has been devoted to the study of many properties of silicon nanowires, using density functional, GW, tight binding, molecular dynamics and Monte Carlo calculations as well as continuum and thermodynamic models. It should be noted, however, that these simulations have often the drawback of having limitations in system sizes, which are often too restrictive to provide a direct comparison with nanowires obtained experimentally.

One of the first problems that have been addressed is the structural character of the nanowires, which refers to the different orientations, cross sections and surface structure that can be considered. Experimental results and theoretical models agrees on a dependence of the most favourable growth orientation on the diameter with a change from [110] to [112] and to [111] as the diameter is gradually increased [5, 10, 11]. Nonetheless, [100] nanowires have also been observed and other parameters, like pressure, can influence the growth direction [12].

Trying to determine the equilibrium cross section, several shapes have been studied, both with *ab-initio* techniques and simpler models. Particular attention has been paid to the role of the edges [13], of the facets [14] and of the perimeter

[15] and the results suggest a preference for pentagonal and hexagonal cross sections. In the search for the equilibrium surface conformation, also passivation and surface reconstruction should be considered. Various surface reconstruction pattern have been analysed [16] and different passivation groups have been tried [17], but actually most of the results have been obtained with hydrogen passivation. Only recently some calculations have been performed with an SiO_2 surface layer[18, 19]. However, a definitive answer to the problem of which are the most stable configurations is still lacking.

Another important line of research is given by the study of transport properties, both for electrons and heat. This is due to the fact that a deeper knowledge of these properties can support the improvement of the performances of nanowire based technology. These properties shows a quite different behaviour from their bulk counterparts, due to small sizes, quantum effects and large surface to volume ratio. Electronic transport suffers of a reduction in the conductance, due to surface roughness, which contributes strongly to backscattering [20, 21], with a dependence on the nanowire orientation [22]. Another source of backscattering is the presence of impurities, whose scattering cross section is comparable to the sizes of the nanowire section. The effect of some substitutional impurities, like P and B atoms, have been studied [23, 24], even in presence of dangling bonds [25].

Also in the case of heat transport the conductivity is strongly influenced by small sizes and surface effect. It has been verified that the thermal conductance is strongly reduced due to the effects of quantum confinement [26, 27] and of surface disorder on phonons [28]. To distinguish between the quantum effects and surface disorder, the dependence of the conductivity on the temperature has been analysed, explaining the liner trend observed at low temperature [29].

The electronic properties, in particular the effects of confinement in the band structure, like those described in Section 1.2 have also been studied for bare and passivated nanowires. These results will be discussed in the following, in comparison with our simulations.

The above is just a short overview of silicon nanowires properties. Recent and more complete reviews based on simulation results can be found in [30] and [31].

1.4 Applications

We have seen that silicon nanowires have various features that would probably be interesting for applications. In practice, with the improvement of the fabrication techniques described in Section 1.1, a lot of ideas have been proposed to exploit these properties.

One of the first field explored for silicon nanowires applications is that of electronic devices. This should not come as a surprise, given the wide use of silicon technology that has been done in this field. Nanowires can be used as field effect transistor (FET) [32], as building blocks for the assembly of electronic devices [33] and to reduce the sizes in CMOS technology [34]. Also, single electron transistors (SET) can be obtained from silicon nanowires, with the observation of the conductance oscillations which are the evidences of the presence of Coulomb blockade phenomena [35, 36]. In this way multiple quantum dots can be lined up and controlled by gate voltages [37].

While electronic applications are focused on the reduction in size, photovoltaic (PV) applications try to exploit the optical properties of the nanowires. In fact, nanowire arrays have proven to suppress light reflection due to wire geometry, thus resulting as useful candidates as antireflection layer for solar cells. Another possible employment of nanowires in PV is given by radial p-n junction nanowire. This combines the presence of a large volume for the absorption of light along the nanowire axis, with short travel distances of photoexcited carriers to the electrodes, i.e. the radial direction. PV devices can be obtained both from single and arrays of p-n junction nanowires. Axial p-n junction and n-doped nanowires on p-Si substrate have also been considered [38, 39].

As already stated in Section 1.3, silicon nanowires have a reduced heat conductance compared with bulk silicon. This property makes them efficient thermoelectric material. Experimentally it has been verified a reduction of two orders of magnitude in thermal conductivity [40, 41].

The small size of silicon nanowires have been used to produce nanosensors with reduced sizes and high sensitivity to detect biological and chemical species, like DNA, viruses and single molecules [42]. But nanowires are small even compared to a single cell, this means that they can be used to interface with living cells [43] for various purposes: delivery of biomolecules [44], bioprobes [45] and stimulation of neuronal signals [46].

It should be noted that here we have limited the analysis to silicon nanowire, but many other constituents have been used to fabricate nanowires. These include Ge, Si-Ge, II-VI and III-V compounds and even organic materials. Everyone has different properties that can be exploited for many applications; some are those described above, but other can considered, like nanowire photonics, using nanowires as lasers, LEDs and waveguides [47].

In conclusion, even if this is not an exhaustive coverage, we have seen that the study of nanowires, their properties and possible applications are active fields of research, with high number of publications and increasing activities focused on their development.

1.5 Nanowire doping

Given the necessity to functionalize the system, a key element to actually make use of semiconductor nanowires in concrete applications is the ability to efficiently perform doping, i.e. incorporate substitutional impurities. The difficulty in achieving incorporation and uniform distribution of dopants is a problem which affects nanocrystals as well as nanowires. This problem has been confronted firstly in nanocrystals, since nanocrystals with a diameter of few nm can be synthesized easily compared to nanowires [48]. In this case two possible models have been proposed to describe the doping mechanism. One is based on what has been called self-purification, that relies on low solubility limit and on the lower formation energy of a defect near the surface, compared to that inside the nanocrystal [49]. The impurities are thus expected to diffuse to the surface after incorporation and being expelled. In the other models the process is governed by kinetic factors. In this case the doping efficiency is limited by impurity adsorption on the nanocrystal surface,

that is different depending on the facet orientation. At the moment, however, the dispute between the two models has not been settled yet [50].

The problem of the distribution of dopants is open also in the case of nanowires. There are many theoretical works that predict surface segregation of P and B dopants, based on the comparison of formation energies like in the case of nanocrsytals, and this behaviour is enhanced in case of nanowires without passivation or in presence of dangling bonds at the surface of the nanowire [25, 51–53]. This suggests that the preference for surface substitutional site can depend on the electronic properties in addition to relaxation of atomic positions. Other dopant atoms have been used in simulations, but the authors have not observed strong tendency to surface segregation.

Differently from nanocrystals, experimental silicon nanowire have not still reached the small dimensions at which *ab-initio* simulations can be performed, nonetheless some measurements of dopant distribution have been done. Björk et al. [54] have revealed a rise of resistivity for P doped nanowires whose diameter is decreased down to 15 nm. They excluded quantum confinement and surface segregation as possible causes and ascribed their results to donor deactivation due to dielectric mismatch between the conducting channel and its surroundings. Dielectric confinement in silicon nanowires has been predicted theoretically [55] and can be understood as follows. In a bulk semiconductor, the charge of a donor is screened by the dielectric constant ϵ_{in}, leaving a total charge of e/ϵ_{in} near the nucleus. In a bulk semiconductor the remaining charge $e(1 - 1/\epsilon_{\text{in}})$ goes to the infinity, while in a confined structure this is distributed over the surface and thus close the defect. In the limit of really small sizes the nucleus is virtually unscreened with a consequent increase of the ionization energy, that has been esteemed to be

$$\frac{2e^2}{\epsilon_{\text{in}}} \frac{\epsilon_{\text{in}} - \epsilon_{\text{out}}}{\epsilon_{\text{in}} + \epsilon_{\text{out}}} F\left(\frac{\epsilon_{\text{in}}}{\epsilon_{\text{out}}}\right) \propto \frac{1}{R}, \tag{1.5}$$

where F is a polynomial function of the dielectric ratio of the wire to the surroundings and R is the radius of the nanowire.

Conversely, in another work [56], the resistance of a nanowire has been measured reducing progressively the diameter with a low-temperature chemical oxidation and etching process. The decrease in conductance is interpreted by the authors as a signal of higher dopant concentration close to the surface.

The nanowires considered in the previous articles have been synthesized with VLS growth, but phosphorus and boron dopant distribution in VLS grown nanowires has been analysed also with other techniques. These include atom probe tomography [57–59], Kelvin probe force microscopy (KPFM) [60] for silicon nanowires with a diameter ranging from about 15-20 nm to 50 nm and scanning spreading resistance microscopy (SSRM) for bigger nanowires ($\sim$ 100 nm) [61]. In all the cases dopant concentration decreases moving from the wire surface to the core. The nanowires analysed with the first two techniques, have been doped during VLS growth with the same adsorption mechanism of silicon atoms, that is through the gold catalyst, but it is possible that an uncatalysed decomposition takes place at the surface (a vapor-solid process), leading to a higher dopant density compared to the core. This hypothesis is supported by the nonuniformity of the longitudinal distribution of dopants, with a concentration that decrease from the base of the nanowires to the

tip, suggesting that the area which is exposed for more time to the dopant precursor can adsorb more dopant atoms.

In the experiment based on SSRM, the doping of P atoms is carried out by ion implantation and the redistribution of phosphorus takes place during the rapid thermal annealing. This excludes the previous explanation for the higher doping level close to the surface.

Rosenwaks group has observed a large diffusion coefficient in silicon nanowires compared to bulk silicon [60] and have proposed two approaches to improve the uniformity of doping along radial and longitudinal directions [62]. Even if an almost uniform radial distribution is achieved, a higher dopant concentration at the surface is still present and this can prove a tendency to surface segregation in silicon nanowires.

The problem can become even more complicated: a ferromagnetism measure of Mn^+ implanted nanowires has determined a segregation of the donor after high-temperature annealing [63], but this is in conflict with simulation results, which predicts the core sites as more stable [64]. A possible explanation is that at high temperature uncontrolled clustering takes places, destroying magnetism. This is however a sign of the difficulties in comparing theoretical and experimental data.

All these results highlight the relevance of having a way to determine the distribution of dopants inside the nanowire. In the following we will show some results about Se donor distribution and propose a method for the measurements of radial distribution based on electron paramagnetic resonance (EPR).

Chapter 2

Methodology

Solving a physical problem often consists in solving differential equations. Unfortunately, only few equations have an analytical solution, so, in most cases, we have to turn to numerical calculations to predict the properties of a physical system. Performing suitable and efficient numerical calculation is not a simple task either and many theories and algorithms have been developed to fulfil it. In this thesis we are dealing with a problem related to a many-body Schrödinger equation and one of the most diffused techniques to deal with this kind of problems is density functional theory (DFT). This chapter is thus devoted to a brief introduction of DFT and to a more detailed explanation of the approximation that has been employed. At the end of the chapter we present our results about the tests on these approximations and the configurations parameters that have been used for the rest of the calculations in this work.

2.1 Density functional theory

Studying a solid state system implies to solve a Schrödinger equation of interacting electrons and nuclei. The system is described by the following Hamiltonian:

$$\begin{aligned}\hat{H} = &-\frac{\hbar^2}{2m_e}\sum_i \nabla_i^2 + \sum_{i,j}\frac{Z_I e^2}{|\mathbf{r}_i - \mathbf{R}_I|} + \frac{1}{2}\sum_{i\neq j}\frac{e^2}{|\mathbf{r}_i - \mathbf{r}_j|} \\ &-\sum_I \frac{\hbar^2}{2M_I}\nabla_I^2 + \frac{1}{2}\sum_{I\neq J}\frac{Z_I Z_J e^2}{|\mathbf{R}_I - \mathbf{R}_J|}\end{aligned} \tag{2.1}$$

where electrons are denoted by lower case subscripts and nuclei by upper case subscripts. The sums run over all the nuclei and the electrons of the system.

In expression (2.1) the nuclear kinetic term is the only one that can be considered small and can thus be neglected. This is equivalent to consider the nuclei as fixed with respect to the dynamics of the electron and this goes under the name of Born-Oppenheimer approximation. The Hamiltonian for electrons can then be divided into a kinetic term, an interaction between the electrons, an interaction between electrons and the external potential of the nuclei and a classical term given by the Coulomb interaction between nuclei:

$$\hat{H} = \hat{T} + \hat{V}_{\text{int}} + \hat{V}_{\text{ext}} + E_{II}. \tag{2.2}$$

The solution of the Schrödinger equation

$$\hat{H}\psi(\mathbf{r}_i) = E\psi(\mathbf{r}_i) \tag{2.3}$$

for this Hamiltonian cannot be found analytically except for some simple systems. Here is where the DFT comes into play.

If the system has nondegenerate ground-state, it is straightforward to show that given an external potential $V_{\text{ext}}(\mathbf{r})$ there is only one ground-state charge density $n(\mathbf{r})$, where charge density is defined as

$$n(\mathbf{r}) = N \int |\psi(\mathbf{r}, \mathbf{r}_2, \ldots, \mathbf{r}_{N-1}, \mathbf{r}_N)|^2 \, d\mathbf{r}_2 \ldots \mathbf{r}_{N-1}\mathbf{r}_N. \tag{2.4}$$

What is less obvious, but quite easy to prove, is that the converse implication is true as well. This is at the heart of DFT and this result has been formulated in two theorems by Hohenberg and Kohn [65–67].

Theorem 1. *For any system of interacting particles in an external potential $V_{\text{ext}}(\mathbf{r})$ the potential $V_{\text{ext}}(\mathbf{r})$ is determined uniquely, except for a constant, by the ground state particle density $n_0(\mathbf{r})$.*

Since $V_{\text{ext}}(\mathbf{r})$ defines the Hamiltonian, which in turn completely determines eigenvalues and eigenfunctions, as a consequence of the previous theorem all the properties of the system are determined by the density $n_0(\mathbf{r})$.

Theorem 2. *A universal functional for the energy $E[n]$ in terms of the density $n(\mathbf{r})$ can be defined, valid for any external potential $V_{\text{ext}}(\mathbf{r})$. For any particular $V_{\text{ext}}(\mathbf{r})$, the exact ground state energy of the system is the global minimum value of this functional, and the density $n(\mathbf{r})$ that minimizes the functional is the exact ground state density $n_0(\mathbf{r})$.*

The energy functional can be expressed in terms of wavefunction ψ with a fixed density $n(\mathbf{r})$

$$E[n] = \left\langle \psi \,\middle|\, \hat{T} + \hat{V}_{\text{int}} \,\middle|\, \psi \right\rangle + \left\langle \psi \,\middle|\, \hat{V}_{\text{ext}} \,\middle|\, \psi \right\rangle = F[n] + \int n(\mathbf{r}) V_{\text{ext}} d\mathbf{r}, \tag{2.5}$$

where $F[n]$ is a universal functional that does not depend on the external potential and the term E_{II} will be neglected, since it consists of a classical constant. This reduces the complex problem of finding the solution of a many-body Schrödinger equation to that of finding a 3-dimensional function $n(\mathbf{r})$ which minimizes the energetic functional $E[n]$, but this remains hard to solve, since the exact expression of $F[n]$ is unknown. Moreover, the relation between the charge density and all the other properties is not straightforward and their derivation is thus not trivial.

In order to make the problem tractable, Kohn and Sham [68] have reformulated it, replacing the many-body system with a non-interacting auxiliary system having the same ground state density $n_0(\mathbf{r})$ of the original one. This method relies on the hypothesis that an external potential V_{KS} can be found, such that the single particle solutions of

$$\left(-\frac{\hbar^2}{2m}\nabla^2 + V_{KS} \right) \psi_i(\mathbf{r}) = E_i \psi_i(\mathbf{r}) \tag{2.6}$$

have a ground-state charge density

$$n(\mathbf{r}) = 2\sum_i |\psi_i(\mathbf{r})|^2 \tag{2.7}$$

equal to that of the original system. In this approach the total energy functional $E[n]$ is rewritten dividing the terms that are known from the others, confining all our ignorance about the many-body system in the exchange-correlation term. The idea is to group the easily computable terms which amounts to a large fraction of the total energy and leave apart the unknown term, which can be approximated. The Kohn-Sham potential is thus given by

$$V_{KS}(\mathbf{r}) = V_{\text{ext}}(\mathbf{r}) + V_{\text{Hartree}}(\mathbf{r}) + V_{\text{xc}}(\mathbf{r}), \tag{2.8}$$

where V_{Hartree} is the Hartree potential and V_{xc} is the exchange-correlation potential.

Until this point, the shifts from the initial many-body problem, to the variational principle and to the Kohn-Sham formulation have never implied any approximation. This means that, knowing explicitly the universal functional or the Kohn-Sham potential would allow to calculate exact solutions of the systems. Unfortunately these are not know and one has to resort to some approximation of the exchange-correlation term in order to obtain numerical results. The approximations used in literature can be split into two broad categories: the local spin density approximation (LSDA) and generalized gradient approximation (GGA). After their introduction the Kohn-Sham system of equation can be solved self-consistently.

2.2 Supercells and plane waves

The system under consideration in our work is one-dimensional periodic, so it seems natural to consider periodically boundary conditions. The standard way to approach this kind of problem is by the aid of supercells. In practice, this means to consider a unit cell containing a part of the physical system, the supercell, and apply periodic boundary conditions in all the spatial directions. This is exemplified in Figure 2.1 for a one-dimensional and a zero-dimensional system.

Having introduced an artificial periodicity, one has to deal with the unwanted fictitious interactions arising between the supercell and its replicas. This is the case for non fully periodic systems, like nanowires, that interact with replicas of the complete structure in the confined directions, but also for defects inside a bulk crystal.

To obtain meaningful results it is important to reduce these interactions as much as possible and this can be done basically in two ways. The first method consists in simply increasing the size of the supercell, in order to move away the elements that should not interact with each other. This means, in our case, to introduce more empty space between the replicas of the nanowire and to use longer supercell in the growth direction of the nanowire in presence of defects. Despite its simplicity, the enlargement of the supercell cannot be pushed too far, since the computational requirements grow quickly with the size of the supercell. Therefore the other approach tries to remove or correct these interactions, while keeping the size of the supercell fixed.

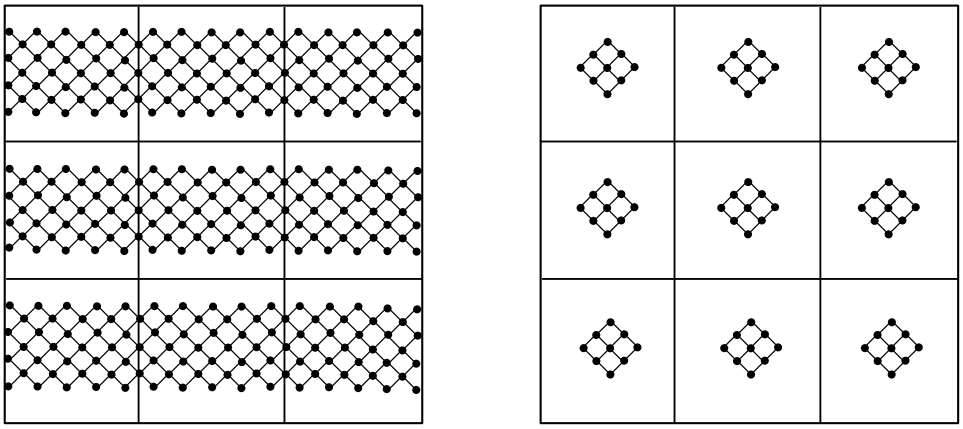

(a) **(b)**

Figure 2.1: Example of supercell for (a) one-dimensional and (b) zero-dimensional systems. The systems are periodically repeated in all the spatial directions. Fictitious interactions arise between the replicas.

Finding suitable schemes that permit to remove the fictitious interactions is still an open problem and many different corrections have been devised [69]. These can be introduced during the calculation, e.g. damping the electrostatic potential beyond a certain interaction range [70], or can be applied to the final results of the total energy. One of the most widely used corrections of this second type is the one by Makov and Payne [71], that calculated a correction to the total energy for systems with charged defects, that depends on the size of the supercell. In our calculation of the formation energies for charged defects we have made use of an adaptation of this method to nanowires by Rurali and Cartoixà [72]. A detailed description of this correction is given in Appendix A.

Working with periodic boundary conditions, any function can be expanded in the complete set of Fourier components. It is known from Bloch theorem that the eigenfunctions can be decomposed in a plane wave times a periodic function, so a wavefunction defined by the band index i and the Bloch index $\mathbf{k}$ can be written as

$$\psi_{i,\mathbf{k}}(\mathbf{r}) = e^{i\mathbf{k}\cdot\mathbf{r}} u_{i,\mathbf{k}}(\mathbf{r}) = \sum_m \frac{1}{\sqrt{\Omega}} c_{i,m} e^{i(\mathbf{k}+\mathbf{G}_m)\cdot\mathbf{r}} \equiv \sum_{\mathbf{q}} c_{i,\mathbf{q}} |\mathbf{q}\rangle \qquad \mathbf{q} = \mathbf{k} + \mathbf{G}_m \quad (2.9)$$

where m is the Fourier index, $\mathbf{G}_m$ are vectors of the reciprocal lattice and $c_{i,\mathbf{q}}$ are the expansion coefficient of the wavefunction in the basis of orthonormal plane waves $|\mathbf{q}\rangle$. Replacing ψ with the previous expression, Kohn-Sham equations in the reciprocal space become

$$\sum_{m'} \left[\frac{1}{2} |\mathbf{k} + \mathbf{G}_m|^2 \delta_{m,m'} + V_{KS}(\mathbf{G}_m + \mathbf{G}_{m'}) \right] c_{i,m'} = E_i c_{i,m}. \quad (2.10)$$

The advantage of this form is that every $\mathbf{k}$ is independent in the first Brillouin zone and can thus be diagonalized separately.

Obviously not all the terms in the Fourier expansion can be considered, but another feature of this method is that one can test the convergence of the results against an energy cutoff E_{cut} on the plane waves

$$\frac{\hbar^2}{2m} |\mathbf{K} + \mathbf{G}_m|^2 \leq E_{\text{cut}}. \tag{2.11}$$

The difficulty of this approach relies in the description of highly localized states, like those in the atom core, due to the delocalized nature of plane waves.

2.3 Pseudopotentials

The presence of core states, being localized close to the nucleus, poses a serious problem to the expansion in plane waves. The solution comes from the observation that the main contribution to chemical bonding and solid state properties comes from valence states, therefore all the relaxation of the core states can be safely ignored (the so called frozen core approximation). The idea is to replace the original atom with a pseudoatom with frozen core states and with smooth wavefunctions inside a cutoff radius for the valence states, in order to remove all the strong oscillations of the real wavefunctions.

Concrete realization of this approximation is done by replacing the original potential with a pseudopotential [73]. A good pseudopotential should have the following properties:

1. Pseudopotentials and pseudowavefunctions should be as soft as possible, i.e. they should be expandable with the least number of plane waves.

2. Pseudopotentials should be transferable, i.e. a pseudopotential generated in a certain electronic configuration should reproduce all the other chemical configurations.

3. Pseudowavefunctions should agree as much as possible with the real wavefunctions beyond a certain cutoff radius r_c

These properties are illustrated schematically in Figure 2.2.

A modern solution that satisfies the requirements is the one proposed by Hamann, Schlüter and Chiang [74]: norm-conserving pseudopotential. In this case the transferability is obtained conserving the scattering properties of the original atom. It can be demonstrated that this condition is satisfied if the integrals from 0 to r of the real and pseudo charge density agree for $r < r_c$ for each valence state (from here the name norm-conserving). Several schemes have been proposed for the generation of pseudopotentials that satisfy this condition [75–77].

In some sense, however, norm-conserving pseudopotentials are still "hard" and may require high cutoffs. Vanderbilt has shown that the norm-conserving condition can be slightly relaxed, in a way that preserves the transferability of the pseudopotential but with a smoother shape near the nucleus [78]. These pseudopotentials are usually referred to as ultrasoft and allow to use lower cutoffs compared to norm-conserving pseudopotentials.

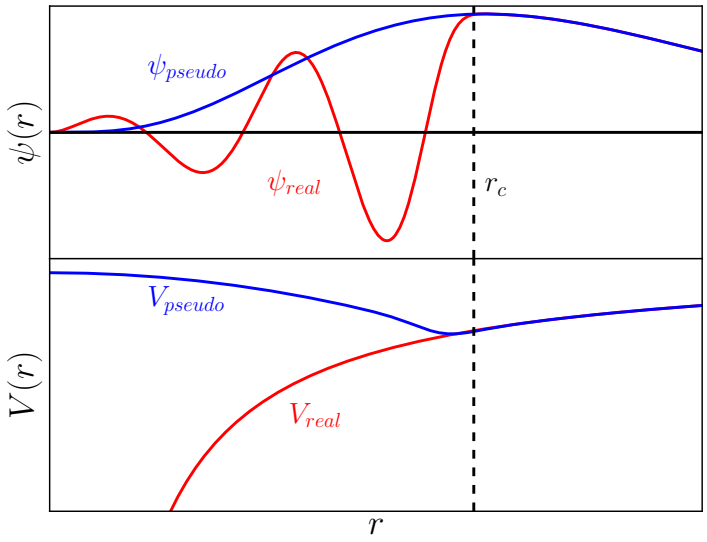

Figure 2.2: Schematic representation of the characteristics of pseudowavefunctions (top) and pseudopotentials (bottom). Red lines represent real values, with oscillations and divergences while blue lines are the pseudo quantities that are smooth and agree with the others for $r < r_c$.

2.4 Projector augmented wave method

Since we are interested in hyperfine structure, the use of pseudopotentials seems to be forbidden. In fact, the calculation of hyperfine parameters requires the knowledge of the real wavefunction close to the nucleus, but this information is not accessible in the pseudopotential formalism. Fortunately Van de Walle and Blöchl have devised a method to reconstruct the all electron wavefunction near the core after the self-consistent pseudopotential calculation and obtain the hyperfine parameters [79]. In addition, it should be noted that this projector augmented wave (PAW) method can also be used as a generalization for the pseudopotential approach [80].

The basic idea behind the PAW method is that the shape of the wavefunction close to the nucleus is essentially atomlike, because of the nuclear strong attractive potential, even when the atom is inside a crystal. It can be then assumed that atomic partial waves are still good solutions in the core region. What changes in the transition from isolated atom to crystals are the boundary conditions. The partial wave inside the core have to match the wavefunction outside and their weights should be changed accordingly.

Based on these observations, the all electron wavefunction can be obtained by the pseudowavefunction, subtracting the contribution from the core pseudo partial waves and replacing it with the core all electron partial waves multiplied by appropriate weights. This is also required to be a linear transformation $\mathcal{T}$:

$$|\psi\rangle = \mathcal{T}\,|\psi\rangle = |\tilde{\psi}\rangle + \sum_i (|\phi_i\rangle - |\tilde{\phi}_i\rangle)\,\langle \tilde{p}_i|\tilde{\psi}\rangle\,. \tag{2.12}$$

Here, ψ and $\tilde{\psi}$ denote the all electron and pseudo wavefunctions, while ϕ_i and $\tilde{\phi}_i$ are the all electron and pseudo partial waves. The index i runs over all the atomic positions and on the angular momentum components. The terms $\langle \tilde{p}_i | \tilde{\psi} \rangle$ are the coefficient c_i in the expansion of the pseudo and all electron wavefunctions on partial waves in the core region Ω_{r_c}

$$\begin{aligned} |\tilde{\psi}\rangle &= \sum_i c_i \, |\tilde{\phi}_i\rangle \\ |\psi\rangle &= \sum_i c_i \, |\phi_i\rangle \end{aligned} \qquad \text{in } \Omega_{r_c} \tag{2.13}$$

The functions $\tilde{p}_i$ act then as projectors for the pseudowavefunction on the pseudo partial waves and should satisfy the condition

$$\langle \tilde{p}_i | \tilde{\phi}_j \rangle = \delta_{ij}. \tag{2.14}$$

In this framework, the all electron matrix elements of an operator A can be derived from the pseudo matrix elements and the projectors, using the following equality

$$\begin{aligned} \langle \psi_n | A | \psi_m \rangle = \langle \tilde{\psi}_n | A | \tilde{\psi}_m \rangle + \sum_{ij} \langle \tilde{\psi}_n | \tilde{p}_i \rangle \, (\langle \phi_i | A | \phi_j \rangle \\ - \langle \tilde{\phi}_i | A | \tilde{\phi}_j \rangle) \, \langle \tilde{p}_j | \tilde{\psi}_m \rangle + \Delta A_{nm}. \end{aligned} \tag{2.15}$$

The hyperfine parameters can be calculated applying this expression to the appropriate operators.

It should be noted that, due to frozen core approximation, core polarization is not included in this model. Methods to introduce this correction exist, but we have not taken them into account, since they are often negligible [79].

2.5 Configuration and convergence tests

Up to now we have described the techniques and approximations that we have made use of. In this section we discuss the configuration parameters employed in our simulations, explaining our choices.

For all the calculations presented in this thesis we have used the open-source suite Quantum ESPRESSO [81] which is an implementation of the DFT based on plane waves and pseudopotentials. The hyperfine parameters have been computed with the aid of GIPAW extension[1].

The exchange-correlation functional has been approximated by GGA as proposed by Perdew, Burke and Ernzerhof [82] both for spin-polarized and spin-unpolarized cases. This scheme has been preferred to the LDA approximation since in our tests the bandgap obtained with GGA was slightly wider, even if still far from the experimental results. This is what one should expect, since it is known that the "deficiency of LDA" is only partially improved in GGA.

[1] Presently the GIPAW extension for Quantum ESPRESSO lives as an external project which includes an experimental implementation of a core relaxation correction. We point out that our calculations has been performed with the previous version included in the package and without core relaxation correction.

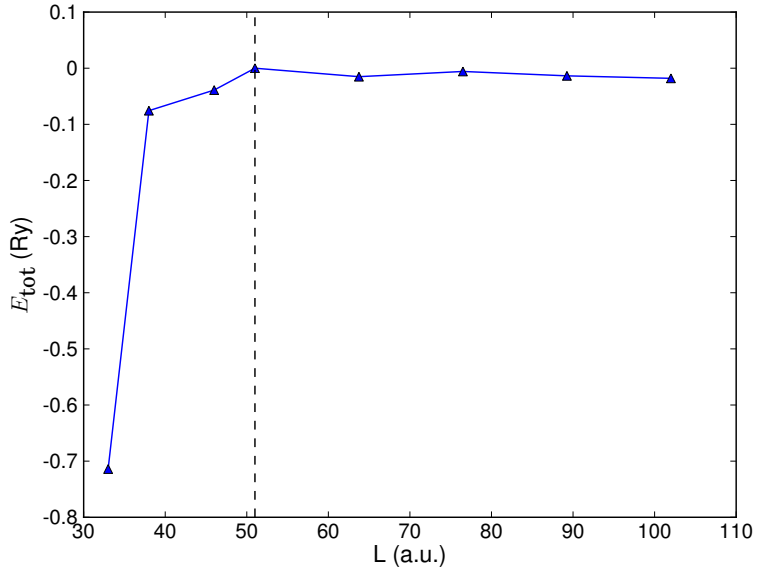

Figure 2.3: Total energy of a pristine nanowire with diameter of 1.5 nm as a function of the width of the supercell.

In order to determine the size of the supercell in the direction orthogonal to the nanowire axis, we have studied the variation of the total energy as a function of the supercell width for a pristine nanowire with a diameter of 1.5 nm. Based on our results (see Figure 2.3), a distance of about 10 Å between the nanowire and its replicas is enough to reduce consistently the fictitious interactions. This result is in agreement with most of the values chosen in literature and we have kept this same distance for all the other nanowires considered. Rurali et al. [83] have, however, claimed that more vacuum should be space should be used to completely suppress unwanted interactions, but that this is not a critical parameter to obtain converged values.

The length of the supercell along the nanowire depends on its orientation. A relaxation of the supercell size along the z axis has been considered in pristine nanowires in order to reduce the stress in the system. For doped nanowires the distance between the donor and its fictitious replicas is at least 1.6 nm.

In our simulations we have used ultrasoft pseudopotentials to study the energies of the system and norm-conserving Troullier-Martins [76] pseudopotentials to calculate the hyperfine parameters. As explained previously the norm-conserving pseudopotentials are "harder" than ultrasoft and this can be seen in our convergence tests in Figure 2.4. These are the total energy values for a nanowire of diameter 1.2 nm containing a Se defect on its axis as a function of the cutoff E_{cut}. Similar results have been obtained for a S doped nanowire. We have thus chosen a cutoff of 25 Ry for ultrasoft and 40 Ry for norm-conserving pseudopotentials.

The surface Brillouin zone integration was performed with a Monkhorst-Pack grid [84] along the nanowire axis, whose size depend on the length of the supercell.

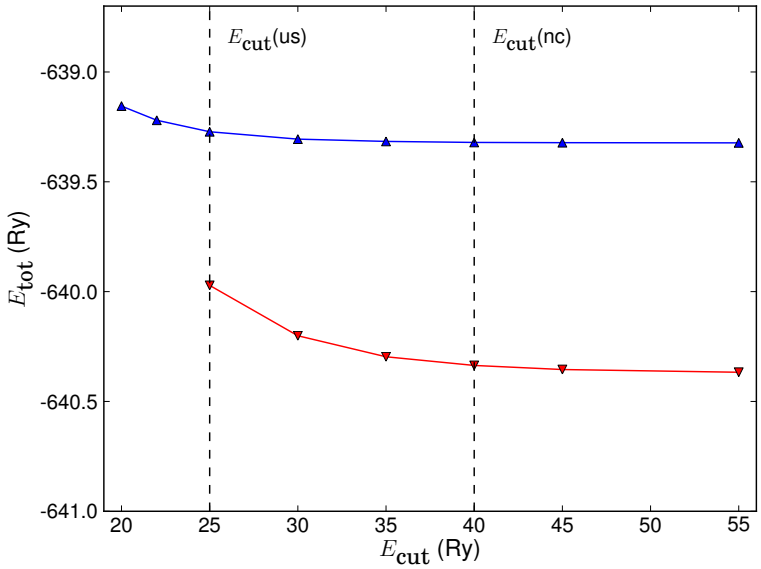

Figure 2.4: Convergence tests for the cutoff E_{cut} in a nanowire with a Se defect on its axis for both norm-conserving (blue) and ultrasoft (red) pseudopotentials. The dashed vertical lines indicate the chosen values.

The atomic positions have been relaxed until the forces on all the atoms are lower than 0.02 eV/Å^{-1}.

Calculations of doped bulk Si have been performed in a cubic supercell of side 1.64 nm with a $3 \times 3 \times 3$ k-point grid.

When needed, namely for singly ionized double donor, spin-polarized calculations have been used. In these cases a total magnetization of +1 has been imposed to the system.

The dielectric tensor $\bar{\varepsilon}$, necessary for the correction to the interaction between charged defect (see Appendix A), has been calculated independently for each nanowire as a linear response to an external electric field [85].

All our main approximations and configuration parameters are collected in tables 2.1 and 2.2 as a reference.

Energy cutoff (`ecutwfc`)	
ultrasoft pseudopotential	25 Ry
norm-conserving pseudopotential	40 Ry
Vacuum space	$\sim$10 Å
Convergence threshold on forces (`forc_conv_thr`)	0.02 eV/Å^{-1}
Convergence threshold for selfconsistency (`conv_thr`)	$1. \times 10^{-8}$
Exchange-correlation functional	GGA-PBE

Table 2.1: Approximations and configuration parameters used in the simulations. In parenthesis, where possible, the name of the corresponding parameter in Quantum ESPRESSO.

System	MP k-point grid
nanowire [001]	
pristine	$1 \times 1 \times 15$
doped	$1 \times 1 \times 11$
nanowire [011]	
pristine	$1 \times 1 \times 15$
doped	$1 \times 1 \times 9$
nanowire [111]	
pristine	$1 \times 1 \times 13$
doped	$1 \times 1 \times 9$
Si bulk	$3 \times 3 \times 3$

Table 2.2: Monkhorst-Pack grid for all the systems considered in the simulations. The third component is along the nanowire axis. These should be set in Quantum ESPRESSO by the `K_POINT` card.

Chapter 3

Pristine nanowires

In this chapter we introduce the detailed structure of the nanowire considered and how they have been constructed, with particular attention to structural properties of the relaxed structure. We then present our results about the electronic properties, limiting to the case of pristine nanowires. The band structure of the system is analysed for different surface reconstruction and for different nanowire orientations. Since this topic has been widely discussed, we also give a comparison of our results with those present in literature. To clear out any possible misunderstanding, we specify that we refer to "pristine nanowire" for undoped H passivated nanowires, as opposed to the term "doped nanowire", used when the chalcogen impurities are present. Instead, we will use the term "bare" for nanowires without passivation, while these are sometimes called "pristine" in literature.

3.1 Nanowire structure

We have already discussed in Section 1.3 the fact that the determination of the most stable cross section for nanowires is an open problem. Here, however, we are interested in determining trends based on the size of the nanowire, so the most natural choice is to consider nanowires with a circular cross section. This seems also reasonable because experimental nanowires often displays hexagonal cross sections, that, at such small sizes, can be well approximated by a circle. The basic silicon structure of our nanowires has thus been obtained cutting a cylindrical section out of a bulk silicon crystal along the desired orientation.

3.1.1 Passivation

Since the wires grown experimentally are always passivated, we had to passivate our structures. Some attempts have been done to determine a simple passivation with oxygen to mimic the SiO_2 external layer, but no satisfactory solution has been devised, while methods like those involving molecular dynamics [19] and Monte Carlo techniques [18] are computationally expensive and require large diameter to have a crystalline core. We have thus chosen single hydrogen atoms to passivate the dangling bonds since, as pointed out in Section 1.1, hydrogen passivated nanowires have been observed experimentally.

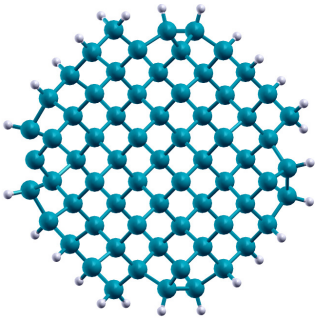

Figure 3.1: Example of a nanowire with unsatisfactory passivation after surface reconstruction. The silicon atom at the left side does not bond easily hydrogen atoms, but in this way a dangling bond state is present in the band-gap

In this work we have focused mainly on an approach to the surface passivation that considers the surface reconstruction of the nanowires. In practice the cylindrical structure cut from the bulk silicon is fully relaxed, leading to the formation of dimers on the surface of the nanowire. At this point the remaining dangling bonds are passivated with hydrogen atoms, trying to preserve the tetrahedral symmetry for each silicon atom at the surface, then the system is relaxed again. This kind of passivation has already been used previously [86, 87] and we believe that it can better reproduce the surface structure of experimental nanowires. Moreover, this approach has the advantage of requiring fewer passivating atoms than the simple passivation of the initial cylindrical structure, reducing the computational effort of the simulation for nanowires of about the same diameter.

On the other hand this approach has two main drawbacks. The first is that not all the diameter of the cylindrical section provide good structures. In fact it is possible that, after the first relaxation, the surface silicon atoms are distributed in a way that makes hard to correctly passivate all the dangling bonds, leaving unwanted states in the gap. A typical case is reported in Figure 3.1, where a satisfactory passivation of the silicon atom in left has not been found. This is usually related to number of silicon atoms on every facets and to the possible surface reconstructions. The second problem is given by the strong deformations the system undergoes when the sizes are reduced too much. For diameters below 1 nm the surface relaxation modifies also the inside of the nanowire, eliminating, de facto, the crystalline core structure.

In light of these problems we have thus considered also another procedure, that consists in simply passivating the surface silicon atoms of the cylindrical structure as it is obtained from the cut in the bulk, preserving the tetrahedral structure of each atom, and relax the system just once. This may be important in combination with the previous method for nanowires with the same number of silicon atoms, since allows to study the effect of surface deformation on the properties of the system. A comparison of unrelaxed and relaxed nanowires prepared with these two different procedures can be seen in Figure 3.2.

A last issue concerns the possibility of having more than one stable configuration after the first relaxation. This situation occurred for one of the nanowire under consideration (NW1 following the definition given below) and the two possible surface

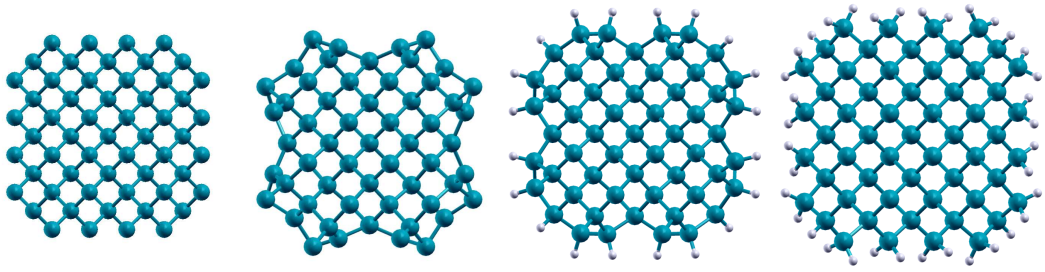

(a) (b) (c) (d)

Figure 3.2: Comparison between unrelaxed and relaxed nanowires with different passivation approaches. (a) Nanowire cut from bulk silicon with circular section. (b) Relaxed nanowire without passivation. (c) Relaxed nanowire after passivation of the previous structure. (d) Nanowire passivated from the cylindrical cut in the bulk. Si and H atoms are represented in cyan and white, respectively.

(a) (b)

Figure 3.3: Two alternative surface reconstruction for a [001] with a diameter of about 1.2 nm. The structure in (a) has a slightly lower total energy, but, since the difference after hydrogen passivation is small we have considered the more symmetric structure in (b).

reconstructions are displayed in Figure 3.3. Based on the value of the total energy one can conclude that the structure in Figure 3.3a is slightly more favourable. However, after hydrogen passivation the difference in the total energy is reduced and, since the structure of Figure 3.3b has a more symmetric structure, we have decided to study only this last configuration. Note that the two passivations need a different number of hydrogen atoms, so the comparison has been done adding N/2 times the total energy of a H_2 molecule to the system with less hydrogen atoms.

Our non passivated final structure are in agreement with those calculated for similar nanowires by Rurali et al. [14],

3.1.2 Orientation and dimensions

Most of our simulations are based on nanowires oriented along the [001] direction passivated after surface relaxation. Nanowires with the same number of silicon atoms but passivated from the beginning have been considered for comparison, with the addition of a smaller nanowire that couldn't have been studied using the other passivation process. The diameter of the nanowires is in a range that goes from about 0.8 nm to 2.0 nm. Pristine nanowires with a larger diameter could

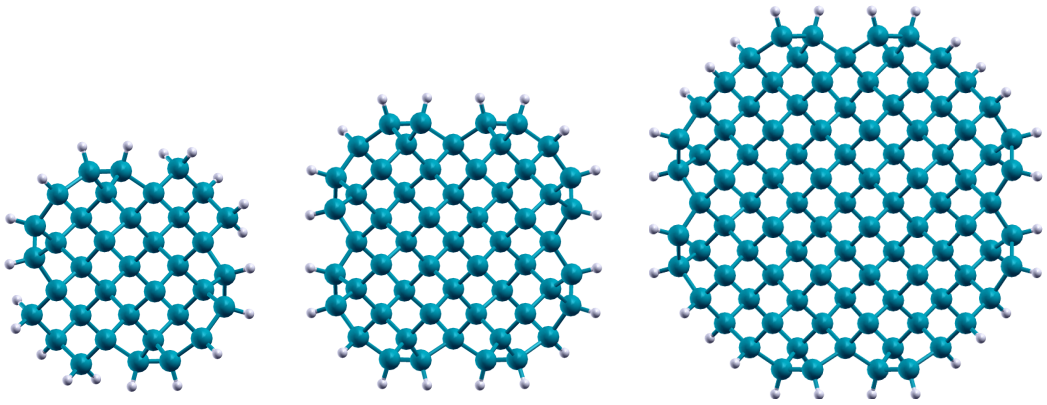

(a) NW1 **(b)** NW2 **(c)** NW3

Figure 3.4: Section view of the [001] oriented silicon nanowires obtained after surface reconstruction and H passivation. These are the nanowires that will be used for most of the simulations. NW1 has a diameter of about 1.2 nm, NW2 of about 1.5 nm and NW3 of about 2 nm.

have been studied, but our interest is for defective nanowires, which require longer supercell. In presence of the defect the larger nanowire is close to our computational limit. The [001] oriented nanowires that have been studied in this work are shown in Figure 3.4 in the case of surface reconstruction and in Figure 3.5 without surface reconstruction, along with a short name we will use from now on to refer to these nanowires. Note that the couples of nanowires NW1-NW5, NW2-NW6 and NW3-NW7 have approximately the same diameter. As can be seen from Figure 3.5, nanowires without initial relaxation have sharp {100} and {110} facets, while surface reconstruction makes the surface smoother, giving a circular shape to the nanowire. Another structural difference between the two groups of nanowires is that for those in Figure 3.4 almost all the surface silicon atoms need just one hydrogen to passivate the dangling bonds.

Looking at Figure 3.4 it is also evident that NW1 has a less symmetrical structure compared to NW2 and NW3. The reason is that every facet of the nanowire before the surface reconstruction has only three atoms. This prevents the formation of a completely symmetric dimerization of the surface atoms and the asymmetry is maintained after the passivation.

It should be noted that the definition of nanowire diameter is somewhat ambiguous, in particular for the nanowires that don't have a circular cross section. We have defined the value of the nanowire radius by the average of the radial distance of the surface silicon atoms from the axis of the nanowire but other definitions can be found in literature. Some examples are those based on the volume of the nanowire in the supercell [88], on the electron cloud [89] and on the largest cylinder inscribed in the nanowire [90]. As a consequence different radii can be attributed to nanowires with the same number of silicon atoms and a direct comparison between result is not always straightforward.

In addition to [001] oriented nanowires we have also considered [011] and [111] orientations. These nanowires have been studied as a comparison with the previous

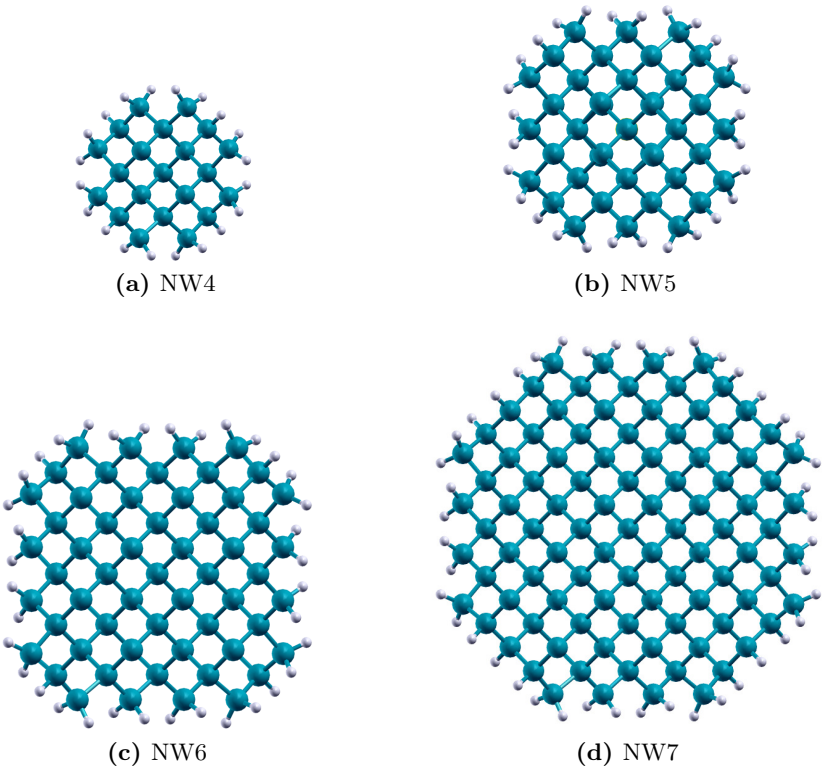

(a) NW4 **(b)** NW5

(c) NW6 **(d)** NW7

Figure 3.5: Section view of the [001] oriented silicon nanowires without surface reconstruction. The nanowires NW4-7 have a diameter of about 0.8 nm, 1.2 nm, 1.6 nm and 2.0 nm, respectively. Note that NW5-7 have approximately the same diameter as NW1-3, respectively.

set, in particular for the nanowire NW2, which is the most interesting in presence of a donor as will be shown in the following chapters. In these cases a satisfactory passivation after surface reconstruction has not been found in the range of interest of the diameter, so we have used only nanowires passivated from the beginning. Only two different diameters have been selected for each orientation (see Figure 3.6): one is a small nanowire used mainly as a test with size similar to NW4 and the other has a circular section and a diameter as close as possible to that of NW2. Like nanowires NW4-7, these have shaper corners compared to NW1-3, but we can observe from Figure 3.6 that [011] oriented nanowires have nonetheless a quite smooth surface, due to the disposition of the atoms. Here the facets are in the directions {100} and {111} for [011] nanowires and {111} for [111] nanowires.

The nanowires oriented in the various directions differ also in the periodicity of the lattice along the growth direction. For a face-centered cubic lattice like silicon, in the case of [001] oriented nanowires the periodicity is the same as the lattice parameter in the bulk crystal a_0 (=0.5431 nm for silicon). For [011] oriented nanowire the unit cell has a smaller length, that is $a_0/\sqrt{2}$. This is an advantage for the simulation of pristine nanowires, since it allows to reach bigger diameter with lower computational effort. Conversely, [111] oriented nanowires have a longer unit cell, since the first repetition occurs after traversing all the diagonal of the cubic

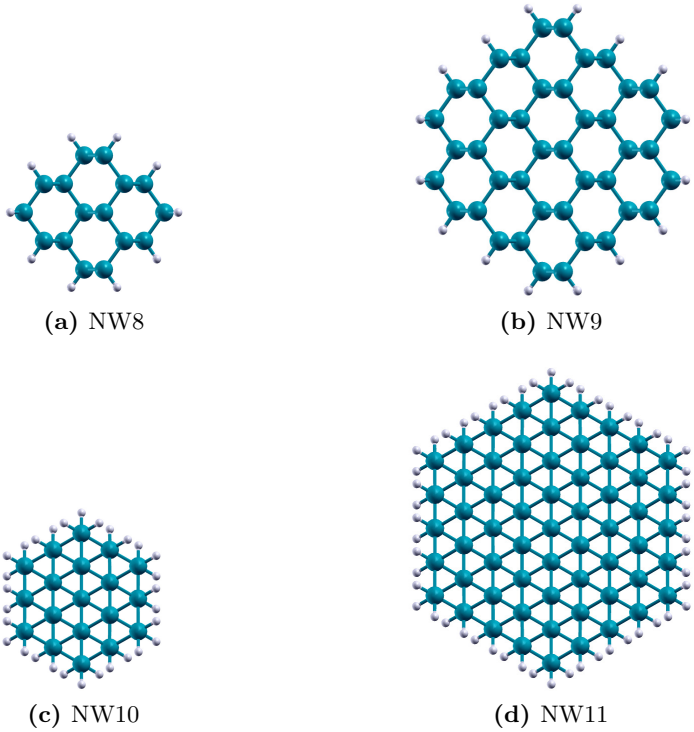

(a) NW8 **(b)** NW9

(c) NW10 **(d)** NW11

Figure 3.6: Section view of [011] (panels (a) and (b)) and [111] (panels (c) and (d)) oriented silicon nanowires without surface reconstruction. NW8 and NW10 have a diameter close to that of NW4, while NW9 and NW11 close to that of NW2.

unit cell of the bulk crystal. The lattice parameter in this case is thus $\sqrt{3}a_0$.

The detailed structural properties, which include stoichiometry, diameter and the relaxed size of the length of the supercell L_z for the pristine nanowires are collected in Table 3.1.

3.1.3 Atomic and axial relaxations

A first effect of the surface reconstruction can be seen directly on the structural properties of the nanowires after the relaxation of the atomic positions and of the length of the supercell.

From Table 3.1 it is immediate to verify that, although the couples of nanowires NW1-NW5, NW2-NW6 and NW3-NW7 have the same number of silicon atoms, they have different diameters. In particular, the nanowires without surface reconstruction are always bigger than their equivalent. This is quite obvious, since the formation of dimers on the surface reduces the distance of these atoms from the axis of the nanowire, which is the base of the definition of the diameter. Nevertheless, it is interesting to inspect the change in the radial disposition of all the atoms inside the nanowire.

We define a *shell* in the nanowire as the set of those silicon atoms who have approximately the same distance from the axis (i.e. the same cylindrical radius). More precisely, we have split up the atoms in the various shells based on their

nanowire	stoichiometry	diameter (nm)	L_z (nm)
[001]			
NW1	$Si_{37}H_{20}$	1.18	5.388
NW2	$Si_{57}H_{20}$	1.52	5.398
NW3	$Si_{97}H_{28}$	1.99	5.418
NW4	$Si_{21}H_{20}$	0.84	5.493
NW5	$Si_{37}H_{28}$	1.21	5.502
NW6	$Si_{57}H_{36}$	1.59	5.512
NW7	$Si_{97}H_{44}$	2.03	5.499
[011]			
NW8	$Si_{16}H_{12}$	0.84	3.946
NW9	$Si_{42}H_{20}$	1.51	3.939
[111]			
NW10	$Si_{38}H_{30}$	0.83	9.444
NW11	$Si_{122}H_{54}$	1.67	9.482

Table 3.1: Structural details of the nanowires used in the simulations. Nanowire names refer to Figures 3.4, 3.5 and 3.6. The stoichiometry refers to the number of atoms contained in the supercell and L_z is the length of the supercell along the growth direction of the nanowire (always chosen as z in our simulations).

position in the crystalline structure as it is obtained after the cut from the bulk, defining the radius of a shell as the average radius of the atoms belonging to a shell (we call r_{init} the starting value). Each shell usually contains 4 or 8 atoms. In this framework, the quantity

$$\Delta r_{\text{shell}} = r_{\text{shell}} - r_{\text{init}}. \tag{3.1}$$

allows to compare the variation of the average radius of the shells for different nanowire structures. In Figure 3.7 Δr_{shell} is plotted as a function of the shell radius for the [001] oriented nanowires. The most evident feature of these results is a strong reduction of the radius of the (sub)surface shells for bare nanowire (blue lines) at all the diameters as a consequence of the dimerization and surface reconstruction. This is only partially healed by the passivation in NW1 and NW2 while in NW3 the initial radius of the surface shell is restored. Conversely, we observe that, consistently with the values of the diameter, in all the nanowires the absence of surface reconstruction leads to an increase of the radius of the external shells compared to the bulk values.

Concerning the core, there is a quite different behaviour between the nanowires obtained with different passivation processes: during the first relaxation, core shells are displaced from their initial positions with an oscillating pattern. This distribution is preserved after the passivation, as it is evident from the high overlap between blue and red lines in Figure 3.7. In the other case the variation is much more smooth, even almost linear for NW7, with every shell having a larger radius than the corresponding one in the bulk. Aside from these differences, the change in the radius of the first shell is almost the same for every nanowire. This can be of some interest in relation to the study of hyperfine parameters of doped nanowires,

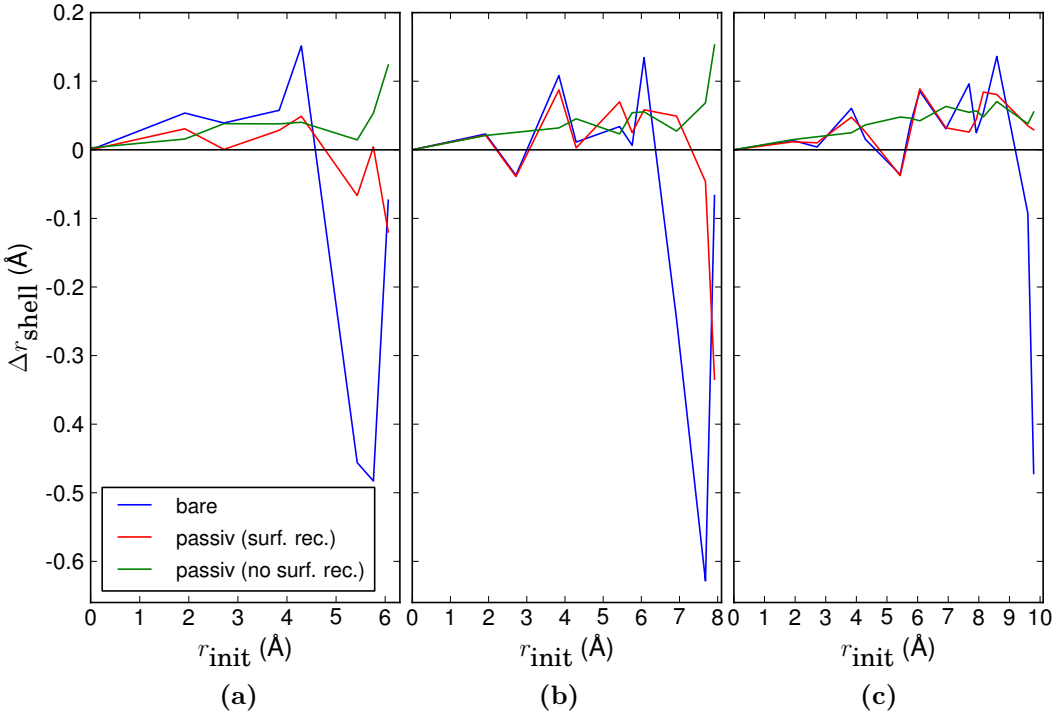

Figure 3.7: Change of the radius of each shell Δr_{shell} (equation (3.1)) as a function of the initial radius of the shell for (a) NW1-NW5, (b) NW2-NW6 and (c) NW3-NW7. Blue lines refer to the displacements of the relaxed bare nanowires, red lines to nanowires passivated after surface reconstruction and green lines to those without surface reconstruction.

that we have studied. However, it is important to note that all the variations in the core are about an order of magnitude smaller than those at the surface and their influence on the electronic properties of the nanowire can be limited.

Another systematic difference between the two groups of nanowires NW1-3 and NW5-7, that can also be recognized from Table 3.1, is that nanowires with surface reconstruction have always a supercell shorter than that of the corresponding nanowire without surface reconstruction. This result seems to be in contrast with the variation of the shell radius, because one expects that reducing the supercell length leads to an increase of the radius and vice versa, being this the exact behaviour that we have obtained changing the size of a single nanowire, by imposing a different supercell length. This fact can be explained with the presence of the dimers on the surface, oriented partially along the growth direction of the surface reconstructed nanowires, that contribute to compress the system also in its length.

The length of the supercell reveals also a trend depending on the diameter of the nanowires: irrespective of the passivation process and with the exception of NW7, L_z grows with the increase of the diameter. The lattice parameter of a bulk Si crystal calculated with our pseudopotential at a cutoff of 25 Ry is 5.475, that should be used as a term of comparison to the values in Table 3.1, instead of the experimental value. Since a nanowire with a large diameter should be more similar to a bulk crystal, our value of a_0 can explain the increase in L_z for nanowires from

NW1 to NW3 and the reversal at NW7. With the appropriate corrections to the values of the lattice constants, this explanation can be applied also to the nanowires oriented along the [011] and [111] directions.

3.2 Electronic properties

Here we present our results about the band structure and band gap of the nanowires we have considered, with the focus on those oriented in the [001] direction. We also compare the results with those present in literature, completing the brief overview started in Chapter 1.

3.2.1 Bare nanowires

The band structure of bare nanowires (see Figure 3.8) shows a metallic behaviour irrespectively of the diameter, but in Figure 3.8c it can be seen the formation of a gap below the Fermi energy. This small opening in the band structure of the nanowires can be seen also in the smaller nanowires (Figures 3.8a 3.8b), suggesting that this is related to the size of the system. The metallization of the system can be attributed to the high surface-volume ratio of the nanowires and to the presence of dangling bonds at the surface, but the number of these dangling bonds should be reduced by the formation of dimers on the surface. A detailed explanation for the results of these kind of nanowires has been given by Rurali et al. [16]: the metallization is due to the partial distortion of the dimers on the {100} facets that allows the formation of delocalized surface states. With the increase of the diameter the coordination of Si(100) surface is recovered, inducing the transition to a semimetallic or semiconductor structure.

The problem of the metallization of bare nanowires has been confronted also for other cross sections and orientations in literature [53, 91, 92]. What emerges from these studies is that the presence of metallic states is strictly related to the facets, the reconstructions that take place at the surface and the sharpness of the edges. Metallic and semiconducting silicon nanowires can be found over a wide range of diameters and small changes to the arrangement of the atoms can result in big differences in the electronic structure. Moreover, since the presence of the band gap is related to the surface-volume ratio, its width is reduced for smaller nanowires, in contrast with what expected from quantum confinement.

3.2.2 Passivated nanowires

We have seen in Section 1.2 that silicon nanowires are expected to display a wider band gap than the bulk crystal and that for some orientations, namely [001] and [011], this band gap should be direct.

As can be seen from the band structure obtained from our simulations for [001] oriented silicon nanowires (see Figure 3.9) we have verified that the bandgap increases as the diameter of the nanowire is reduced, irrespectively of presence or absence of surface reconstruction. Also, it can be easily observed that in all the cases the conduction band minimum (CBM) has moved to the Γ point, at variance

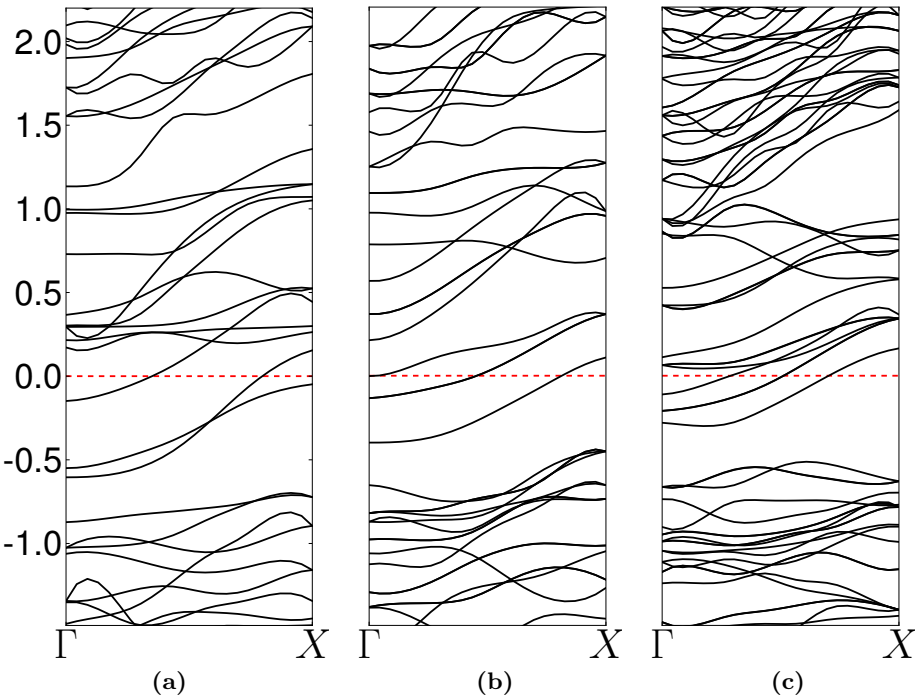

Figure 3.8: Band structure for the bare nanowires (a) NW1, (b) NW2 and (c) NW3 along the axis of the nanowire. The horizontal dashed lines represent the Fermi level of the system.

with bulk silicon. In contrast, an interesting feature arises, leading again to an indirect bandgap: for nanowires with surface reconstruction there is a band crossing that brings the valence band maximum (VBM) away from the Γ point for nanowires with diameter of 1.6 nm (Figure 3.9b) and 2.0 nm (Figure 3.9c). Even if the difference between the top of the valence band and the top at the Γ point is quite small, this effect is not present in the nanowires without surface reconstruction and so it should be ascribed to the reduction of symmetry and to the strain near the surface of the nanowire.

The influences of the surface reconstruction can be seen also on values of the bandgap for nanowires with similar diameter. For the two smaller nanowires, the bandgap of the one which has undergone to surface reconstruction before passivation is smaller than the corresponding one that has been passivated from the beginning. As the diameter increases this difference decrease and vanishes at a diameter of 2 nm (Figures 3.9c and 3.9f). This is in contrast with what one could have expected from quantum confinement and the fact that, as already discussed previously, nanowires NW1, NW2 and NW3 have always a smaller diameter than NW5, NW6 and NW7. Based on these data, we conclude that one of the consequences of surface reconstruction is to counteract the effect of quantum confinement. This is in agreement with what we have found for the hyperfine parameters and that will be shown in the following. However, as far as the band gap is concerned, this effect is quite small and can often be neglected.

In the simplified description of nanowires given in Section 1.2, we have seen that

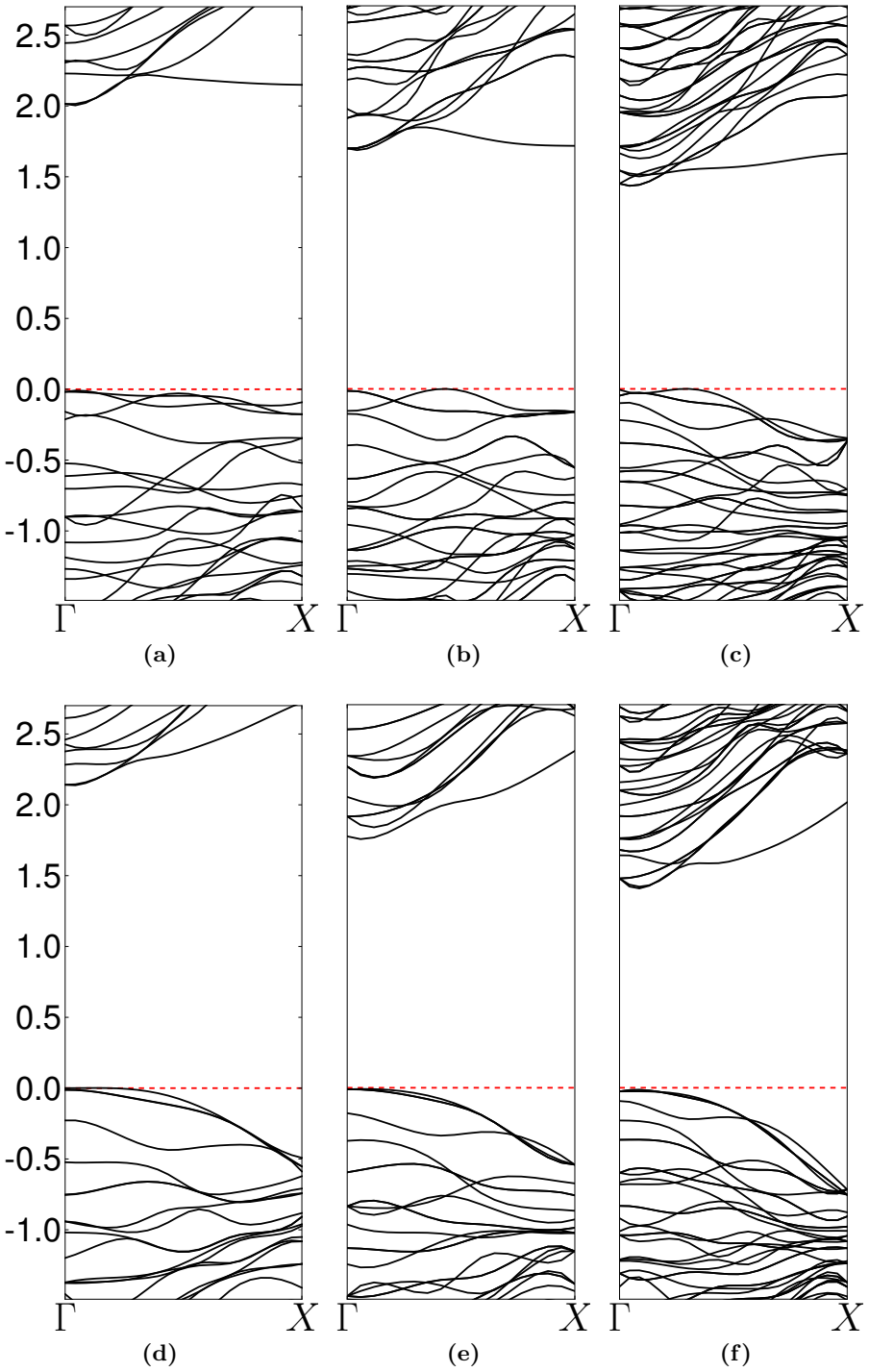

Figure 3.9: Band structure along the axis nanowire of the pristine nanowires (a) NW1, (b) NW2, (c) NW3, (d) NW5, (e) NW6 and (f) NW7, comparing corresponding nanowires with (top) and without (bottom) surface reconstruction. The horizontal dashed lines indicate the top of the valence band. For nanowires with surface reconstruction VBM can be away from the Γ point. The band structure of the small nanowire NW4 have been omitted since it does not have a direct comparison.

in the EMA the band gap of the nanowire is expected to depend on the inverse of the square of the side (equation (1.3)). This suggests that, as proposed by Delerue et al. [93], in order to estimate the dependence of the bandgap E_g on the nanowire diameter d, we should fit the results with the following expression

$$E_g(d) = E_{g,bulk} + C\frac{1}{d^\alpha}, \tag{3.2}$$

where C and α are fitting parameters. Here, instead of the experimental value, for the band gap of bulk silicon $E_{g,bulk}$ we have used the value obtained from simulations performed with the same approximations of the nanowires. This is obvious since the values of the bandgap calculated in our simulations for the diameter tending to infinity should converge to the calculated bulk value and not to the experimental one.

The bandgaps (direct or indirect) calculated within our simulations are shown in Fig. 3.10 along with fits based on equation (3.2), where the values of the diameters are those reported in Table 3.1. The resulting parameters of the fit are $C = 1.62$ and $\alpha = 1.137$ for nanowires with surface reconstruction and $C = 1.76$, $\alpha = 1.113$ without it. The value of the exponent α is thus much smaller than 2, the value that was predicted by EMA. This difference can be explained by the fact that EMA is quite a rough approximation to describe such a complex system and by the wrong assumption underlying EMA that the dielectric constant in a nanowires remains the same as in the bulk crystal. As discussed in Section 1.5 this approximation does not hold due to dielectric confinement.

Finding values of α smaller than 2 is a common feature of the simulation on small nanowires, but there is no strong agreement between the results reported by different groups. For [001] oriented nanowires, different values of α has been obtained in the range 0.9-1.7 (see table 3.2 for a list of values and references). These discrepancies can be ascribed to the differences in the definitions of nanowire diameter and to the small sizes of the nanowires considered, which do not offer enough points to perform the fit of equation (3.2), while the shape of the cross section at fixed diameter seems to have a limited effect on the bandgap [17]. If this is the case, then the most reliable result should be that obtained recently by Ng et al. [94], who have calculated a value of 1.34 for α, considering nanowires with diameter up to 7.3 nm.

Concerning the differences between nanowires obtained with and without surface reconstruction, we can see that, although the width of the band gap present some differences, the trend is almost the same in both cases, as can be seen by the fitting parameters C and α, that have approximately the same value.

We have considered the band gap also for the nanowires oriented along [011] and [111] directions depicted in Figure 3.6. The values are reported in Figure 3.10 but no fit based on equation (3.2) has been considered, since two points would have not provided a reliable sample. From our results we can see that the trend is similar to that of the [001] oriented nanowires, but the width of the band gap depends strongly on the orientation of the nanowire. In particular, the band gaps E_g follow the relation

$$E_g^{[001]} > E_g^{[111]} > E_g^{[011]} \tag{3.3}$$

which can be verified by a comparison of the large number of calculations performed in the past (we did not consider [112] oriented nanowires. Their band gap is ap-

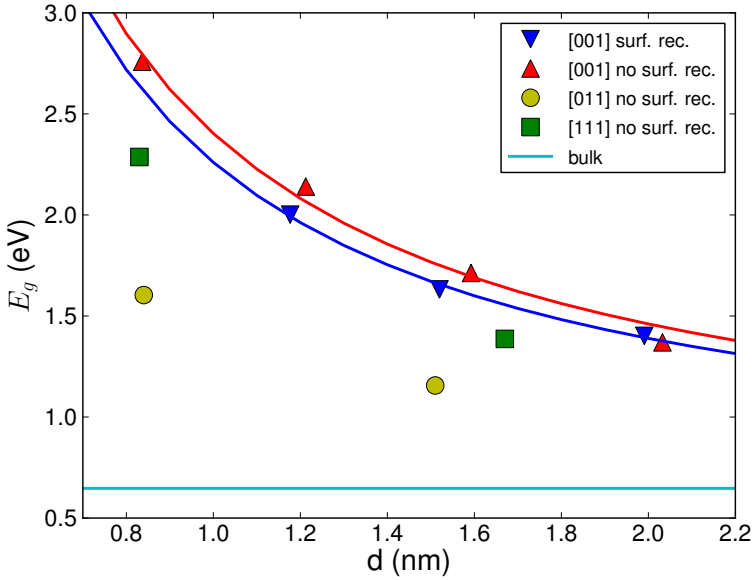

Figure 3.10: Nanowire band gap as a function of the diameter. Triangles indicate the calculated values of the bandgap for [001] oriented nanowires with (blue) and without (red) surface reconstruction, respectively, and the solid lines represent the corresponding fit with the expression defined in equation (3.2). Green squares and yellow circles represent the band gap of [111] and [011] oriented nanowires, respectively. No fit is provided for these cases. The horizontal cyan line indicates the calculated bandgap in bulk Si (0.647 eV).

	This work	Ref. [89]	Ref. [90]	Ref. [94]	Ref [95]	Ref. [96]
α	1.1	1.4	1.3	1.34	1.4 (1.7)	0.9

Table 3.2: Comparison between α in equation (3.2) for [001] silicon nanowires based on theoretical calculations available in literature. Note that the α values are much smaller than 2, which is the value predicted by effective mass approximation. These results have been obtained with different techniques, including hybrid functional Hamiltonian and GW approximation. The results from reference [95] are with and without GW corrections, respectively.

proximately the same as that of [111] nanowires) [30]. Also in these cases, different simulations provide different values of the parameter α. Its value ranges from 1.0 to 1.7 and from 1.0 to 1.8 for [111] and [011] oriented nanowires, respectively [89, 90, 94–96]. Again, for [011] the most recent result for big [011] nanowires indicates a value of 1.01.

As for [001] nanowires, these other orientations show a direct bandgap with the minimum at the Γ point. Although this is expected for [011] nanowires, for the orientation [111] this is in contrast with the EMA result. From the band structure of nanowire NW11, that we don't report here, we can observe that the initial part of the conduction band is almost flat from Γ point. This signals the transition from a direct to indirect band gap that has been observed for [111] oriented nanowires with a diameter above 1.5, depending on the configurations [90, 95, 97]. This is a further confirmation of the inaccuracy of the EMA for nanowires with very small diameter.

It should be pointed out that DFT is known to underestimate the bandgap of materials, and in fact we have obtained a value of the bandgap of the bulk Si which is about 40% smaller than the experimental value (namely 0.647 eV against the experimental 1.14 eV). Nonetheless it has been proven useful at least for obtaining trends of the bandgap [98] and so we can rely on it for the calculation of trends and for the qualitative considerations we have put forward so far.

Chapter 4

Chalcogen doped nanowires

This chapter is devoted to the analysis of the doping of the silicon nanowires described in the previous chapter. Both selenium and sulphur substitutional defect have been considered, but most of the work is focused on the properties of selenium doped nanowires while sulphur has been considered mainly as a comparison for the hyperfine parameters that will be shown in the following. Here we report about our results of the electronic properties and the formation energy of the defects as a function of the nanowire diameter, of the donor donor position and charge state. We also describe the possible formation of hydrogen-chalcogen complexes at the surface of the nanowire.

4.1 Supercell size

In Chapter 2 we discussed the need for using a long supercell in the nanowire growth direction, in order to reduce the spurious interactions between the defect and its replicas. In all the cases under consideration, we have used a supercell length above 1.6 nm, but the exact values obviously depend on the orientation of the nanowire, since it should be an integer multiple of the unit cell. As a final result we have chosen a supercell which is long three times the pristine unit cell for [001] oriented nanowires, two times the pristine unit cell for [111] oriented nanowires and five times the pristine unit cell for [011] oriented nanowires. The exact values has been calculated simply multiplying the relaxed length in Table 3.1.

These sizes have been chosen balancing between the reduction of the interaction and the computational resources required for the simulations. Based on their calculations, Rurali et al. [83] have concluded that the replicas of the defect should be separated by at least 2.4 nm, which is much greater than the sizes usually employed in literature. There are however two reasons to presume that the length of our supercells can be enough in our case. The first is that in their calculations they have considered an aluminium defect, which is a shallow acceptor, while we are working with chalcogens, that are deep donors even for bulk silicon. Being a deep donor should lead to a more localized defect wavefunction and thus requires a smaller distance between the replicas. This difference between shallow and deep dopant has been verified in our calculations of defects in bulk silicon. Considering a cubic supercell with a side of about 1.6 nm, we have observed a strong overlap of

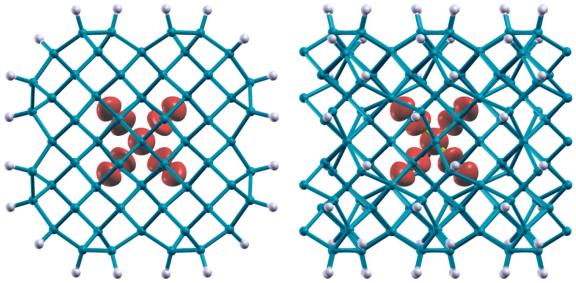

Figure 4.1: (a) Section and (b) side view of the Se defect wavefunction square modulus in nanowire NW2. The Se atom is on the axis of the nanowire and the isosurface of the wavefunction point towards the four tetrahedral directions.

the defect band with the conduction band both for phosphorus and bismuth donors, while, although with a high dispersion, the defect band of chalcogen donor stays always below the conduction band.

The second reason is related to the orientation of the nanowires. Rurali et al. have worked only with [011] oriented nanowires, but we have observed a different behaviour for nanowires with this orientation compared to the others. The first striking difference can be noticed in the shape of the wavefunction associated with the defect. In Figure 4.1 it can be seen the isosurface of the charge density of the Se defect level for a [001] oriented nanowire, with the lobes pointing towards the four tetrahedral directions, which is roughly the same shape for the defect in bulk silicon. This has been calculated for the final supercell with a length of about 1.6 nm, but its appearance does not change significantly even with a distance between the defect and its replicas of 1.1 nm, i.e. two times the pristine unit cell. Similar charge density, adequately rotated, can be observed in [111] oriented nanowires, even in a single unit cell, which means a distance of less than one nanometer. Conversely, the shape of the wavefunction in [011] oriented nanowires is strongly dependent on the length of the supercell. To underline this difference, in Figure 4.2 we have reported the changes of the charge density isosurface as a function of the size of the supercell, along with the corresponding band structure. We have started from a length of 0.8 nm, for which, being the smallest considered, the wavefunction is strongly delocalized along the axis of the nanowire. However, this situation is only partially healed considering supercells of the size comparable to that of [001] and [111] oriented nanowires. For supercells given by the repetition of three or four times the unit cell the wavefunction displays a tendency to stretch in the growth direction and we needed to increase the length of the supercell at nearly 2 nm to suppress, at least partially, this behaviour. Moreover, this size is not sufficient to restore completely the tetrahedral symmetry of the defect wavefunction and we should have increased the supercell length above 2.4 nm, as suggested in [83], but this would have pushed us beyond our computational limit.

The same differences in the behaviour can be seen in the formation energy of the defect. For [001] oriented nanowires, moving from a supercell of 1.1 nm to that of 1.6 nm, the change in the formation energy is of the order of 0.001 eV, while, in the case of [011] nanowires, this change is more then 0.05 eV increasing the distance

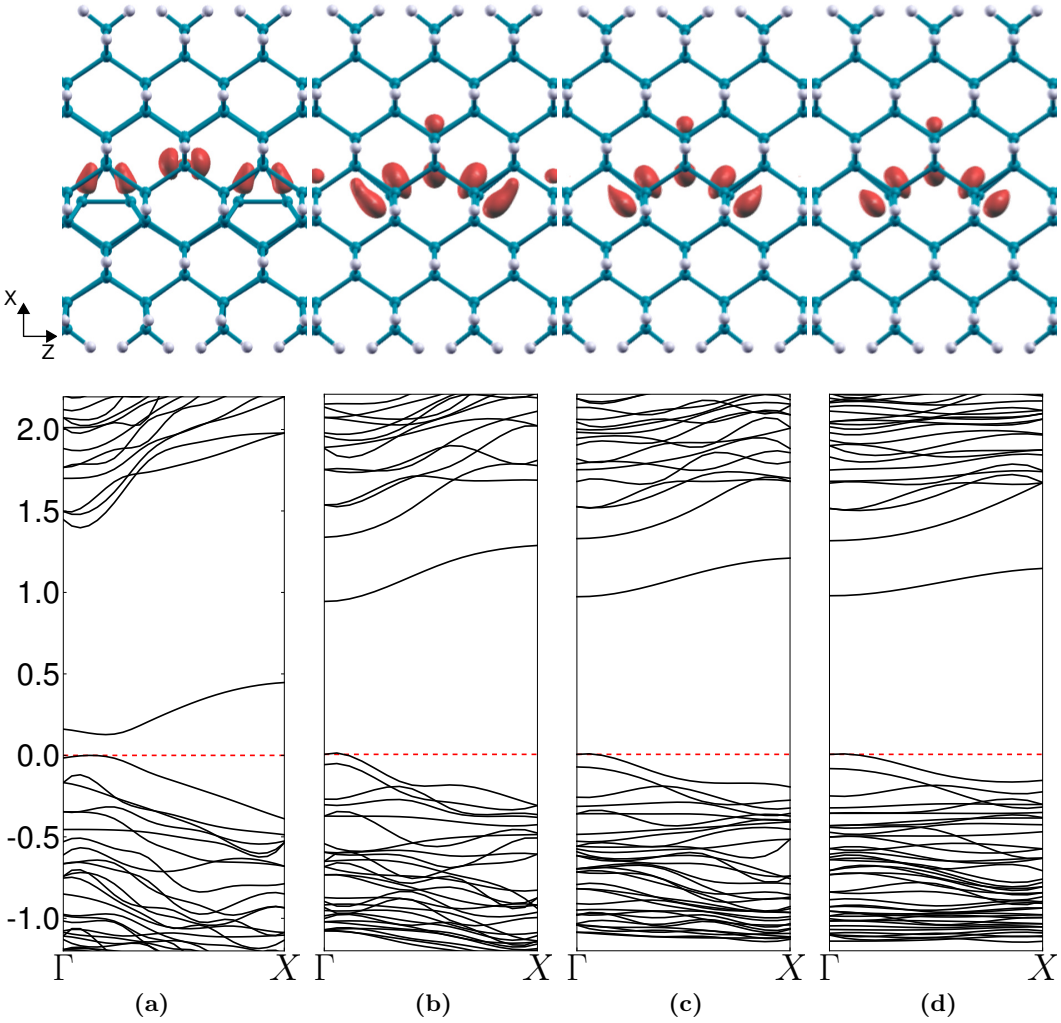

Figure 4.2: Section view of the Se defect wavefunction square modulus in nanowire NW9 (top) and its band structure (bottom) for increasing length of the supercell. The Se atom is on the axis of the nanowire (at the center of each cell depicted) and the distance to its replicas is about (a) 0.8 nm, (b) 1.2, (c) 1.6 and (d) 2.0 nm, i.e. multiple integers of the size of the nanowire unit cell. The fictitious interactions are reduced as the size of the supercell is increased.

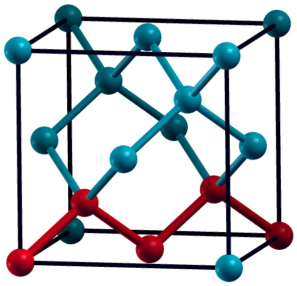

Figure 4.3: Cubic unit cell for bulk silicon. The atoms in red highlight the path connecting the defects along the [110] direction. No such simple path can be found along the [100] and [111] directions. The shading of the atoms is given as a help to understand the depth of the figure.

between defects from 1.2 to 2 nm. In the case of the supercell with L_z equal to 0.8 nm the formation energy is much smaller, because of the strong interaction of the selenium atoms. Also the band structure provides useful informations. As can be seen in Figure 4.2a the defect level is really close to the valence band and alters the band structure moving the VBM away from the Γ point, highlighting its anomalous condition. In the other cases the defect level is below the conduction band, with a dispersion that arises from having a periodic array of selenium atoms along the axis of the nanowire. This dispersion can be used as an estimation of the spurious interactions. This dispersion, again, is only 0.047 eV for [001] oriented nanowires with $L_z \simeq 1.6$ while it is 0.16 eV in the case shown in Figure 4.2d, further confirming the fact that [011] nanowires favour the interaction between the fictitious replicas of the defect.

A simple explanation for this phenomenon can be obtained from the analysis of the bonds structure along the axis of the nanowire. To this purpose consider the cubic unit cell of bulk silicon in Figure 4.3. We can see that along the [110] direction the atoms have a continuous simple path connecting two arrays of atoms (highlighted in red). This broken line is exactly were the defect wavefunction is spread in Figure 4.2 and in particular in Figure 4.2a. We can thus suppose that these bonds act as a bridge to increase the interactions between the dopant atoms when the symmetry of the system is oriented in this direction. In contrast, no such spread of the defect wavefunction occurs in the {011} directions in bulk silicon probably as a consequence of the symmetries of the full crystal, which constrains the wavefunction. From Figure 4.3 it is evident that a similar path is not present along the edges and the diagonals of the cube, i.e. {001} and {111} directions, respectively, preventing a simple spread of the defect wavefunction along the [001] and [111] oriented nanowires. Although this behaviour is similar in the case of a sulphur defect, a wider class of dopant atoms and longer supercells should be considered to validate this hypothesis, but this is beyond the scope of this work.

Anyway, as already stated previously, the main focus of this work is on nanowires grown along the [001] direction and the [011] oriented nanowires have been considered only as comparison for the study of the dependence of the electronic properties on the nanowire orientation. Our results can then be considered reliable for [001]

nanowires, while for the [011] case the results should be analysed keeping in mind that the defect may not be considered as fully isolated from its replicas.

As a last remark, it should be pointed out that, in addition to its relevance in determining the minimum length of the supercell, this feature can be of some interest also from the experimental point of view. In fact, even if the defects are not arranged on a line like in our simulations, the particular structure of [011] oriented nanowires can favour the interaction between dopants in various position of the nanowire cross section, causing different behaviour of electronic properties of the defect depending on the orientation of the nanowire.

4.2 Structural properties

For all the nanowires presented in Chapter 3, with or without surface reconstruction and with different orientations, we have studied the electronic properties of defects at the center of the nanowire. In all these cases the defect are located on the axis, except for the [011] oriented nanowires, NW8 and NW9, that does not have any atom on the axis (see Figure 3.6). For this orientation we thus use the term central position referring to the atoms that are the closest to the axis of the nanowire. Moreover, since we are interested in establishing the effect of the surface on the defect, we have also considered different defect positions for [001] oriented nanowires with surface reconstruction, NW1, NW2 and NW3, limiting only to substitutional defects. All the positions considered are numbered in Figure 4.4 and consist mainly, in addition to the central position, of surface (direct contact with passivating atoms) and subsurface (near surface but not in contact with passivating atoms) positions. With respect to Figure 4.4, the subsurface and surface positions correspond to label 2 and 3 for nanowires NW1 and NW3, and to label 3 and 4 for NW2, repsectively. We should point out that all these position and diameters have been explored for selenium defect, while, in the case of sulphur, only some selected configurations have been taken into account.

The insertion of the defect in place of some silicon atom causes an alteration of the local structure of the nanowire during the relaxation of the system. The features of this alteration can depend on many different factors, like the symmetry of the system with respect to the substitutional atoms, the disposition and the chemical properties of the other atoms surrounding the defect and clearly also the dimensions and the electronic properties of the defect itself. We will see that all these factors are important in the description of our system.

We have observed that in presence of a substitutional chalcogen atom at the center of the nanowire the core silicon atoms tend to expand their radius, moving away from the defect. Being surrounded by many layer of silicon, the defect in central positions is still constrained by the symmetry of the surrounding structure. To quantify the relaxation induced by the defect on the whole radial structure of the nanowire, we consider again the variation in the radius of each shell, as introduced in Chapter 3. Here, we define the variation Δr_{shell} not as the difference from the radius of the bulk atomic positions, but from the value obtained after the relaxation of the pristine nanowire r_{pristine}

$$\Delta r_{\text{shell}} = r_{\text{shell}} - r_{\text{pristine}}. \tag{4.1}$$

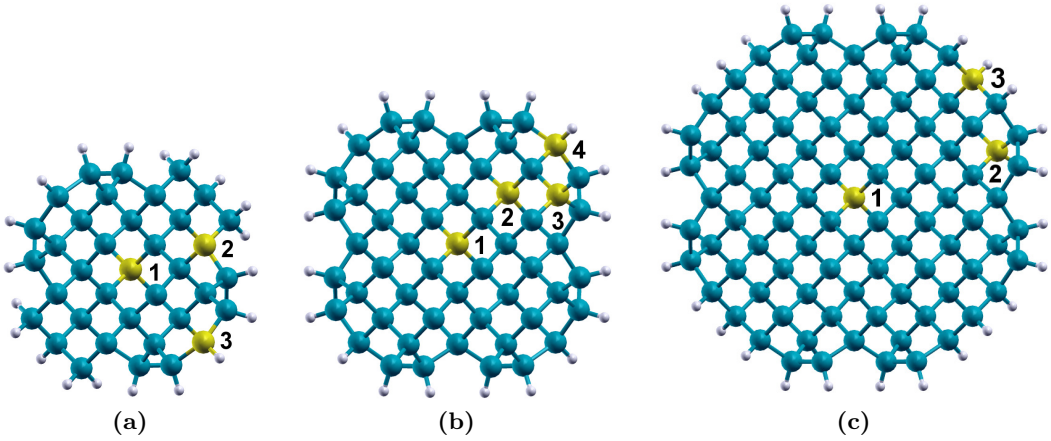

Figure 4.4: Section view of the [001] oriented silicon nanowires with surface reconstruction (a) NW1, (b) NW2 and (c) NW3. The yellow atoms indicates the dopant atom positions that have been studied with the respective label. Note that every position has been analysed separately; we did not consider simultaneous doping of more than one chalcogen atom.

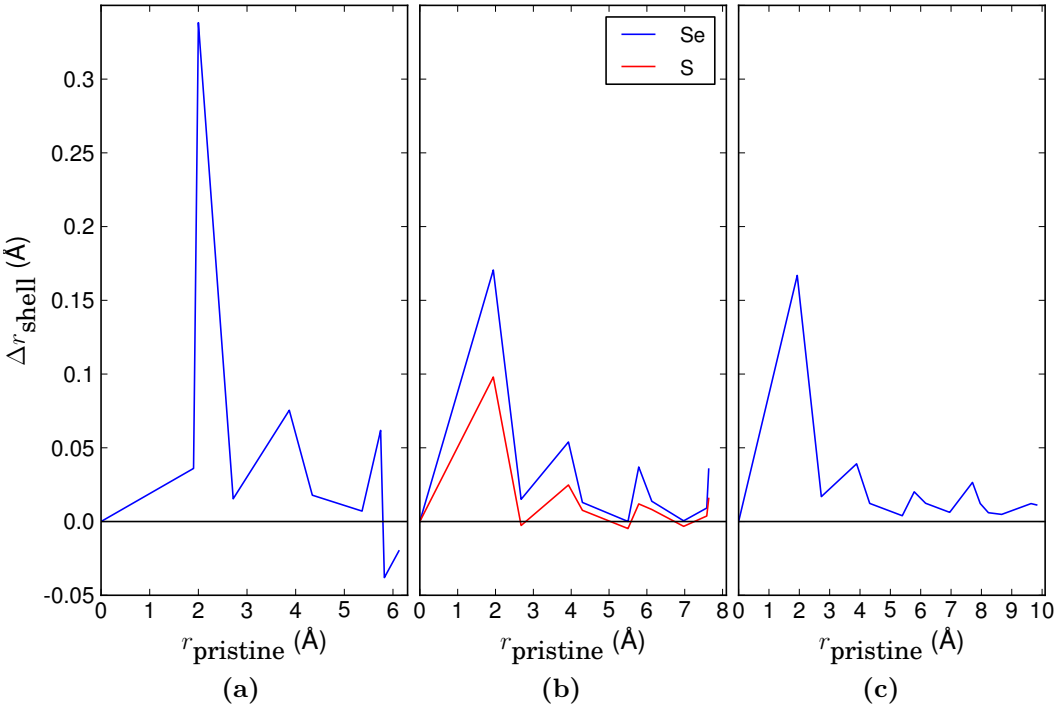

Figure 4.5: Change of the radius of each shell Δr_{shell} (equation (4.1)) as a function of the initial radius of the shell for (a) NW1, (b) NW2 and (c) NW3. Blue lines are for the nanowires doped with selenium atom, while the red line in (b) is for the case of a sulphur atom.

In Figure 4.5 we report the value of Δr_{shell} for the shells of [001] oriented nanowires. Defining a_{NW} as the length of the supercell of the pristine nanowire, only those atoms that are less than $a_{\text{NW}}/6$ from the defect along the axis of the nanowire have been considered. It can be noted that the effect of the relaxation is almost equivalent for nanowires NW2 and NW3, while it is quite anomalous for NW1. This is the first of a series of consequences of the surface distortion on the properties of the defect. Given the small diameter of the nanowire, the asymmetry at the surface has a strong influence on the local relaxation near the impurity. The four nearest neighbours in tetrahedral position split in two different shells, two atoms are closely bonded to the defect and do not change significantly their radius, while the other two drift away from the axis. On the whole, the resulting local structure affects also the shape and the orientation of the donor wavefunction and this will reveal to be a key point in determining the particular properties of the defect in NW1 compared to the bigger nanowires.

For nanowire NW2 we have considered a sulphur defect in addition to selenium. In Figure 4.5b the comparison between the relaxation of the two chalcogens shows that they modify the shell distribution with the same pattern. The only difference is in the magnitude of the displacement, which is smaller for sulphur. This is consistent with the smaller dimension of the sulphur covalent radius, compared to selenium. We expect that similar results would have been obtained if sulphur would have been used to dope NW1 and NW3.

In the case of central defect the relaxation affects only the first shells, leaving the external structure almost unchanged, and the displacements are small compared to the bond length. The interaction with the surface occurs only as a consequence of the symmetry of the system. When the dopant atom is in a surface or sub-surface position it can interact directly with the surface and with the passivating atoms. We have verified that these interactions change the structure of the system, but this deserves a separate discussion about the properties of chalcogen-hydrogen complexes.

4.2.1 Surface impurities: chalcogen-hydrogen complexes

The existence of chalcogen-hydrogen complexes in bulk silicon has been verified experimentally with the aid of several techniques, including EPR [99, 100], Fourier transform infrared spectroscopy [101], DLTS [102] and time-dependent conversion electron Mössbauer spectroscopy [103]. From a theoretical point of view a stable antibonding configuration and a metastable bond centered location have been identified for the hydrogen atom, with substitutional chalcogen atom [104, 105]. Note that, in this context, the term antibonding refers to the position of the hydrogen atom located along the $\langle 111 \rangle$ direction at a distance from the defect that is greater than $\sqrt{3}a_0/4$, i.e. beyond the defect nearest neighbour.

In the case of selenium, EPR measurements [100] have shown the presence of two different spectra with Se atom occupying a substitutional site in silicon and theoretical DFT calculations have determined that these can be both assigned to the configuration with H in the antibonding location [105]. We have reproduced this result using our pseudopotentials and a cubic supercell of 216 silicon atoms. The final antibonding configuration that we have obtained is displayed in Figure 4.6.

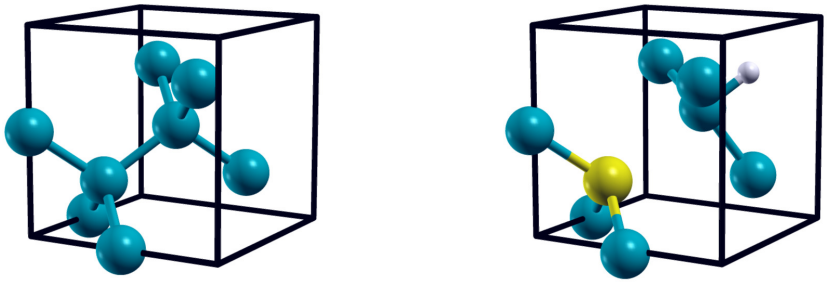

(a) **(b)**

Figure 4.6: Comparison between (a) the pristine crystal structure and (b) the complex Se-H defect in bulk silicon in the antibonding configuration. The cubic unit cell has been translated in order to underline the displacement of the silicon atom bonded to the hydrogen. After the relaxation the Se atom has only three silicon nearest neighbours.

The most interesting feature for our study is the breakaway from the selenium of the silicon atom close to the hydrogen, with a subsequent loss of the tetrahedral symmetry close to the defect.

The existence of chalcongen-hydrogen complexes in silicon is of great importance in our study, since when the defect is located near the surface of the nanowire it can interact with H passivating atoms, allowing the formation of complexes of this kind. This phenomenon has not been recognized for all the location close to the surface that we have considered, but in a particular case, that is position 3 of NW2, it seems evident that a mechanism similar to that of the complex formation is at work. In this configuration the selenium defect is in the subsurface position, meaning that one of its silicon nearest neighbours is in contact with an hydrogen atom. During the relaxation of the system we have observed that this Si-H couple moves apart from the Se atom, leading to a structure that resembles the one of Figure 4.6b. In Figure 4.7 we can see that, in the relaxed nanowire, the selenium defect is much more closer to only three of the four silicon nearest neighbours compared to the silicon atom bounded to the hydrogen, like for the complex defect in the bulk crystal. It can be noted that in our system the hydrogen atom is not located along the antibonding direction, but this can be attributed to the initial structure of the system and should not invalidate our conclusions.

The local deformations for defects located near the surface of the nanowire can thus be very different from those induced by a defect in the core, where the tetrahedral symmetry is usually preserved. This contrast between the local structure at different defect locations affects also the shape of the defect wavefunction and is the base for the differences in the electronic properties that we will show.

We didn't perform any calculation with sulphur defect at the surface of the nanowire. However, although experimental [100] and theoretical [105] results demonstrated that both antibonding and bond centered configurations can be found for S doped silicon, inside the nanowires we don't have any starting configuration with the hydrogen atom in the bond centered location. Therefore we expect that sulphur doped nanowires will show no qualitative difference with the case of selenium.

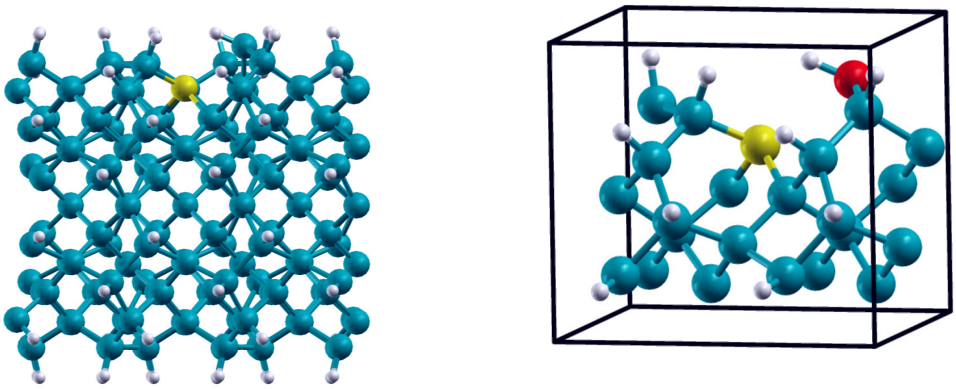

(a) (b)

Figure 4.7: Side view of relaxed NW2 with Se defect in position 3. In (a) the complete supercell is shown, while in (b) only few atoms are displayed. Here, the cubic cell depicted in (b) serves only to clarify the perspective view and is not related to the nanowire supercell. The silicon atom which moves apart from the selenium defect is highlighted in red. This structure should be compared with that in Figure 4.6.

4.3 Defect formation energy

In order to determine the most favourable position inside the nanowire and to check the possibility of doping silicon nanowires at different diameter, we studied the energy required to replace one of the silicon atoms with a chalcogen atom. This energy can be used also to establish the charge state of the defect. The standard way to express this quantity is the formation energy as is formulated by Zhang and Northrup [106]. The formation energy for a generic defect in a system is defined as

$$E_{\mathrm{f}} = E_{\mathrm{D}} - E_{\mathrm{pristine}} - \sum_i n_i \mu_i + q(\varepsilon_{\mathrm{V}} + \mu_{\mathrm{e}}), \tag{4.2}$$

where E_{D} and E_{pristine} are the total energies of the defective and pristine systems, respectively, n_i is the number of atoms of species i added or removed to create the defect D and μ_i is the corresponding chemical potential of the reservoir. If the defect is charged, q indicates the charge state of the defect, ε_{V} is the top of the valence band and μ_{e} is the chemical potential for electrons.

In our specific case we need to add a chalcogen atom and remove the corresponding silicon atom in a nanowire, so equation (4.2) reduces to

$$E_{\mathrm{f}} = E_{\mathrm{D}} - E_{\mathrm{pristine}} + \mu_{\mathrm{Si}} - \mu_{\mathrm{chalcogen}} + q(\varepsilon_{\mathrm{V}} + \mu_{\mathrm{e}}). \tag{4.3}$$

Rurali and Cartoixà [72] have pointed out that this expression has been formulated for bulk systems and assumes that the atom removed to create the defect is added to the crystal. However, while in a bulk crystal all the positions are equivalent, this is not true for a one dimensional system like a nanowire. They have thus devised an expression based on the microscopic structure of the nanowire, considering the formation of n_{Si} defects instead of a single defect, where n_{Si} is the number of

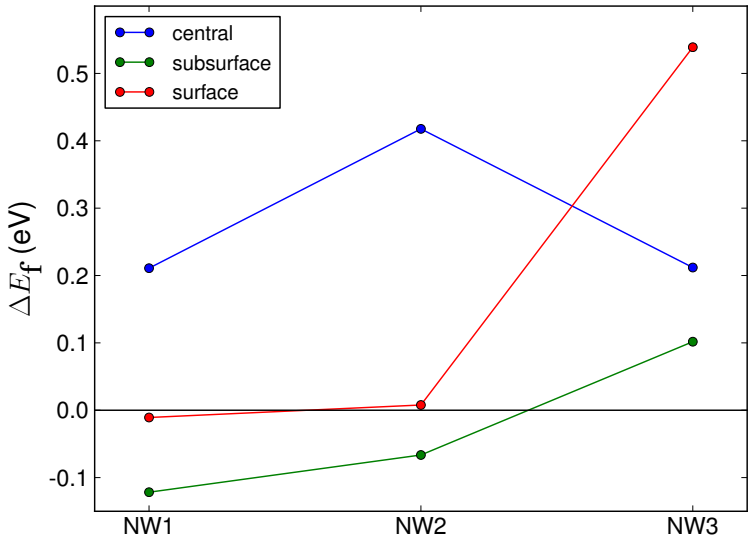

Figure 4.8: Relative formation energy (equation (4.4)) for central (blue), subsurface (green) and surface (red) Se defect position depending on the nanowire diameter. The zero value indicates the formation energy of the Se defect in bulk silicon. The subsurface position is the most stable configuration for all the nanowires.

silicon atoms in the unit cell of the nanowire (see Appendix A for the details of this correction). Despite its interest, we have applied this correction for some nanowires doped with selenium and we have found that in our case its contribution is negligible. For example the formation energy calculated for Se doped NW1 including this correction differs by only 0.006 eV from the value obtained using the simpler equation (4.3) with μ_{Si} being the chemical potential of bulk silicon and $\mu_{\mathrm{chalcogen}}$ the chemical potential of an isolated selenium atom extracted from a simulation with the same approximations. As we will show below, this quantity is much smaller than the differences that we have observed in the formation energies for different configurations, so we have decided to omit this correction from our final results.

Since we are interested in comparing the properties of the defect in the positions of Figure 4.4, we can limit ourselves to study only the differences between formation energies. All the values will be expressed as differences from a reference value, which is chosen to be the formation energy of the Se defect in bulk Si obtained from our calculations:

$$\Delta E_{\mathrm{f}} = E_{\mathrm{f}}(\text{nanowire}) - E_{\mathrm{f}}(\text{bulk}). \tag{4.4}$$

In this way we do not have to include in the calculation the chemical potentials of silicon and of the chalcogens.

4.3.1 Neutral defect

We start considering the formation energy for neutral defects, which is obtained setting q equal to 0 in equation (4.3) and we focus on the dependence on the diameter

of the nanowire and on the position of the defect. The results obtained from our simulations can be seen in Figure 4.8, where ΔE_{f} is plotted as a function of the three nanowires NW1, NW2 and NW3 for each kind of defect position. From these values we can see that there is a tendency to surface segregation and, in particular, the subsurface position is always the energetically most favourable, in agreement with calculations performed on other impurities (P, B) [51, 52]. Still, this tendency depends strongly on the nanowire radius and especially on the deformations near the surface. In fact, in NW1 the relaxation of the surface and the consequent reduction of the symmetry are probably responsible for a reduction of the formation energy even for the defect in the central position. Defining the segregation energy as the difference between the formation energy of the defect in the core and in the subsurface position, we see that decreasing the size of the nanowire from NW2 to NW1 the segregation energy decreases to 0.33 eV, a fact that is against what is usually obtained for the segregation energy in nanowires and nanocrystals and that can be explained by the deformations of the structure of NW1. The maximum value of the segregation energy for the nanowires considered here is 0.48 eV and is found in NW2. This can be ascribed to the fact that for NW2 the surface does not affect the core of the nanowire, while at the subsurface position there is a reduction in the formation energy related to the presence of what we have recognized to be a Se-H complex. In NW3 it is evident that the central position is no more the least favourable among those considered, as it is for NW1 and NW2 and the segregation energy is reduced to 0.11 eV. In fact, as the nanowire diameter becomes larger, the formation energy of central defect tends to the bulk value (the reference value in Figure 4.8). Moreover, it is probable that, as the diameter of the nanowire is increased, the system becomes more resistant to local relaxation, increasing the formation energy of the defect near the surface. A feature not immediately evident from the way in which the data are presented in Figure 4.8 is that the formation energy of the defect on the axis for NW1 and NW3 are almost identical. After some analysis we have concluded that there is no deeper meaning behind this matching values and this should just be due to a numerical coincidence.

It is also worth mentioning that for nanowires with small diameter, alteration of the tetrahedral symmetry brings the formation energy of the defect with Se close to the surface below the value that we have obtained for the defect in the bulk. This suggests that the contribution to the energy originating from the deformation overcomes the one coming from confinement inside the nanowire. However, one needs to be careful in drawing conclusions, since, if the formation of complexes is important in determining the segregation behaviour, the choice of different passivation mechanisms could change these results significantly.

The comparison between the data for different orientations and dopant atoms is not as straightforward as for the previous cases, since, even though the diameters of corresponding nanowires have been chosen to be as close as possible, the exact value can vary of about 10% (in particular NW11). The results thus follows from a combined effect of the changes in growth direction and in nanowire size. For this reason we report the calculated values in Table 4.1 and not in graphical form. We have considered nanowires with diameter of about 0.8 nm and 1.5 nm, for both Se and S defect and for all the orientations. However, we should pay a particular attention for the nanowire NW8. In fact, as can be seen from Figure 3.6a, the

nanowire	d (nm)	ΔE_{f} Se (eV)	ΔE_{f} S (eV)
[001]			
NW4	0.84	0.56	0.51
NW2	1.52	0.42	0.25
[011]			
NW8	0.84	0.36	0.29
NW9	1.51	0.18	0.13
[111]			
NW10	0.83	0.54	0.52
NW11	1.67	0.23	0.17

Table 4.1: Relative formation energy (equation (4.4)) for defects on the axis of nanowires with orientation [001], [011] and [111]. The diameter allows to match nanowires with similar dimensions.

central defect is not on the axis of the nanowire and is placed quite close to the surface, which perturbs slightly the local structure of the defect. This, combined with the strong interaction between replicas of the defect that we have discussed above for [011] nanowires, can make NW8 less reliable for comparison with NW4 and NW10 when studying donors in central position.

From the data in Table 4.1 we can see that the relative formation energy ΔE_{f} is always smaller for sulphur defect with respect to selenium, meaning that when moving from bulk silicon to a nanowire, the increase in the doping difficulty is higher in selenium than in sulphur. For completeness, we report that the formation energy of selenium and sulphur in bulk crystal, calculated within our approximations, are 1.31 eV and 1.26 eV, respectively. We can see that the formation energy for Se is greater than that of S, in agreement with other calculations present in literature [105, 107]. These values have been calculated using our results of the energy per atom of solid monoclinic α-S and α-Se as μ_{S} and μ_{Se} in equation (4.2). However, the formation energy is strongly dependent on the chemical potential, as we have verified replacing the energy per atom in a crystal with the total energy of an isolated atom. Therefore, when dealing with the comparison of systems with different properties, it is better to keep working with differences in the defect formation energy, as we have done so far.

Concerning the dependence of the formation energy on the orientation of the nanowire, the results suggest that the [011] orientated nanowires are the easiest to dope. This conclusion can however be questioned, based on the discussion of Section 4.1, since the residual interaction between the defect and its replicas can bias the final value of the formation energy. Nonetheless, given that the difference in the formation energy between different orientations is more than 20% and the trend in the formation energy as the distance between the defect is increased, we expect that this advantage in the case of [011] orientation will be preserved even using longer supercells which reduce the fictitious interactions.

At small diameter we see that the formation energy is almost equal for both [001]

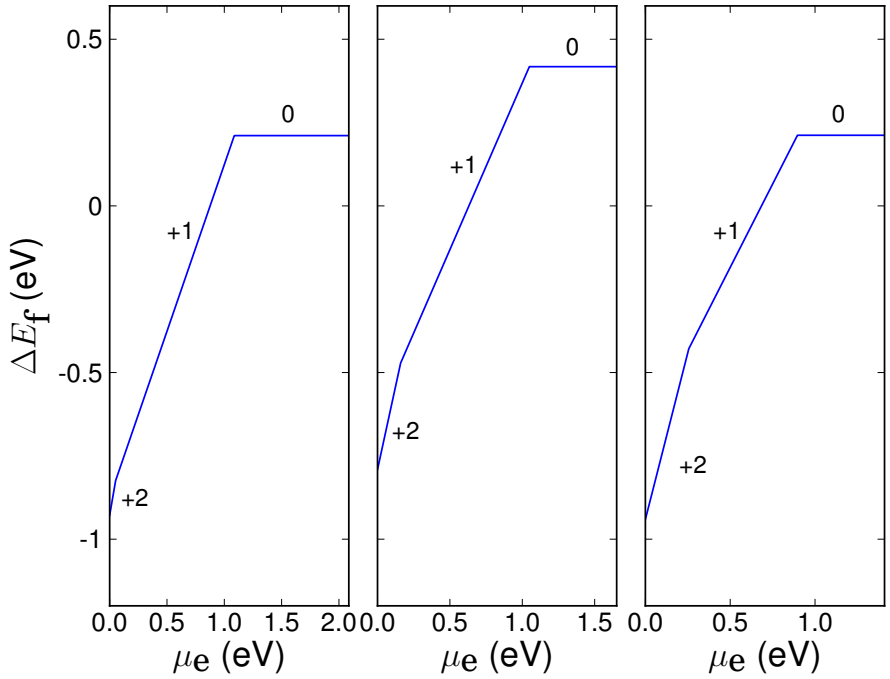

Figure 4.9: Relative formation energy (equation (4.4)) for NW1, NW2, NW3 depending on the electron chemical potential μ_e. μ_e ranges in the band gap of each nanowire. Different charge states correspond to different slopes. The reference value of ΔE_f remains the formation energy of the neutral defect in the bulk.

and [111] orientations. However this fact changes when the diameter is raised up to 1.5 nm, as the formation energy of the chalcogen defects in NW2 is about twice that in NW11. A contribution to this result can come from the difference between the diameters of NW2 and NW11, while NW4 and NW10 have approximately the same size, but this is not sufficient to explain this discrepancy. We thus conclude that the at small sizes the role of quantum confinement is crucial in determining the formation energy and its effect overcomes the one coming from the orientation of the nanowire, while at larger diameters the differences induced by the orientation can emerge as a relevant factor.

Note that all these trends regarding the nanowire orientation are the same for both selenium and sulphur dopants.

4.3.2 Charged defect

Since one of the aims of this work is the inspection of the hyperfine parameters, which are different from zero only for Se^+ and S^+ defect, the study of the formation energies for the charged states can provide useful information. This has been done only for a selenium defects on the axis of the nanowire, in order to isolate as much as possible these values from the influences of the surface deformations. Moreover, we have considered only [001] oriented nanowires with initial surface reconstruction,

since we do not expect that the change in surface reconstruction and orientation should alter qualitatively our conclusions.

The ionization energy is the energy required to remove an electron from the system and is thus defined as the difference of total energy calculated after and before the removal of a single electron, in our case

$$I(N) = E_{\mathrm{D}}(N-1) - E_{\mathrm{D}}(N), \tag{4.5}$$

where N is the number of electron in the system. Recently, Niquet et al. [108] have questioned the validity of this approach in the framework of DFT for semiconductor nanostructure if the neutral impurity is used in the calculation, due to the lack of screened exchange in LDA and GGA functionals[1]. They have then verified their conclusions studying the binding energy of a defect in silicon nanowires, confirming the presence of an underestimation compared to the GW calculations. Nonetheless, our results here reported can be used to extract qualitative behaviour of the ionization energy.

As expected from the confinement effect the first ionization energy $E(0/+)$ increases noticeably from 0.31 eV in NW3 to 0.88 eV in NW2, while it decreases to 0.49 eV in NW1. Again, this should be ascribed to the high influence of the surface deformations occurring during relaxation in NW1. A further confirmation to this comes from the fact that reducing the diameter of the nanowire and removing the surface reconstruction, we obtain a ionization energy of 2.18 eV for NW4. The second ionization energies $E(+/++)$ are 3.83 eV, 1.52 eV, 1.77 eV and 0.95 eV for nanowires NW4, NW1, NW2 and NW3, respectively.

In Figure 4.9 the formation energies ΔE_{f} for the charged defect are shown as a function of the electron chemical potential μ_{e}. Only the charge state that gives the lowest formation energy with respect to the Fermi energy is shown. Change in the slope therefore indicates transitions to a different charge state. As can be seen, for all the nanowires there is a wide interval in the values of μ_{e} for which the defect in the singly ionized charge state is the most stable.

We have thus established that in our nanowires the Se^+ charge state can be attained tuning the Fermi level of the system. This is of key importance since demonstrates that it is possible to measure experimentally the hyperfine parameters for chalcogens donors in this kind of nanowires.

4.4 Band structure

To conclude this chapter we report the band structures that we have calculated for nanowires with different diameters, orientations and defect positions that we have discussed above. All of these band structures have been calculated with the defect in a neutral charge state and the Fermi level is then at the top of the defect band. In our plots we set the zero value at the top of the valence band, like for pristine nanowires, in order to have a common term of reference.

Figure 4.10 shows the comparison of the band structure for [001] nanowires with diameters ranging from 1.2 nm to 2 nm. We see that the main effect of the dimension

[1]This has been demonstrated for the binding energy, the energy required to bring an electron to the conduction band, but the calculation of ionization energies suffers from the same deficiencies of the functionals.

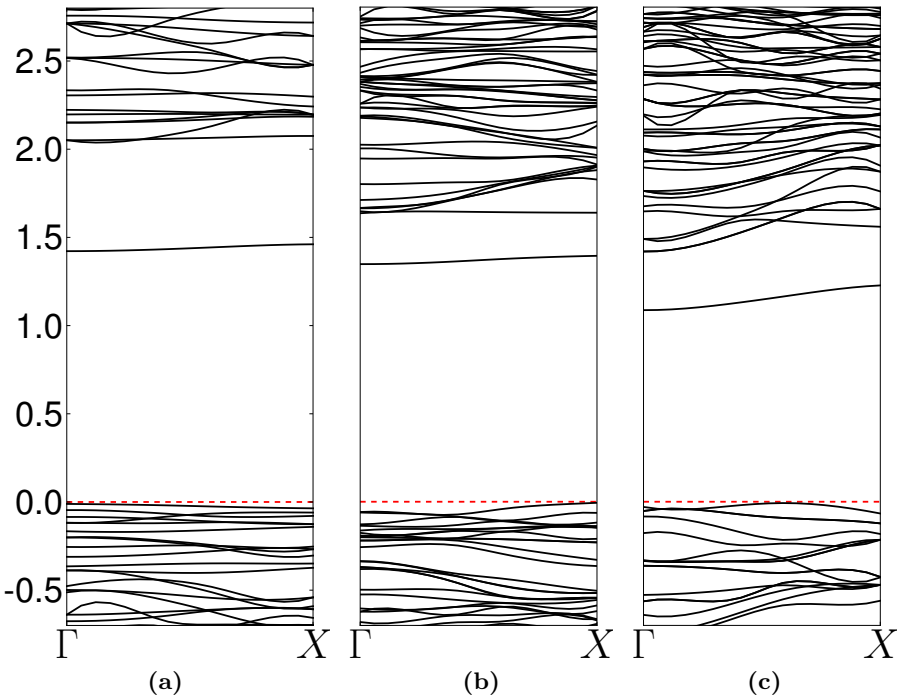

Figure 4.10: Band structure along the axis for [001] oriented nanowires (a) NW1, (b) NW2 and (c) NW3 with Se defect at the center of the nanowire. The horizontal dashed lines represent the top of the valence band.

on the defect level is to increase the depth of the level for small nanowires. Thus, in this case, the deformation of the wavefunction due to the surface reconstruction in NW1 does not prevent the quantum confinement effect to make the defect deeper than in bigger nanowires. This trend finds further confirmation in the band structure of the small nanowire NW4 (not shown here), even if prepared with a different passivation procedure. The dispersion of the defect band is quite small in all of these cases, with a value which is of a few hundredth of electronvolts for NW1-NW3 and drops to 0.008 eV for NW4. Comparing these dispersions with those of nanowires without surface reconstruction, we can deduce that the steep change that takes place between NW1 and NW4 can be ascribed to the different surface structure of the system.

In Figure 4.11 we report the band structure of the same nanowires of Figure 4.10 but with the defect in the subsurface position. It is evident that the effect of the interaction with the surface is to deepen the defect level, in particular for NW1 and NW2, where the donor band is shifted almost to the center of the band gap. This seems to be in contrast with the fact that in bulk crystal the complex chalcogen-hydrogen defect is shallower compared to the isolated chalcogen [105]. In this case, however, the system is influenced by the presence of the nanowire surface and of quantum confinement that increase the localization of the wavefunction and whose effect cannot be predicted easily. Hence this observation does not invalidate our conclusions of Section 4.2.1. From Figure 4.11c it can be seen that the deepening is instead less pronounced in NW3 compared to NW1 and NW2. This is in agreement

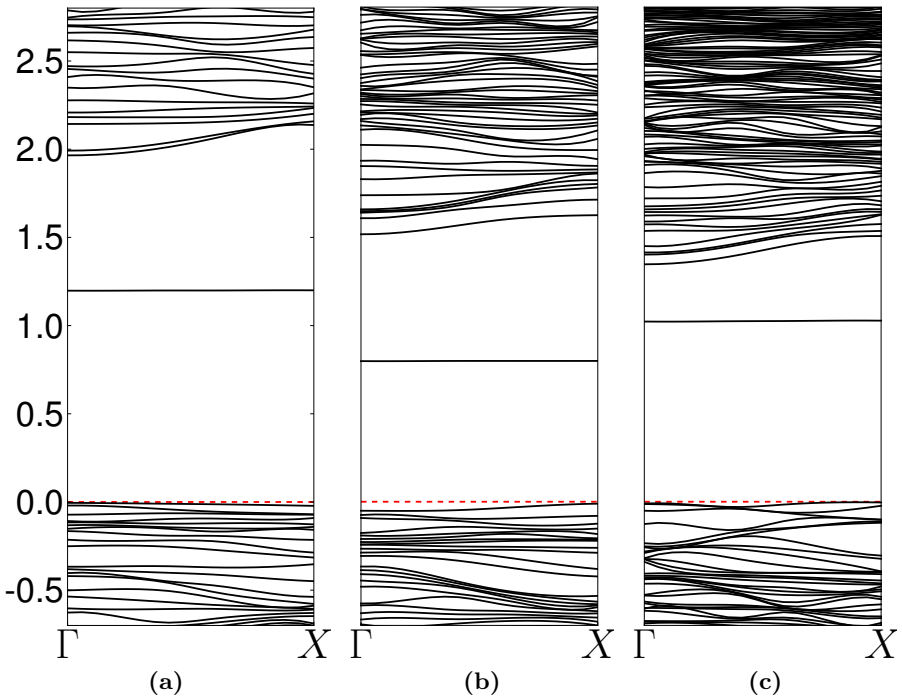

Figure 4.11: Band structure along the axis of the nanowire with Se defect at subsurface position, for nanowires (a) NW1 (position 2), (b) NW2 (position 3) and (c) NW3 (position 2). The horizontal dashed lines represent the top of the valence band.

with the increase of the formation energy for the subsurface position that we have obtained (see Figure 4.8) and that has been interpreted as a resistance to surface deformation in a nanowire with bigger diameter.

In this case the dispersion of the defect band is one or two orders of magnitude smaller, depending on the diameter, than for the defect on the axis of the nanowire. This suggests that there is almost no interaction between the defect and its replicas in this configuration.

We do not report graphically the band structure of the nanowires with the defect at the surface position. The results are similar to those obtained for the subsurface defect, with a deep donor level and a small dispersion of the defect band along the axis of the nanowire. The only remarkable difference is the deepening of the defect band in nanowire NW3.

Finally, in Figure 4.12 we compare the band structure of nanowires with diameter slightly bigger than 1.5 nm and a selenium defect on the axis of the nanowire for [001], [011] and [111] orientations. It is evident that the dispersion of the wavefunction is greater for NW9 (Figure 4.12c) even if the distance between the fictitious replicas of the defect is the highest among the various orientations, as already anticipated in Section 4.1. The depth of the level is almost the same for all the orientations with a slightly deeper level in the case of the [111] nanowire.

For the nanowires with sulphur defect that we have studied, we have found no qualitative difference in the band structure compared to the selenium defect. Given the similar nature of these two chalcogens, all the considerations drawn about the

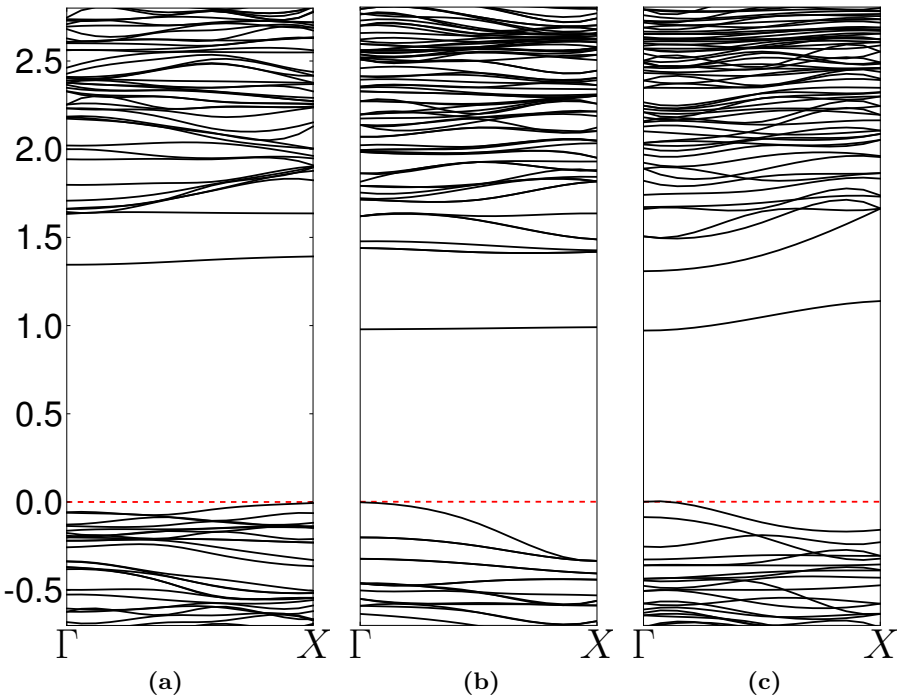

Figure 4.12: Band structure for nanowires (a) NW2, (b) NW11 and (c) NW9 along the axis of the nanowire with Se defect on the central position. The horizontal dashed lines represent the top of the valence band.

selenium defect so far should be applicable to the case of sulphur doped nanowires as well.

Chapter 5

Hyperfine structure

In the previous chapters we have seen that quantum confinement has a strong influence on the properties of pristine and doped nanowires. Here we want to verify that the confinement in the directions orthogonal to the nanowire axis can also modify the hyperfine structure of the donor. In this chapter we demonstrate that the confinement of the defect wavefunction can increase the hyperfine contact term compared to bulk silicon, but we also show the relevance of the interaction with the surface in the determination of its final value. In addition, we will present our results about the dependence of the hyperfine structure, in particular the anisotropic term, on the strain of the system.

5.1 The hyperfine interaction

In a solid, the hyperfine interaction is the interaction between the magnetic moment of the unpaired electron or hole, and the magnetic moments of the nuclei [109]. In our case, we consider the interaction of an electron with the nucleus of an impurity atom, hence the Hamiltonian is given by

$$\hat{H} = \hat{\mathbf{S}} \cdot \mathbf{A} \cdot \hat{\mathbf{I}}, \tag{5.1}$$

where $\hat{\mathbf{S}}$ is the electron spin operator, $\hat{\mathbf{I}}$ is the nuclear spin operator and $\mathbf{A}$ is a tensor describing the hyperfine coupling constant. The explicit form of this coupling constant can be obtained considering a single electron interacting with a fixed nucleus. The interaction between the two particles is given not only by the interaction between the two spin magnetic moment, but also by the interaction of the electron magnetic moment with the magnetic field seen by the electron, due to its motion relative to the nucleus. This last term depends on the electron orbital angular momentum and the classical Hamiltonian of the interaction is thus obtained as the sum of these two contributions [110]

$$H = \frac{e}{mc}\mathbf{p} \cdot \mathbf{V} - \mathbf{M}_e \cdot \mathbf{B}. \tag{5.2}$$

Here, $\mathbf{V}$ is the electromagnetic vector potential, $\mathbf{M}_e$ is the electron magnetic moment and the magnetic field $\mathbf{B}$ at a distance $\mathbf{r}$ from the nucleus is given by

$$\mathbf{B} = \mathbf{M}_N \delta(\mathbf{r}) \left(\frac{8\pi}{3}\right) - \frac{\mathbf{M}_N}{r^3} + \frac{3(\mathbf{M}_N \cdot \mathbf{r})\mathbf{r}}{r^5}, \tag{5.3}$$

where $\mathbf{M}_N$ is the magnetic moment of the nucleus.

After some calculations, the Hamiltonian can be represented in the form of equation (5.1) and the coupling constant $\mathbf{A}$ can then be divided into two terms

$$\mathbf{A} = a\mathbf{1} + \mathbf{A}_{\text{dip}}, \tag{5.4}$$

where

$$a = \frac{4\pi g_{\text{e}}\mu_{\text{e}} g_{\text{N}}\mu_{\text{N}}}{3\langle S_z\rangle} \int \mathrm{d}^3 r n_s(\mathbf{r})\delta(\mathbf{r}) \tag{5.5}$$

is the scalar Fermi-contact term that is obtained from the isotropic part of the Hamiltonian (5.2) and is determined by the electron spin density near the nucleus while

$$\mathbf{A}^{ij}_{\text{dip}} = \frac{g_{\text{e}}\mu_{\text{e}} g_{\text{N}}\mu_{\text{N}}}{2\langle S_z\rangle} \int \mathrm{d}^3 r n_s(\mathbf{r}) \frac{3r_i r_j - \delta_{i,j} r^2}{r^5} \tag{5.6}$$

is the dipolar tensor, which depends on the anisotropic part of the electronic spin density. Here, $n_s(\mathbf{r}) = n_\uparrow(\mathbf{r}) - n_\downarrow(\mathbf{r})$ is the electron spin density, g_{e} is the electron g factor, μ_{e} is the Bohr magneton, g_{N} is the nuclear gyromagnetic ratio of the nucleus, μ_{N} is the nuclear magneton and $\langle S_z\rangle$ is the expectation value of the z component of the total electronic spin. Since a is a function of $n_s(\mathbf{0})$, where $\mathbf{0}$ indicates the nucleus site, only the s-like part of the wavefunction contributes to its value.

The dipolar term $\mathbf{A}_{\text{dip}}$ is a traceless tensor and, in its principal axis system, is usually described by two independent parameters, uniaxiality b and asymmetry b', such that

$$\mathbf{A}_{\text{dip}} = \begin{pmatrix} -b + b' & & \\ & -b - b' & \\ & & 2b \end{pmatrix}. \tag{5.7}$$

These parameters vanish for systems with tetrahedral symmetry, like bulk Si, and b' describes the deviation of the system from axial symmetry.

The same parameters can be used to describe the so called superhyperfine interaction, that is the interaction between the host atom of the material (in our case silicon atoms) and the electronic spin density originated by the defect.

5.1.1 Relativistic correction

Since the hyperfine contact term is calculated from the value of the spin density near the core of the nucleus, where the relativistic effects are strongest, a relativistic correction can be important. In our specific case this is true, since the chalcogen donors we are dealing with are heavy atoms.

In a first order scalar relativistic treatment the contact term expression (5.5) is modified considering, instead of the simple value at the nucleus site $n_s(\mathbf{0})$, an average of the spin density for a sphere with a radius of the order of the Thomson radius

$$r_T = \frac{Ze^2}{m_e c^2}, \tag{5.8}$$

where Z is the nuclear charge [111, 112]. Note that this radius is much larger than the diameter of the nucleus itself. This is equivalent to replace the Dirac δ function

in equation (5.5) with a more extended radial function $\delta_T(r)$, defined by

$$\delta_T(r) = \frac{1}{4\pi r^2} \frac{r_T/2}{[(1 + E/2m_e c^2)r + r_T/2]^2}. \tag{5.9}$$

All our results presented here have been calculated applying this correction, but a discussion about its employment is given for the results in bulk silicon, because in that case experimental data are available for comparison.

5.1.2 Quantum information applications

In our case, the interest for the hyperfine structure arises from its possible applications, in particular for quantum information technology. This field of research is presently of high importance because extremely fast quantum algorithms have been devised for the solution of some specific problems [113]. Despite the effort that has been devoted, real-world quantum computers are still far from being achieved, due to the strict requirements that such a system should obey (scalability, universal logic and correctability)[114]. In order to obtain a scalable model for a qubit many different technological approaches are under consideration, like for example those based on spin, photons, trapped atoms and superconductors [115].

One of the most important ideas is the one proposed by Kane [116], which consists in storing the qubit in the nuclear spin of a donor in silicon. Among the others, one of the proposals based on Kane's scheme is the one by Berman et al. [117], which exploits the hyperfine interaction between the nuclear spin of the donor and the associated electron spin to control the qubit. In particular they propose the use of magnetic resonance force microscopy (MRFM) to control the qubit indirectly through the action on the electron spin. However, due to the large size of its electron cloud and relatively weak hyperfine interaction, phosphorus donor is not suitable for this proposal and the same authors have thus suggested the use of one of the chalcogen atoms, i.e. tellurium, as it has small electron cloud and a large hyperfine interaction [118].

In light of this and knowing that the effect of quantum confinement is to reduce the dispersion of the defect electron cloud, we aim to verify if other chalcogens, and in particular selenium, can fit this proposal once implanted in a nanostructure that can localize the donor wavefunction and increase the hyperfine interaction. As we will see this is possible only under specific conditions on the size of the nanowire and the position of the donor.

5.2 Donors in bulk silicon

Before beginning the study of hyperfine parameter in nanowires we have performed some calculations for the same defects in bulk silicon. This is useful as a test for the techniques that we have used, as a term of reference for the results in nanowires and also as a tool to understand the experimental results that can be obtained in bulk silicon by means of EPR measurements. Here we report our results for sulphur and selenium defect.

In Table 5.1 we report the calculated hyperfine and superhyperfine parameters and a comparison with experimental results available in literature [119, 120]. The

Shell	a_{calc}	a_{exp}	b_{calc}	b_{exp}	b'_{calc}	b'_{exp}
S^+_{Si}						
S^+	313.8	312.4	0	0	0	0
111						
Si(1,1,1)	39.39	32.7	12.67	12	0	
Si(3,3,$\bar{3}$)	2.93	8.94	0.01	0.62	0	
Si(4,4,4)	0.72	2.94	0.01	0.02	0	
100						
Si(4,0,0)	1.95	2.04	-0.07	0.05	-0.01	
110						
Si(2,2,0)	-3.52		-0.13		-0.12	
Si(3,1,$\bar{1}$)	3.93	3.84	0.46	0.42	0.12	
Si(3,3,1)	7.58	4.77	0.61	0.03	0.19	
Si(4,4,0)	9.73	8.94	0.55	0.47	0.03	
Se^+_{Si}						
Se^+	1326	1658	0	0	0	0
111						
Si(1,1,1)	33.99	28.89	12.94	12.52	0	
Si(3,3,$\bar{3}$)	3.08	9.63	0.01	0.57	0	
Si(4,4,4)	0.97	1.24	0.01	0.09	0	
100						
Si(4,0,0)	2.88	3.13	-0.08		-0.01	
110						
Si(2,2,0)	-2.81		-0.23		-0.15	
Si(3,1,$\bar{1}$)	4.15	3.87	0.5	0-45	0.11	-0.11
Si(3,3,1)	6.6	4.27	0.48	-0.11	0.18	-0.11
Si(4,4,0)	9.87	7.54	0.55	0.52	0.03	0.13

Table 5.1: Hyperfine and superhyperfine structure of sulphur and selenium defect in bulk silicon. The results for contact term a, uniaxiality b and asymmetry b' are classified based on the symmetry and the shell. The experimental data used for comparison are taken from Ludwig [119] for S and Gruelich-Weber et al. [120] for Se. Missing values means that there are no data available for these parameters. All the data are expressed in MHz.

superhyperfine data are classified depending on the type of the shell, i.e. 111, 100 or 110, which are the symmetries that can be distinguished in EPR measurements. A shell is composed of a group of equivalent lattice sites which have the same value of the contact term a and each one is labeled by the standard notation (i, j, k), where the numbers in parenthesis indicates the coordinate of the atom in multiples of $a_0/4$, a_0 being the silicon lattice parameter [121]. Since in EPR experiment it is not possible to determine the distance of the shell with respect to the donor site, we compare our calculated data with the experimental data for which the contact interactions are largest.

The most interesting part of this comparison is for the hyperfine interaction. In bulk silicon the anisotropic term is zero for symmetry reasons, so we have to compare only the contact term. We see from the data in Table 5.1 that we have a very good agreement in the case of sulphur, while for selenium defect the theoretical calculation underestimates the real value of about 20%. These results suggest that the we can calculate the hyperfine contact term within a good approximation, but the use of scalar relativistic correction described above deserves some comments. Although this correction is suitable when working with an heavy atom, like selenium, we found that its contribution is almost negligible for silicon atoms and it changes the value of the contact term of less than 10% for sulphur, while its effect in the case of selenium is considerable. In fact, neglecting this correction for selenium leads to an overestimation of about 20% of the contact term (1953 MHz) compared to the experimental value, while we have seen that taking it into account causes an underestimation of approximately the same amount. We have decided to apply the relativistic correction in light of the improvement brought to the results, like in the case of sulphur defect.

The superhyperfine data show that we have a good agreement with the experimental results in the isotropic and dipolar terms when considering the defect nearest neighbours (shell Si(1,1,1)) for both sulphur and selenium defects. For other shells far from the defect we have obtained some good results, like in the case of Si(4,0,0) and Si(3,1,$\bar{1}$), but also some data that do no match the experiments very well, like Si(3,3,$\bar{3}$). To explain this it should be kept in mind that as the distance from the original defect is increased, the shells get closer to the replicas of the defect in the neighboring supercell. In the limiting case, when a silicon atom is at half of the supercell it is in the middle between two defects. The superhyperfine parameters are thus altered by the fact that the defect cannot be considered completely isolated. The relevance of the supercell size has been verified also by studying a bismuth defect in a supercell with a side of 1.64 nm. Even if this donor is deep, in our simulations the donor band has a strong overlap with the conduction band, signaling the interaction between the defect and its replicas. As can be expected, the calculations of the hyperfine structure have a poor agreement with the experimental data [122], even for the contact term of the bismuth, and a larger supercell is necessary to obtain meaningful results.

Unfortunately, few experimental data are available for the asymmetry term b', and these are only for the shells where we obtain the worse results even for a and b, making hard to check the reliability of the calculated values.

In conclusion we have verified that our method allows the calculation of hyperfine and superhyperfine parameters in bulk crystal, at least in the proximity of the

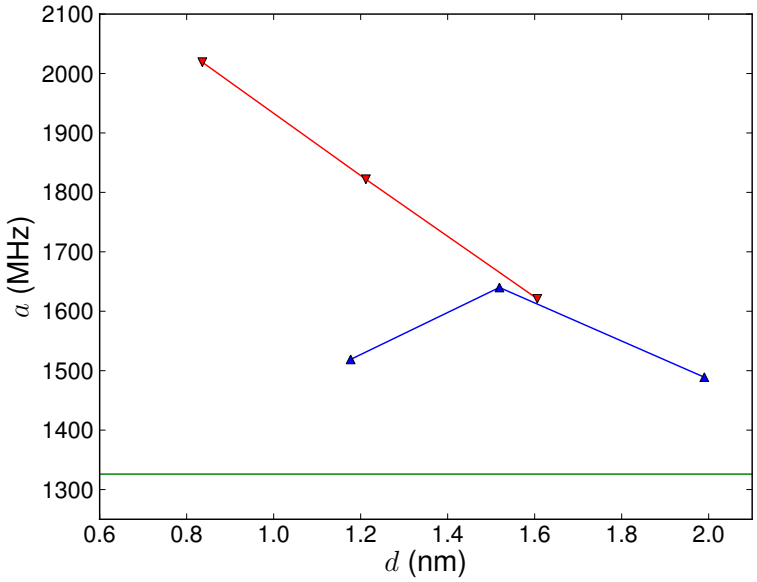

Figure 5.1: Hyperfine contact term a of Se defect on the axis of nanowires oriented along the [001] direction as a function of the diameter. The bulk value (green) is the one obtained from our calculations. For nanowires with surface reconstruction (blue) a has a maximum at 1.5 nm, while for nanowires without surface reconstruction (red) a monotonically increases with decreasing diameter.

defect, and we can thus use it to obtain reliable values in silicon nanowires. In fact, in confined systems the interaction between the replicas is further suppressed and we expect our technique can yield sensible results even for donors that are shallow in bulk crystals. In the following we will consider as a term of reference the calculated value of a in bulk silicon and not the experimental one.

5.3 Confinement effect

We now examine how the change from a bulk structure to a nanowire influences the values of the hyperfine parameters. The basic idea is that, due to the lateral confinement, the wavefunction of the defect, and thus the spin density, is pushed towards the defect, leading to an increase of the hyperfine contact term. We will show that this is true only under certain conditions.

Since here we are interested only in the dependence of the hyperfine parameters on the structural properties of the nanowire, we will consider only defect placed on its axis, in order to reduce the effects of the interaction with the surface and to highlight those of confinement.

First, we investigate the dependence of the hyperfine structure on the nanowire diameter and on the surface reconstruction. In doing that, we limit ourselves just to the case of Se donor and nanowires oriented along the [001] directions, since these are the configuration that we have analysed more extensively. In Figure 5.1 we have reported the change in the contact term as a function of the diameter for

nanowires both with and without surface reconstruction. As a consequence of the squeezing of the defect level wavefunction, a is always higher in nanowires than in bulk Si and its value tends to increase as the diameter is reduced. However, while nanowires without the initial surface reconstruction respect this trend, for nanowire with surface reconstruction the value of a at diameter of about 1.2 nm is lower than that at 1.5 nm. Comparing the values of a for nanowires with same diameter but different surface structure (i.e. NW1 and NW5) we can deduce that surface relaxation is responsible for the small value in NW1. This is evident also from the deformation of the donor wavefunction due to the alteration of the symmetry of the surface, that reduces the s-like character of the spin density. Thus, we can conclude that, even for a deep donor as Se, the effects of surface cannot be neglected in the determination of the hyperfine structure for nanowires with diameter comparable or smaller than 1 nm. Apart from this case, the contact term follows an almost linear relationship between a and the diameter, in the range we have covered. Noting that at a diameter of 2 nm the difference between the contact term in the bulk and in the nanowire is only about 10%, we do not expect to have sizeable differences at diameters above a few nanometers.

These properties of chalcogen in silicon nanowires are important since demonstrate that, if one is interested in obtaining a high hyperfine contact term, there is only a small range of diameters for which it is possible to obtain a non-negligible increase of a before the influence of surface deformation starts to counter the effect of confinement. Comparing our results with those calculated by tight-binding approach in chalcogen doped silicon nanocrystals [123], we see that reaching a convergence to the bulk value at small diameters is a common feature for chalcogens in nanostructures. In contrast, it has been observed that when considering phosphorus doped silicon nanowires [124] and nanocrystals [125–127] the percentage increase of the contact term is much higher at the same diameters and the convergence is reached for diameter greater than 10 nm [126]. This can be easily understood noticing that Bohr radius of phosphorus is much larger than that of chalcogens in bulk silicon. However, from the numerical comparison of our values with that from Rurali et al. [124] we note that, for similar diameters, a is always greater for Se than P doped nanowires.

In Table 5.2 we display our results of the calculations of parameters a, b and b' defined in equation (5.7) for all the nanowires here considered. In this case, since we are dealing with Se on the axis of nanowires oriented along the z direction, the values $\mathbf{A}^{iz}_{\mathrm{dip}}$ $(i = x, y)$ are zero or negligible, so we set $2b = \mathbf{A}^{zz}_{\mathrm{dip}}$ and $b' = \left|\mathbf{A}^{xx}_{\mathrm{dip}} - \mathbf{A}^{yy}_{\mathrm{dip}}\right|$ after tensor diagonalization. We point out that, at variance with [001] oriented nanowires, where the dipolar tensor has two eigenvectors with components $(1/\sqrt{2},1/\sqrt{2},0)$ and $(1/\sqrt{2},\text{-}1/\sqrt{2},0)$, for [011] and [111] oriented nanowires $\mathbf{A}_{\mathrm{dip}}$ is almost diagonal in the supercell orthonormal base, except for negligible off-diagonal terms, that are at least two order of magnitude smaller than the diagonal ones.

If we focus again on [001] oriented nanowires, we can see that the values of b and b' are quite small (less than 1 MHz) except for the case of NW1, where the stronger anisotropic interaction highlights one more time the effects of surface relaxations for nanowires of this size. Notably, the values of b have a different sign depending on the surface structure: positive in presence of surface reconstruction and negative for

	d (nm)	S			Se		
		a	b	b'	a	b	b'
[001]							
NW1*	1.18				1519	6.34	18.34
NW2†	1.52	374	0.29	0.007	1640	0.77	0.21
NW3	1.99				1489	0.44	0.01
NW4$^\parallel$	0.84	454	-0.23	0.03	2019	-0.46	0.15
NW5*	1.21				1822	-0.42	0.09
NW6†	1.61				1621	-0.63	0.03
[011]							
NW9†	1.51	312	-2.35	0.35	1467	-7.67	1.05
[111]							
NW10$^\parallel$	0.83	207	1.70	0.001	2032	0.55	0.03
NW11†	1.67	325	-0.75	0	1574	-1.69	0.005
bulk		314	0	0	1326	0	0

Table 5.2: Hyperfine contact term a, and the two dipolar interaction parameters b and b' with S and Se defect on the axis of the nanowire. The calculations with S donor have been performed only for some selected nanowires. Nanowires marked with the same symbol ($*$, $\dagger$ or $\parallel$) denotes nanowires with similar diameters. The hyperfine parameters are expressed in MHz.

nanowire passivated from the beginning. This can be due to the small differences in the local structure near the defect caused by the different surface structure and to the differences in the length of the relaxed supercells.

Since b' is a measure of the nonaxial symmetry of the donor wavefunction, its values for surface reconstructed nanowires are considerably larger than those of nanowires with similar diameter but without surface reconstruction.

Let us now look at the dependence on the orientation of the nanowires doped with selenium. Comparing the values for [001] and [111] orientations we can see that there is no relevant difference in the values of the contact term. The agreement is very good when the nanowires have the same diameter, while the small difference between NW11 and NW6 was already expected, due to the slightly larger diameter of the former. The dipolar terms differs significantly, since each orientation lead to a completely different local structure with respect to the axis of the nanowire. However, they have the same order of magnitude of their corresponding values for [001] nanowires and in particular, since they have no surface reconstruction, the asymmetry term b' is small.

The nanowire with [011] orientation is a special case. We observe that, as expected, the nanowire NW9 shows an anomalous behaviour both for contact and dipolar term, compared to nanowires with other orientations but similar diameters. Recalling the discussion of Section 4.1, it is possible to conclude that the spread of the donor wavefunction along the nanowire axis reduces its s-like component

	defect position 1	defect position 2	defect position 3	defect position 4
a(MHz)	1641	1548	856	928

Table 5.3: Hyperfine contact term a for NW2 with Se defect in different positions (see Figure 4.4). The values can be divided in two groups, one with Se being in the core and the other with Se in the surface region.

and this leads to a decrease in the hyperfine contact term. By contrast, for the same reason, b and b' are an order of magnitude greater than in NW6 and NW11. It should be noted however that, differently from NW1, b' is still much smaller than b, since the cylindrical symmetry of the system is still preserved. Given the proximity of the defect to the surface in NW8, which can act as a further element of disturbance, we have chosen not to calculate its hyperfine structure.

Given these results, at the moment we don't know if the particularity of [011] nanowires is a feature of the nanowire orientation itself or of the structure of the system that we have used for our simulations, so we can't draw a final conclusion about the dependence of the hyperfine parameters on the orientation.

Replacing the selenium defect with sulphur does not alter the overall behaviour of the hyperfine parameters. We have an increase of the contact term as the diameter is reduced, even if this is smaller in percentage terms compared to selenium doped nanowires. The same holds true for the dipolar terms. There are however two remarkable exceptions in the cases of nanowires NW9 and NW10. For NW9 a has a value that is little smaller than our result calculated in the bulk. This can be ascribed to a greater interaction between the defect replicas for S doped nanowires. The case of NW10 is different, since during the relaxation the sulphur atoms shifts away from one of its nearest neighbours. This leads to a deformation of the spin density that causes a strong decrease of the contact term and an increase of the anisotropic term b. This phenomenon is the same that we have observed when the Se doped nanowire NW10 has been subject to a strong tensile strain (see Subsection 5.5.2). In fact, as a last point, we notice that the hyperfine parameters can depend strongly on compressive and tensile strain, even for a departure of less than 1% of the nanowire lattice constant from our relaxed value. We will deal with this problem in a separate section.

5.4 Defect position

Having established that at diameters greater than 1.5 nm the effects of surface relaxation for a defect on the axis of the nanowire are sufficiently small, we now move on to the analysis of the dependence of the hyperfine parameters on the position of the defect. The focus here is on the nanowire NW2, because it has the maximum a among the relaxed nanowires with Se at the central site. The results for a are summarized in Table 5.3. It is evident from these values that, for defects located near the axis of the nanowire, the contact terms are quite similar among them and greater than in the bulk. Conversely, near the surface of the nanowire, the deformations lead to a steep decrease of a, bringing it well below the bulk value.

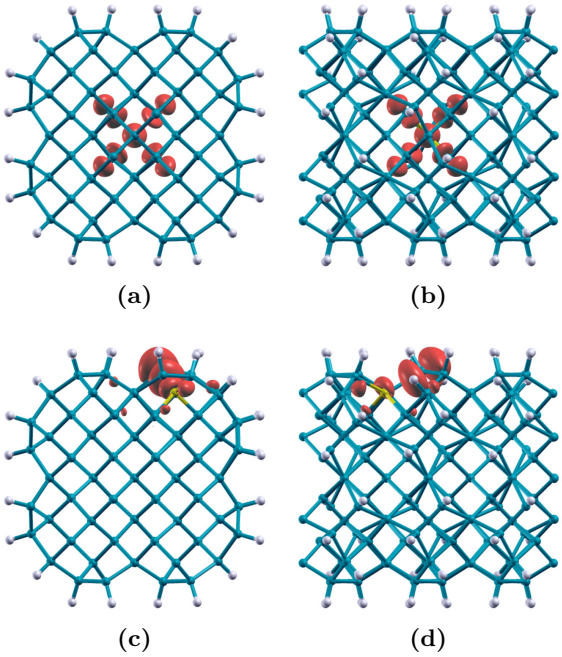

Figure 5.2: Section (a,c) and side (b,d) view of the defect wavefunction modulus in NW2. With the defect in position 1 (top), the four lobes of the wavefunction point towards the four tetrahedral directions. This structure is quite similar to that obtained in bulk as well as in other nanowires with defect in central positions. This symmetric structure is lost for defects located near the surface, as in position 3 (bottom). In this case the wavefunction is mainly localized near the external Si atom. The isosurface of the two wavefunctions have been evaluated at approximately the same isovalue.

This should be due to the interaction with the surface and to the possible formation of complexes with H atoms. In the case of a subsurface position the contact term of the superhyperfine interaction gives some insight about this possibility: the contact term of the superficial silicon atom close to the Se is greater than that of the other impurity nearest neighbours and also the superficial H atom has non-negligible a compared to other passivating atoms. This supports the previous hypothesis of a wavefunction delocalized over the Se-Si-H atoms.

In Figure 5.2 it is evident the difference between the wavefunction of the defect in the two distinct positions: when the defect is at the center the defect wavefunction has the same symmetry as in bulk crystal, whereas when the defect is close to the surface this symmetry is lost.

Given these different properties of the hyperfine contact term for the defect near the axis of the nanowire with respect to the defect close to the surface, we suggest that this could be a way to determine the distribution of the dopants inside the silicon nanowire using EPR measurements. This is important since, as we have seen in Chapter 1, no definitive answer has been found to the question about the segregation at the surface of the defects, these results can provide an additional tool to approach this problem from an experimental point of view.

For defects located off the axis of the nanowire, the tensor $\mathbf{A}_{\text{dip}}$ is not oriented along the z axis, the parameters b and b' are about one order of magnitude bigger

than the values reported in Table 5.2 and strongly dependent on the defect position. In practice, even considering two substitutional positions at small distance between each other, the dipolar tensors can have different magnitude and orientation. This is a further confirmation of the changes in the hyperfine structure between different regions of the nanowire, but, contrary to the Fermi contact term, it seems hard that the dipolar term can be used to localize the position of the defect, due to large fluctuations of the components of the $\mathbf{A}_{\mathrm{dip}}$ tensor.

5.5 Strain

The effect of the compressive and tensile strain on silicon nanowires has been already investigated with *ab-initio* simulations, but in these works the main attention has been devoted to the study of mechanical properties [128] and of the band structure [129] of pristine nanowires, verifying a dependence of the calculated quantities on the growth orientation.

Here we want to verify the effect of the strain on the hyperfine parameters in our doped nanowires. Restricting to bulk silicon this has already been demonstrated experimentally for phosphorus donors, inducing a strain on the sample with different techniques: applying a mechanical pressure [130], growing the crystal on a $\mathrm{Si_{1-x}Ge_x}$ substrate at various concentrations [131] or using a piezoelectric actuator [132]. It is possible that similar methods can be use to strain also nanostrucures.

Given the computational effort required to calculate the hyperfine parameters in each strained configuration, we have limited ourselves to the study of the smaller nanowires. This forces us to the use of nanowires passivated without previous surface reconstruction, in order to suppress the dependence of our calculations on the interaction with the surface as much as possible.

In our simulations the strain has been applied to the nanowires changing the length of the supercell L_z and letting the positions of the atoms relax again. As a term of comparison, we have also performed the same simulations on selenium doped bulk silicon. In this case we have changed uniformly the size of the supercell in x and y directions and then let the length of the supercell along z relax until the reaching of its equilibrium value.

We have already verified that, with the supercell size we have used, also the hyperfine parameters are strongly influenced by the interaction between the defect and its replicas in the case of [011] oriented nanowires, this orientation has thus not been considered for this analysis. The other two orientations, [001] and [111], behave differently under the application of strain, so they will be treated separately.

5.5.1 [001] orientation

In Figure 5.3 we report our results for changes of the hyperfine parameters a, b and b' as a function of the percentage variation of the supercell length L_z. This has been done for both NW4 and NW5 with the selenium defect at the central position, while for NW4 a position as close as possible to the axis has also been considered. These results are compared with the same quantities for bulk silicon.

For this orientation, the modification of L_z alters the tetrahedral symmetry of the nearest neighbours of the defect uniformly. More precisely, in an unstrained bulk

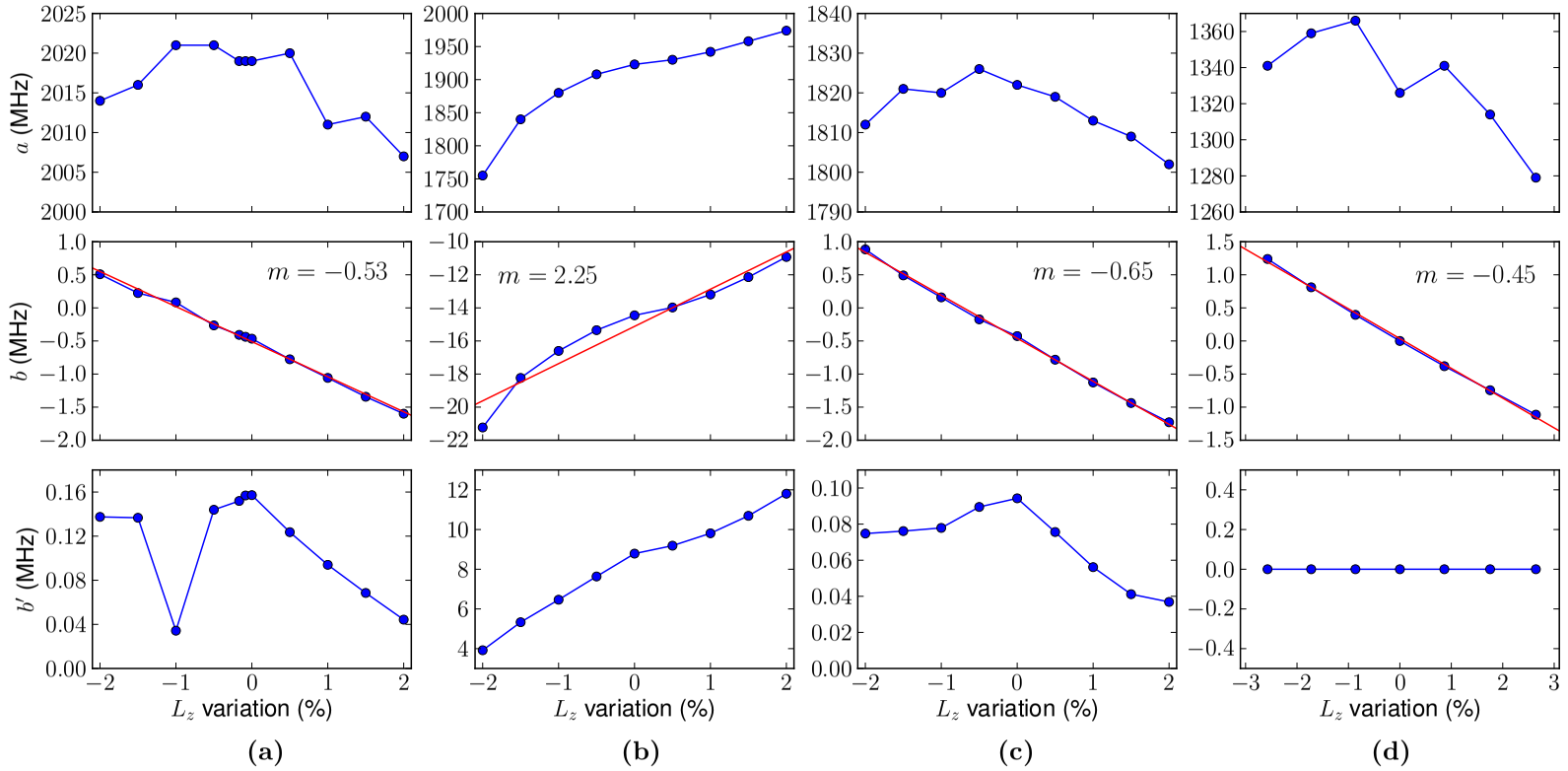

Figure 5.3: The effect of compressive and tensile strain on the hyperfine parameters a, b and b' for (a) NW4 with Se defect at the center, (b) NW4 with the Se defect next to the axis of the nanowire, (c) NW5 with Se defect at the center and (d) bulk silicon. The red lines with slope m are the linear interpolations of the dipolar term b.

crystal, in polar coordinates the position of every nearest neighbour is described by the angle θ with the z axis that satisfies the relation $\cos\theta = 1/\sqrt{3}$. The main effect of the application of a strain is to increase or reduce the angle θ for compressive and tensile strain, respectively. The effect is similar in a [001] nanowire and leads to an almost linear decrease of the nanowire diameter as L_z is increased.

Limiting to the case of the donor on the axis of the nanowire (Figures 5.3a and 5.3c), we can observe some interesting features which are shared with the bulk silicon. The first is that the hyperfine contact term a is not strongly affected by the changes in the size of the supercell. The variations are in the order of about 4% for bulk silicon, while they are reduced to 1.6% and 0.75% for NW5 and NW4, respectively. This is consistent with the fact that the local symmetry is not altered significantly. In light of this, our conclusions of the previous sections about the contact term should not be influenced by small departures from the equilibrium value of the supercell size.

The second observation regards the linear relation between the uniaxiality term b and the L_z variation. This is important since, as can be seen in Figure 5.3, a variation of less than 1% in the supercell length can induce a shift of b of the order of more than 100% and even a change of its sign. The main consequence for our work is that our numerical results for b in unstrained conditions can be affected by higher imprecision compared to that of a if the relaxed supercell size is not achieved with high precision. It is possible to note that, keeping the attention on the case of defects on the axis of the nanowire, the slope of the interpolating line is negative and this might at first sight seem somewhat unexpected. To give a more detailed explanation let us consider the explicit expression for b. From equation (5.6) we see that b, in our convention, can be written as

$$b = \frac{\mathbf{A}^{zz}_{\mathrm{dip}}}{2} = \frac{g_{\mathrm{e}}\mu_{\mathrm{e}}g_{\mathrm{N}}\mu_{\mathrm{N}}}{4\langle S_z\rangle}\int \mathrm{d}^3 r n_s(\mathbf{r})\frac{3\cos^2\tau - 1}{r^3}, \tag{5.10}$$

where τ is the angle between $\mathbf{r}$ and the z axis. This expression changes sign for τ such that $\cos\tau = 1/\sqrt{3}$ and the dipolar term is thus zero for bulk silicon due to the tetrahedral symmetry of the crystal. We have observed that when the nanowire is strained the defect wavefunction maintains the same structure, with the lobes pointing towards the four defect nearest neighbours. Since when the system is compressed the coordinate θ of the nearest neighbours is increased, one expects the wavefunction to rotate in agreement with them and to increase the value of $n_s(\mathbf{r})$ for the region of the integral where $3\cos^2\tau - 1 < 0$. The opposite should hold true for tensile strain and this would have lead to a positive slope, in contrast with our results. A deeper analysis of our data shows that this explanation is correct and that the problem lies in the displacement of the donor wavefunction and thus of the spin density $n_s(\mathbf{r})$. In fact, the spin density contributes relevantly to the integral in equation (5.10) only for small values of the radius r and we have verified that close to the nucleus the spin density is deformed in such a way that it is mostly distributed in the direction opposite to that of movement of the nearest neighbours. This is exemplified schematically in Figure 5.4 for the isosurface of the spin density under compressive and tensile strain.

The slope of b as a function of the strain shows however another anomaly. We would have expected that increasing the diameter the value of the slope m would

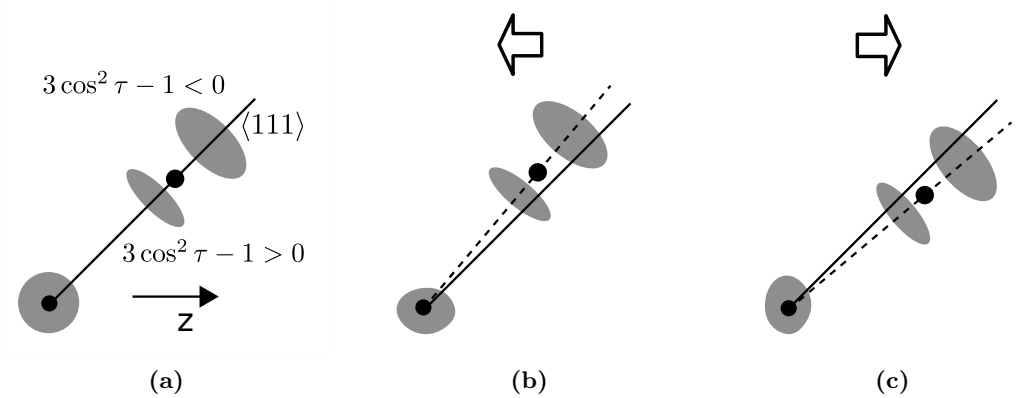

Figure 5.4: Schematic description of the effect of strain on the electron spin density $n_s(\mathbf{r})$ in the proximity of the defect and one of his nearest neighbours. The gray shaded area represents an isosurface of the spin density along the $\langle 111 \rangle$ for (a) unstrained, (b) compressed and (c) tensed system. The deformation of the spin density close to the defect explains the trend of b. The z direction indicates the orientation of the nanowire. Note that this is an oversimplified picture of the phenomenon and the real deformation is only roughly approximated.

have converged to the bulk result, but the slope decreases from -0.53 for NW4 to -0.65 for NW5, while the bulk value is greater (-0.45). This should be probably ascribed again to the small diameters of the nanowires, that can perturb the result.

Lastly, we can note that, while in bulk crystal the asymmetry term b' is exactly zero, in nanowires it is strongly affected by the strain. No specific trend has been recognized in this case, except from the fact that b' reaches its maximum value for the unstrained system. Its values are however small and remain quite stable in a neighbourhood of the unstrained configuration.

The results for nanowire NW4 with the defect next to the axis of the nanowire (Figure 5.3b) are entirely different from those with the defect on the axis. The contact term changes more than 10% over our range, the dipolar term b has a high positive slope, even though it keeps an almost linear behaviour, and b' has big values and a linear trend. This outcome is the result of the interaction of the defect wavefunction with the surface, since, given the small sizes of NW4, even the one next to the axis should be considered a subsurface position. At this level the data can be used as a further confirmation of the linear dependence of b on the strain of the system.

5.5.2 [111] orientation

Nanowires oriented along the [111] direction behaves differently compared to what described above, due to the orientation of the bonds with respect to the direction on which the strain is applied. In fact, while for [001] nanowires the system is symmetric about the xy-plane passing through the defect, in [111] oriented nanowires the bond between the defect and one of his nearest neighbours is directed along the axis of the nanowires and the other three bonds form an angle of about 109° with the z axis (the tetrahedral angle). In this way the strain acts

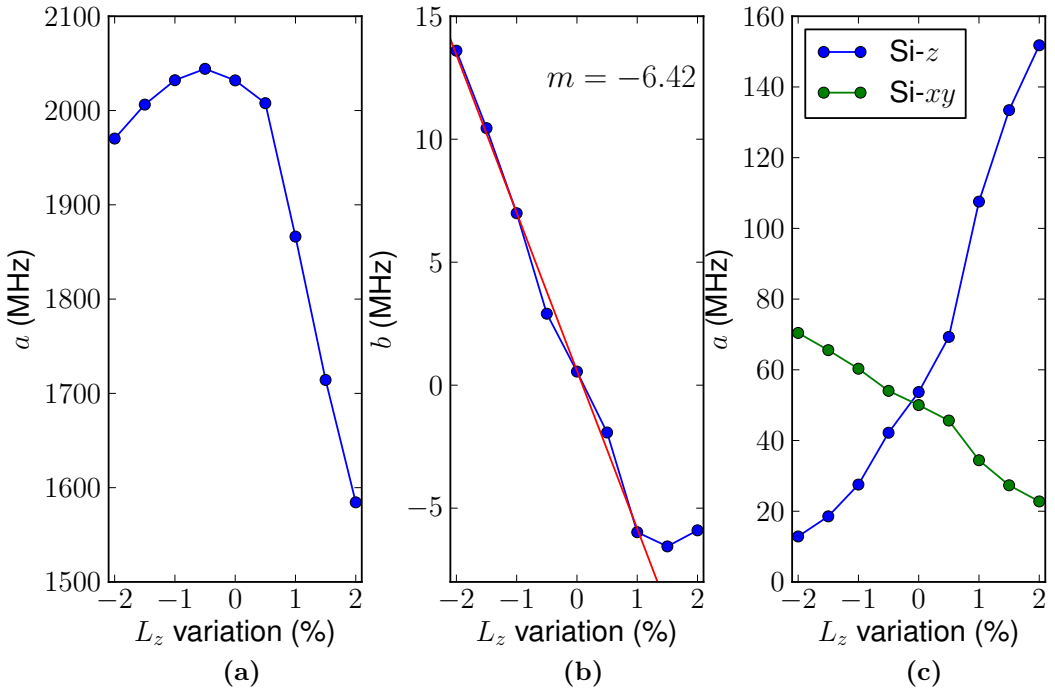

Figure 5.5: Hyperfine parameter (a) a and (b) b of the defect and (c) superhyperfine parameter a for the Se defect nearest neighbours Si-z and Si-xy as a function of the length of the supercell L_z of the nanowire NW4. In (b) the interpolation (red line) has been calculated considering only the data from -2% to +1%, since at higher values of the strain linear trend is lost.

non-uniformly on the bonds, inducing an asymmetry of the donor wavefunction. From now on we will refer to these two groups of silicon atoms as Si-z and Si-xy, respectively, with the notation referring to the orientation of the bonds with respect to the orthonormal basis of the real space given by the axes x, y, z.

In Figure 5.5 the results for the defect contact term a and dipolar term b are shown, along with the superhyperfine contact term for both Si-z and Si-xy in nanowire NW10. We do not report the data for b' since in this case its value is always smaller than 0.035 MHz, which can be considered negligible. For the hyperfine terms a and b we can distinguish two different regimes, depending on the strain of the system. When the length of the supercell L_z is varied from -2% to +0.5% the behaviour is similar to that of [001] nanowires. In this range, a changes of only 3% between its maximum and minimum values and b has a linear dependence on the strain with a negative slope, although in this case it is much more steeper compared to [001] oriented nanowires. For tensile strain above 1%, instead, the contact term starts to drop abruptly, with a linear decrease, while the dipolar term b remains almost constant. We should point out that, even with its small values, these two different ranges can be recognized also in the values of the term b'.

The discontinuity in the hyperfine parameters of the defect which takes place for tensile strain can be understood by the analysis of superhyperfine data for Si-z and Si-xy. Looking at Figure 5.5c we can see that the contact term is uniform on all

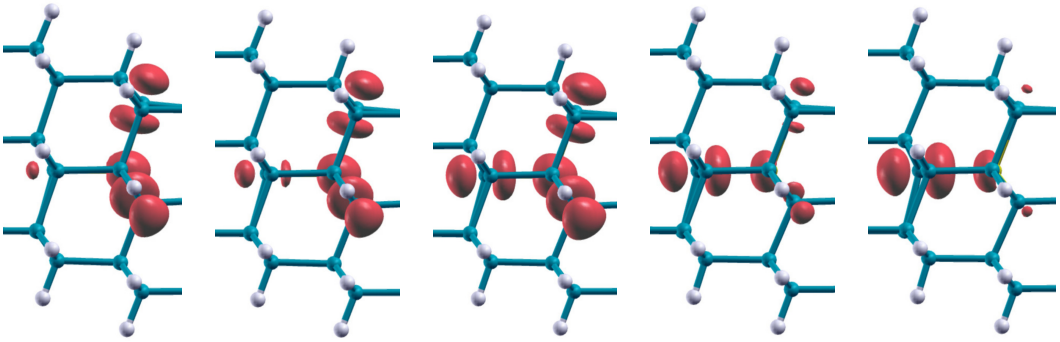

Figure 5.6: Isosurface of the defect wavefunction for various elongations and contractions of the supercell along the axis of the nanowire. The supercell length L_z is varied by (a) -2%, (b) -1%, (c) 0%, (d) +1% and (e) +2% from the relaxed value. The wavefunction shifts from the Si-xy atoms to the Si-z atoms as L_z is increased.

the defect nearest neighbours only for the relaxed supercell size and the value of a at which the two lines cross is the same that we have obtained for [001] nanowires. In fact, at variance with the case of [001] nanowires, where the superhyperfine contact terms remain constant all over the range explored, here we have a linear dependence on L_z. We can see from Figure 5.6 that this is simply explained by the defect wavefunction distribution. When the nanowire is compressed the atom Si-z gets closer to the selenium defect and the wavefunction shifts towards the Si-xy atoms (Figures 5.6a and 5.6b). The opposite happens when the system is subject to tensile strain (Figures 5.6d and 5.6e). From our superhyperfine data in Figure 5.5c one can deduce that this transformation is uniform. However, since there is only one Si-z against three Si-xy atoms, when the wavefunction moves towards the Si-z atom an asymmetry is induced on the system and, in particular, we can see that the wavefunction close to the nucleus is strongly deformed along the z axis. In practice, when the nanowire is tensed over a certain limit we have a breakdown of the symmetry of the defect wavefunction, that loses most of its s-like character, and this causes the anomalous behaviour observed for the hyperfine parameters.

The same mechanism explains the negative slope of the uniaxiality b considering the expression (5.10). Again, one should not be misled by the distribution of the defect wavefunction far from the nucleus. The relevant part of the integral in equation (5.10) is for small values of the distance from the defect r and, like for [001] oriented nanowires, the deformation of the spin density in the proximity of the nucleus takes place in such a way that $n_s(\mathbf{r})$ has a relevant distribution in the region where $3\cos^2\tau - 1 > 0$ for compressive strain and vice versa for tensile strain.

Conclusions

In this thesis we have studied by *ab-initio* calculations the properties of pristine and chalcogen doped silicon nanowires. The analysis on non-doped systems has been useful in order to prepare a set of nanowires, whose properties are consistent with other theoretical and experimental results present in literature about the effect of quantum confinement. In addition, it has permitted to study the differences in the band structure between nanowires that have undergone an initial surface reconstruction before hydrogen passivation and nanowires with the same number of silicon atoms but obtained passivating the structure as it is cut from the bulk crystal. We have verified that the surface reconstruction induces a stronger displacement of the atoms at the surface and that in the band structure, along with a small reduction of the band gap, this can induce a direct to indirect band gap transition with respect to the nanowires passivated from the beginning.

Concerning the doped nanowires, we have performed the most of our simulations focusing on selenium double donor and used the sulphur as a term of comparison in some selected cases. From our simulations we have obtained the formation energies of the defect in various positions and charge states for nanowires of different dimensions and orientations. The results do not always show the increase in the formation energy when the diameter of the nanowire is reduced that it would be expected from the effect of quantum confinement. This is due to the deformations caused by the surface reconstruction or by the direct interaction with the surface and the passivating hydrogen atoms. In fact, one of the features that we have observed is that, when the selenium defect is in the subsurface position, during the relaxation process drifts away from the couple Si-H at the surface and comes close to the other three nearest neighbours. We have associated this behaviour with the formation of a complex chalcogen-hydrogen defect, whose existence in bulk silicon has been proved both theoretically and experimentally. Another consequence of this deformation at the surface is the reduced formation energy for subsurface and surface positions compared to the center of the nanowire. Although the differences between the two regions are relatively small, we can conclude that selenium defects in silicon nanowires have a tendency to surface segregation as has been observed for other kind of donors, like phosphorus and boron.

The dependence on the orientation of the nanowires is interesting because, while we do not have big differences between [001] and [111] oriented nanowires with approximately the same diameters, the situation is different for the [011] orientation. In this case we have verified that, even bringing the length of the supercell along the axis of the nanowire to 2 nm, the interaction between the defect and its fictitious replicas cannot be neglected, whereas smaller dimensions where sufficient for the

other orientations. Since further increasing the dimension of the supercell would have brought above our computational limit, we could not distinguish if the anomaly of the [011] oriented nanowires should be ascribed to its peculiarities or simply to the size of the supercell. Nonetheless, the dependence of the minimum length of the supercell and the interaction between dopants on the orientation defines an interesting problem on its own and further analysis will be devoted to this topic in a separate work.

The most relevant and original part of our work is the one about the calculation of hyperfine structure. First of all we have checked that the PAW method can be successfully used to obtain hyperfine parameters in good agreement with experimental data for donors in silicon, provided that the defect is deep enough to prevent too strong interactions between the replicas of the defect. This has allowed us to calculate the hyperfine parameters to a good degree of approximation also for chalcogen in silicon nanowires. Our results demonstrates that when considering dopants in the core of the nanowire the effect of quantum confinement is to squeeze the donor wavefunction leading to an increase of the hyperfine contact term a when the diameter of the nanowire is reduced. However, we have observed that when the diameter is decreased below 1.2 nm the effects of surface reconstruction lead to a partial breaking of the symmetry of the defect wavefunction, with a consequent reduction of the contact term. Moreover, despite the high increase observed for small nanowires, a seems to converge quickly to the bulk value as the diameter is increased.

The following step was to test if the increase of the contact term is independent of the position of the defect inside the nanowire. Our data clearly indicates that this is not the case and for subsurface and surface defect positions a drops to a value below the one of the bulk silicon, showing that the interaction with the surface is much more crucial than the effect of quantum confinement.

Lastly, we have studied the dependence of the hyperfine parameters on compressive and tensile strain along the axis of the nanowire. We have thus observed that, while a is quite stable, b undergoes a linear change with a negative slope as the length of the supercell is varied. This allows to deduce that the calculations on the contact term are not affected by possible small imprecision in the relaxed supercell size.

All these results are of key importance in light of possible applications based on the value of the hyperfine parameters. They demonstrates that if a large value of the hyperfine contact term is needed, like for example in the realization of a nuclear spin qubit, a high control of the dimensions of the nanowire and of the position of the defect is required. The diameter should be in the small range for which the contact term can benefit from the confinement effect without being perturbed by the interaction with the surface and the donor should be implanted in the core of the nanowire. On the other hand, the steep decrease between the core and surface regions provides a useful method to localize the disposition of the donors inside the nanowire by EPR measurements, a problem which is of great interest based on the relevance of doping for semiconductor technology.

Appendix A

Formation energy in silicon nanowires

In our calculations and in DFT simulations in general the ability to calculate correctly the formation energy of a defect in its different charge states is of paramount importance, since it allows to determine the most favourable states and spatial configurations for the defect under examination. Usually, the formation energy is calculated in the Zhang-Northrup formalism and some correction schemes have been devised to confront the problem of fictitious interactions in the case of charged defects. However, these procedures are defined in bulk crystals, while we are dealing with nanowires, that are not bulk-like systems. Some changes are thus required if one wants to obtain more accurate results in the calculation of the formation energy. In this appendix we introduce the adaptations proposed by Rurali and Cartoixà [72] to be applied in the specific case of nanowires, both to the correction for charged defects and to the expression of the formation energy.

A.1 Charged defects

In general, studying defective systems in periodic boundary conditions is problematic due to the fictitious interactions that arise from the defect and its periodic images. One of the possibilities to overcome this difficulty is to enlarge the supercell until the interactions can be considered negligible, but this can be impossible in some systems due to the limitation of computational capabilities. Charged defects are even more difficult to deal with since, due to electrostatic interaction, the total energy of the system would be divergent. Conventional algorithms insert a compensating jellium background to make the supercell neutral and cancel the divergence, as is done in Quantum ESPRESSO. A standard way to speed up the convergence with respect to the supercell size is to add a correction to the total energy of the system derived by Leslie and Gillan [133] depending on the inverse of the linear supercell dimension $L = \Omega^{-1/3}$ (where Ω is the supercell volume) and generalized by Makov and Payne [71] with an additional higher-order correction term depending on L^{-3}. The correction is given by

$$E(L) = E_0 - \frac{q^2\alpha}{2\varepsilon L} - \frac{2\pi qQ}{3\varepsilon L^3} + O[L^{-5}], \tag{A.1}$$

nanowire	ε_{xx}	ε_{yy}	ε_{zz}
NW1	2.013	2.013	4.377
NW2	1.764	1.764	3.949
NW3	1.969	1.969	4.746

Table A.1: Dielectric tensor for various pristine nanowires, calculated as a linear response to an external electric field. The tensor is diagonal and for symmetry reasons the values along x and y directions are equal.

where q is the charge of the defect, Q is the second radial moment of the extended charge density, α is the appropriate superlattice Madelung constant and ε is the static dielectric constant of the host material.

In a nanowire the value of the Madelung constant depends on the relation between the lattice parameter and the dielectric tensor $\bar{\varepsilon}$ of the system, so this procedure cannot be applied straightforwardly. The expression for the Madelung constant in the general case has been calculated by Rurali and Cartoixà [72] and is given by

$$\begin{aligned}\alpha = &\sum_{\mathbf{R}_i} \frac{1}{\sqrt{\det \bar{\varepsilon}}} \frac{\operatorname{erfc}\left(\gamma\sqrt{\mathbf{R}_i \cdot \bar{\varepsilon}^{-1} \cdot \mathbf{R}_i}\right)}{\sqrt{\mathbf{R}_i \cdot \bar{\varepsilon}^{-1} \cdot \mathbf{R}_i}} + \\ &\sum_{\mathbf{G}_i} \frac{4\pi}{\Omega} \frac{\exp\left(\mathbf{G}_i \cdot \bar{\varepsilon} \cdot \mathbf{G}_i / 4\gamma^2\right)}{\mathbf{G}_i \cdot \bar{\varepsilon} \cdot \mathbf{G}_i} - \frac{2\gamma}{\sqrt{\pi \det \bar{\varepsilon}}} - \frac{\pi}{\Omega\gamma^2},\end{aligned} \tag{A.2}$$

where the sums over $\mathbf{R}_i$ and $\mathbf{G}_i$ extends over all the vectors of the direct and reciprocal space, respectively, and γ is a suitably chosen convergence factor.

This is the correction that we have applied to the total energy of the system when we had to consider charged systems, i.e. singly and doubly ionized selenium defect (see Section 4.3). In order to obtain the correction we had to calculate the dielectric tensor for our systems. This has been done for each nanowire in its pristine form as a linear response to an external electric field [85]. The values of the dielectric tensors that have been used in our corrections are reported in Table A.1.

A.2 Formation energy

The Zhang-Northrup formalism for the calculation of the formation energy [106] has been described in Section 4.3 and the general expression for the formation energy is given in equation (4.2). One of the components in the expression is the chemical potential μ of the reservoir for the various elements, but the value that should be used for this quantity when studying silicon nanowires is not obvious. In fact, when a defect is created in the crystals the original atoms that are removed from their location are considered to be placed in the crystal in its bulk phase. However, during the growth process that leads to the formation of the nanowire, the displaced atoms remain inside the nanowire and the value of μ should be chosen accordingly, resolving the ambiguity on the final position. Since it is not possible to consider a general correction, given all the inequivalent position, the solution proposed by Rurali and Cartoixà is based on a microscopic treatment of the system.

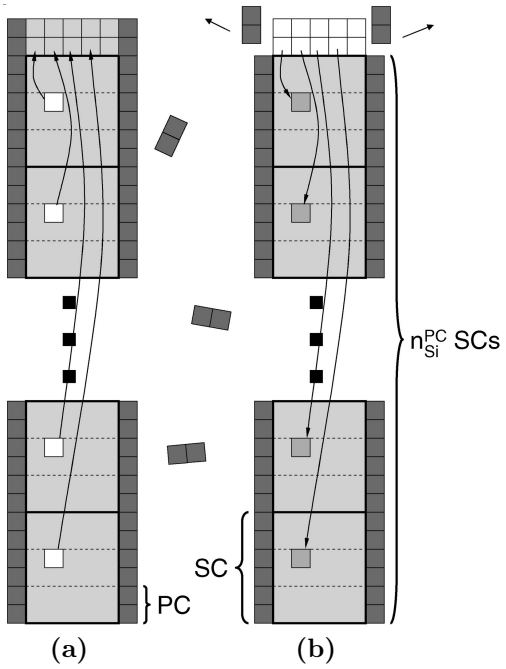

Figure A.1: Schematic approach for dealing with defect formation in nanowires. (a) For vacancies and substitutional defects an additional primitive cell (PC) is created from the silicon atom removed from each supercell. (b) For interstitial defects a primitive cell is removed and its atoms are used to for the defects in each supercell. Hydrogen atoms are taken or released as molecular hydrogen H_2. Adapted with permission from reference [72]. Copyright 2009 American Chemical Society.

The schematic approach of the solution is depicted in Figure A.1. The primitive cell (PC) is the unit cell of the pristine nanowire, containing $n_{\mathrm{Si}}^{\mathrm{PC}}$ silicon atoms and $n_{\mathrm{H}}^{\mathrm{PC}}$ hydrogen passivating atoms, while the supercell (SC) is made up of a multiple N of pristine cells and contains the defect. The basic idea is to consider $n_{\mathrm{Si}}^{\mathrm{PC}}$ copies of the supercell and thus $n_{\mathrm{Si}}^{\mathrm{PC}}$ defects, instead of a single one. Depending on the defect type, every silicon atom removed (added) from each of the $n_{\mathrm{Si}}^{\mathrm{PC}}$ supercells is used to create (eliminate) a further primitive cell, whose total energy is known. If one uses $n_{\mathrm{H}}^{\mathrm{PC}}$ times half of the energy of a hydrogen molecule as energy contribution of the passivating hydrogen atoms used (released) by the pristine cell, the formation energy of a single defect can be obtained by the expression

$$E_{\mathrm{f}} = E_{\mathrm{D}} - NE_{\mathrm{NW}}^{\mathrm{PC}} - \sum_i n_i\mu_i - \frac{n_{\mathrm{Si}}}{n_{\mathrm{Si}}^{\mathrm{PC}}}\left(E_{\mathrm{NW}}^{\mathrm{PC}} - n_{\mathrm{H}}^{\mathrm{PC}}\frac{E_{\mathrm{H_2}}}{2}\right) + q(\varepsilon_{\mathrm{V}} + \mu_{\mathrm{e}}). \qquad \text{(A.3)}$$

Here, the summation over i is limited to the atomic species added to the nanowire to form the defect that are different from silicon, while the number of silicon atoms involved in the formation is indicated by n_{Si}. $E_{\mathrm{NW}}^{\mathrm{PC}}$ is the energy of the primitive cell and $E_{\mathrm{H_2}}/2$ is the chemical potential of the passivating hydrogen atoms.

Note that this procedure is equivalent to define an average chemical potential of silicon in the nanowire and then apply the Zhang-Northrup formalism [134].

This corrected formula has been tested in our systems and in particular for

nanowire NW1, giving a difference of only 0.006 eV compared to the value of the formation energy calculated with the plain expression of equation (4.2). Since this can be considered negligible compared to the formation energies that we have observed, this correction has not been applied.

Bibliography

[1] A. Vellei, PhD thesis, Università degli Studi di Milano-Bicocca, Dottorato di ricerca in Nanostrutture e Nanotecnologie, 22, 2011-01-24.

[2] P. R. Bandaru, P Pichanusakorn, "An outline of the synthesis and properties of silicon nanowires", *Semicond. Sci. Technol.* **25**, 024003 (2010).

[3] V. Schmidt, J. V. Wittemann, S. Senz, U. Gösele, "Silicon Nanowires: A Review on Aspects of their Growth and their Electrical Properties", *Adv. Mater.* **21**, 2681–2702 (2009).

[4] D. D. D. Ma, C. S. Lee, F. C. K. Au, S. Y. Tong, S. T. Lee, "Small-Diameter Silicon Nanowire Surfaces", *Science* **299**, 1874–1877 (2003).

[5] Y. Wu *et al.*, "Controlled Growth and Structures of Molecular-Scale Silicon Nanowires", *Nano Lett.* **4**, 433–436 (2004).

[6] P. Yu, M. Cardona, *Fundamentals of Semiconductors: Physics and Materials Properties* (Springer, 2010).

[7] C. Delerue, M. Lannoo, *Nanostructures: theory and modeling* (Springer, 2004).

[8] C. Hamaguchi, *Basic Semiconductor Physics* (Springer, 2010).

[9] A. J. Read *et al.*, "First-principles calculations of the electronic properties of silicon quantum wires", *Phys. Rev. Lett.* **69**, 1232–1235 (1992).

[10] V. Schmidt, S. Senz, U. Gösele, "Diameter-Dependent Growth Direction of Epitaxial Silicon Nanowires", *Nano Lett.* **5**, 931–935 (2005).

[11] C. X. Wang, M. Hirano, H. Hosono, "Origin of Diameter-Dependent Growth Direction of Silicon Nanowires", *Nano Lett.* **6**, 1552–1555 (2006).

[12] J. D. Holmes, K. P. Johnston, R. C. Doty, B. A. Korgel, "Control of Thickness and Orientation of Solution-Grown Silicon Nanowires", *Science* **287**, 1471–1473 (2000).

[13] Y. Zhao, B. I. Yakobson, "What is the Ground-State Structure of the Thinnest Si Nanowires?", *Phys. Rev. Lett.* **91**, 035501 (2003).

[14] R Rurali, N Lorente, "On the properties of surface reconstructed silicon nanowires", *Nanotechnology* **16**, S250 (2005).

[15] J. F. Justo, R. D. Menezes, L. V. C. Assali, "Stability and plasticity of silicon nanowires: The role of wire perimeter", *Phys. Rev. B* **75**, 045303 (2007).

[16] R. Rurali, A. Poissier, N. Lorente, "Size effects in surface-reconstructed <100> and <110> silicon nanowires", *Phys. Rev. B* **74**, 165324 (2006).

[17] M.-F. Ng *et al.*, "Theoretical investigation of silicon nanowires: Methodology, geometry, surface modification, and electrical conductivity using a multiscale approach", *Phys. Rev. B* **76**, 155435 (2007).

[18] R. J. Bondi, S. Lee, G. S. Hwang, "First-Principles Study of the Structural, Electronic, and Optical Properties of Oxide-Sheathed Silicon Nanowires", *ACS Nano* **5**, 1713–1723 (2011).

[19] M. Koleini, L. Colombi Ciacchi, M. V. Fernández-Serra, "Electronic Transport in Natively Oxidized Silicon Nanowires", *ACS Nano* **5**, 2839–2846 (2011).

[20] A. Svizhenko, P. W. Leu, K. Cho, "Effect of growth orientation and surface roughness on electron transport in silicon nanowires", *Phys. Rev. B* **75**, 125417 (2007).

[21] A. Lherbier, M. P. Persson, Y.-M. Niquet, F. m. c. Triozon, S. Roche, "Quantum transport length scales in silicon-based semiconducting nanowires: Surface roughness effects", *Phys. Rev. B* **77**, 085301 (2008).

[22] M. P. Persson, A. Lherbier, Y.-M. Niquet, F. Triozon, S. Roche, "Orientational Dependence of Charge Transport in Disordered Silicon Nanowires", *Nano Lett.* **8**, 4146–4150 (2008).

[23] R. Rurali, T. Markussen, J. Suñé, M. Brandbyge, A.-P. Jauho, "Modeling Transport in Ultrathin Si Nanowires: Charged versus Neutral Impurities", *Nano Lett.* **8**, 2825–2828 (2008).

[24] M. P. Persson, H. Mera, Y.-M. Niquet, C. Delerue, M. Diarra, "Charged impurity scattering and mobility in gated silicon nanowires", *Phys. Rev. B* **82**, 115318 (2010).

[25] M. V. Fernandez-Serra, C. Adessi, X. Blase, "Conductance, Surface Traps, and Passivation in Doped Silicon Nanowires", *Nano Lett.* **6**, 2674–2678 (2006).

[26] J. Wang, J.-S. Wang, "Dimensional crossover of thermal conductance in nanowires", *Appl. Phys. Lett.* **90**, 241908 (2007).

[27] I. Ponomareva, D. Srivastava, M. Menon, "Thermal Conductivity in Thin Silicon Nanowires: Phonon Confinement Effect", *Nano Lett.* **7**, 1155–1159 (2007).

[28] D. Donadio, G. Galli, "Atomistic Simulations of Heat Transport in Silicon Nanowires", *Phys. Rev. Lett.* **102**, 195901 (2009).

[29] D. Donadio, G. Galli, "Temperature Dependence of the Thermal Conductivity of Thin Silicon Nanowires", *Nano Lett.* **10**, 847–851 (2010).

[30] R. Rurali, "*Colloquium*: Structural, electronic, and transport properties of silicon nanowires", *Rev. Mod. Phys.* **82**, 427–449 (2010).

[31] B. K. Teo, S.-P. Huang, R. Zhang, W.-K. Li, "Theoretical calculations of structures and properties of one-dimensional silicon-based nanomaterials: Particularities and peculiarities of silicon and silicon-containing nanowires and nanotubes", *Coord. Chem. Rev.* **253**, Functional Hybrid Nanomaterials: - Design, Synthesis, Structure, Properties and Applications, 2935 –2958 (2009).

[32] Y. Cui, Z. Zhong, D. Wang, W. U. Wang, C. M. Lieber, "High Performance Silicon Nanowire Field Effect Transistors", *Nano Lett.* **3**, 149–152 (2003).

[33] Y. Cui, C. M. Lieber, "Functional Nanoscale Electronic Devices Assembled Using Silicon Nanowire Building Blocks", *Science* **291**, 851–853 (2001).

[34] N. Singh *et al.*, "Si, SiGe Nanowire Devices by Top-Down Technology and Their Applications", *IEEE Trans. Electron Devices* **55**, 3107 –3118 (2008).

[35] Z. Zhong, Y. Fang, W. Lu, C. M. Lieber, "Coherent Single Charge Transport in Molecular-Scale Silicon Nanowires", *Nano Lett.* **5**, 1143–1146 (2005).

[36] M. Hofheinz *et al.*, "Simple and controlled single electron transistor based on doping modulation in silicon nanowires", *Appl. Phys. Lett.* **89**, 143504 (2006).

[37] M. Pierre *et al.*, "Compact silicon double and triple dots realized with only two gates", *Appl. Phys. Lett.* **95**, 242107 (2009).

[38] K.-Q. Peng, S.-T. Lee, "Silicon Nanowires for Photovoltaic Solar Energy Conversion", *Adv. Mater.* **23**, 198–215 (2011).

[39] B. Tian, T. J. Kempa, C. M. Lieber, "Single nanowire photovoltaics", *Chem. Soc. Rev.* **38**, 16–24 (2009).

[40] A. I. Hochbaum *et al.*, "Enhanced thermoelectric performance of rough silicon nanowires", *Nature* **451**, 163–167 (2008).

[41] A. I. Boukai *et al.*, "Silicon nanowires as efficient thermoelectric materials", *Nature* **451**, 168–171 (2008).

[42] F. Patolsky, C. M. Lieber, "Nanowire nanosensors", *Mater. Today* **8**, 20 –28 (2005).

[43] W. Kim, J. K. Ng, M. E. Kunitake, B. R. Conklin, P. Yang, "Interfacing Silicon Nanowires with Mammalian Cells", *J. Am. Chem. Soc.* **129**, 7228–7229 (2007).

[44] A. K. Shalek *et al.*, "Vertical silicon nanowires as a universal platform for delivering biomolecules into living cells", *Proc. Natl. Acad. Sci.* **107**, 1870–1875 (2010).

[45] B. Tian *et al.*, "Three-Dimensional, Flexible Nanoscale Field-Effect Transistors as Localized Bioprobes", *Science* **329**, 830–834 (2010).

[46] F. Patolsky *et al.*, "Detection, Stimulation, and Inhibition of Neuronal Signals with High-Density Nanowire Transistor Arrays", *Science* **313**, 1100–1104 (2006).

[47] R. Yan, D. Gargas, P. Yang, "Nanowire photonics", *Nat. Photon.* **3**, 569–576 (2009).

[48] J. R. Chelikowsky, M. M. G. Alemany, T.-L. Chan, G. M. Dalpian, "Computational studies of doped nanostructures", *Rep. Prog. Phys.* **74**, 046501 (2011).

[49] G. M. Dalpian, J. R. Chelikowsky, "Self-Purification in Semiconductor Nanocrystals", *Phys. Rev. Lett.* **96**, 226802 (2006).

[50] D. J. Norris, A. L. Efros, S. C. Erwin, "Doped Nanocrystals", *Science* **319**, 1776–1779 (2008).

[51] C. R. Leao, A. Fazzio, A. J. R. da Silva, "Confinement and Surface Effects in B and P Doping of Silicon Nanowires", *Nano Lett.* **8**, 1866–1871 (2008).

[52] H. Peelaers, B. Partoens, F. M. Peeters, "Formation and Segregation Energies of B and P Doped and BP Codoped Silicon Nanowires", *Nano Lett.* **6**, 2781–2784 (2006).

[53] M. V. Fernández-Serra, C. Adessi, X. Blase, "Surface Segregation and Backscattering in Doped Silicon Nanowires", *Phys. Rev. Lett.* **96**, 166805 (2006).

[54] M. T. Bjork, H. Schmid, J. Knoch, H. Riel, W. Riess, "Donor deactivation in silicon nanostructures", *Nature Nanotechnology* **4**, 103–107 (2009).

[55] M. Diarra, Y. M. Niquet, C. Delerue, G. Allan, "Ionization energy of donor and acceptor impurities in semiconductor nanowires: Importance of dielectric confinement", *Phys. Rev. B* **75**, 045301 (2007).

[56] P. Xie, Y. Hu, Y. Fang, J. Huang, C. M. Lieber, "Diameter-dependent dopant location in silicon and germanium nanowires", *Proc. Natl. Acad. Sci.* **106**, 15254–15258 (2009).

[57] J. E. Allen, D. E. Allen, E. R. Hemesath, L. J. Lauhon, "Nonuniform Nanowire Doping Profiles Revealed by Quantitative Scanning Photocurrent Microscopy", *Adv. Mater.* **21**, 3067–3072 (2009).

[58] D. E. Perea *et al.*, "Direct measurement of dopant distribution in an individual vapour-liquid-solid nanowire", *Nat. Nanotechnol.* **4**, 315–319 (2009).

[59] R. A. Schlitz, D. E. Perea, J. L. Lensch-Falk, E. R. Hemesath, L. J. Lauhon, "Correlating dopant distributions and electrical properties of boron-doped silicon nanowires", *Appl. Phys. Lett.* **95**, 162101 (2009).

[60] E. Koren, N. Berkovitch, Y. Rosenwaks, "Measurement of Active Dopant Distribution and Diffusion in Individual Silicon Nanowires", *Nano Lett.* **10**, 1163–1167 (2010).

[61] X. Ou *et al.*, "Carrier Profiling of Individual Si Nanowires by Scanning Spreading Resistance Microscopy", *Nano Lett.* **10**, 171–175 (2010).

[62] E. Koren *et al.*, "Obtaining Uniform Dopant Distributions in VLS-Grown Si Nanowires", *Nano Lett.* **11**, 183–187 (2011).

[63] H. W. Wu, C. J. Tsai, L. J. Chen, "Room temperature ferromagnetism in Mn+-implanted Si nanowires", *Appl. Phys. Lett.* **90**, 043121 (2007).

[64] G. Giorgi, X. Cartoixà, A. Sgamellotti, R. Rurali, "Mn-doped silicon nanowires: First-principles calculations", *Phys. Rev. B* **78**, 115327 (2008).

[65] P. Hohenberg, W. Kohn, "Inhomogeneous Electron Gas", *Phys. Rev.* **136**, B864–B871 (1964).

[66] R. Parr, W. Yang, *Density-functional theory of atoms and molecules* (Oxford University Press, 1994).

[67] R. Martin, *Electronic structure: basic theory and practical methods* (Cambridge University Press, 2004).

[68] W. Kohn, L. J. Sham, "Self-Consistent Equations Including Exchange and Correlation Effects", *Phys. Rev.* **140**, A1133–A1138 (1965).

[69] R. M. Nieminen, "Issues in first-principles calculations for defects in semiconductors and oxides", *Modell. Simul. Mater. Sci. Eng.* **17**, 084001 (2009).

[70] M. R. Jarvis, I. D. White, R. W. Godby, M. C. Payne, "Supercell technique for total-energy calculations of finite charged and polar systems", *Phys. Rev. B* **56**, 14972–14978 (1997).

[71] G. Makov, M. C. Payne, "Periodic boundary conditions in *ab initio* calculations", *Phys. Rev. B* **51**, 4014–4022 (1995).

[72] R. Rurali, X. Cartoixà, "Theory of Defects in One-Dimensional Systems: Application to Al-Catalyzed Si Nanowires", *Nano Lett.* **9**, 975–979 (2009).

[73] W. E. Pickett, "Pseudopotential methods in condensed matter applications", *Comput. Phys. Rep.* **9**, 115 –197 (1989).

[74] D. R. Hamann, M. Schlüter, C. Chiang, "Norm-Conserving Pseudopotentials", *Phys. Rev. Lett.* **43**, 1494–1497 (1979).

[75] G. B. Bachelet, D. R. Hamann, M. Schlüter, "Pseudopotentials that work: From H to Pu", *Phys. Rev. B* **26**, 4199–4228 (1982).

[76] N. Troullier, J. L. Martins, "Efficient pseudopotentials for plane-wave calculations", *Phys. Rev. B* **43**, 1993–2006 (1991).

[77] A. M. Rappe, K. M. Rabe, E. Kaxiras, J. D. Joannopoulos, "Optimized pseudopotentials", *Phys. Rev. B* **41**, 1227–1230 (1990).

[78] D. Vanderbilt, "Soft self-consistent pseudopotentials in a generalized eigenvalue formalism", *Phys. Rev. B* **41**, 7892–7895 (1990).

[79] C. G. Van de Walle, P. E. Blöchl, "First-principles calculations of hyperfine parameters", *Phys. Rev. B* **47**, 4244–4255 (1993).

[80] P. E. Blöchl, "Projector augmented-wave method", *Phys. Rev. B* **50**, 17953–17979 (1994).

[81] P. Giannozzi *et al.*, "QUANTUM ESPRESSO: a modular and open-source software project for quantum simulations of materials", *J. Phys.: Condens. Matter* **21**, 395502 (2009), `http://www.quantum-espresso.org`.

[82] J. P. Perdew, K. Burke, M. Ernzerhof, "Generalized Gradient Approximation Made Simple", *Phys. Rev. Lett.* **77**, 3865–3868 (1996).

[83] R. Rurali, M. Palummo, X. Cartoixà, "Convergence study of neutral and charged defect formation energies in Si nanowires", *Phys. Rev. B* **81**, 235304 (2010).

[84] H. J. Monkhorst, J. D. Pack, "Special points for Brillouin-zone integrations", *Phys. Rev. B* **13**, 5188–5192 (1976).

[85] S. Baroni, S. de Gironcoli, A. Dal Corso, P. Giannozzi, "Phonons and related crystal properties from density-functional perturbation theory", *Rev. Mod. Phys.* **73**, 515–562 (2001).

[86] A. K. Singh, V. Kumar, R. Note, Y. Kawazoe, "Effects of Morphology and Doping on the Electronic and Structural Properties of Hydrogenated Silicon Nanowires", *Nano Lett.* **6**, 920–925 (2006).

[87] E. Durgun, N. Akman, C. Ataca, S. Ciraci, "Atomic and electronic structures of doped silicon nanowires: A first-principles study", *Phys. Rev. B* **76**, 245323 (2007).

[88] Y. M. Niquet *et al.*, "Electronic structure of semiconductor nanowires", *Phys. Rev. B* **73**, 165319 (2006).

[89] H. Scheel, S. Reich, C. Thomsen, "Electronic band structure of high-index silicon nanowires", *phys. stat. sol. (b)* **242**, 2474–2479 (2005).

[90] R. Rurali, B. Aradi, T. Frauenheim, A. Gali, "Accurate single-particle determination of the band gap in silicon nanowires", *Phys. Rev. B* **76**, 113303 (2007).

[91] J. X. Cao, X. G. Gong, J. X. Zhong, R. Q. Wu, "Sharp Corners in the Cross Section of Ultrathin Si Nanowires", *Phys. Rev. Lett.* **97**, 136105 (2006).

[92] A. K. Singh, V. Kumar, R. Note, Y. Kawazoe, "Pristine Semiconducting [110] Silicon Nanowires", *Nano Lett.* **5**, 2302–2305 (2005).

[93] C. Delerue, G. Allan, M. Lannoo, "Theoretical aspects of the luminescence of porous silicon", *Phys. Rev. B* **48**, 11024–11036 (1993).

[94] M.-F. Ng, M. B. Sullivan, S. W. Tong, P. Wu, "First-Principles Study of Silicon Nanowire Approaching the Bulk Limit", *Nano Lett.* **11**, 4794–4799 (2011).

[95] J.-A. Yan, L. Yang, M. Y. Chou, "Size and orientation dependence in the electronic properties of silicon nanowires", *Phys. Rev. B* **76**, 115319 (2007).

[96] M. Bruno, M. Palummo, A. Marini, R. Del Sole, S. Ossicini, "From Si Nanowires to Porous Silicon: The Role of Excitonic Effects", *Phys. Rev. Lett.* **98**, 036807 (2007).

[97] T. Vo, A. J. Williamson, G. Galli, "First principles simulations of the structural and electronic properties of silicon nanowires", *Phys. Rev. B* **74**, 045116 (2006).

[98] H. Yoshioka, N. Morioka, J. Suda, T. Kimoto, "Bandgap shift by quantum confinement effect in <100> Si-nanowires derived from threshold-voltage shift of fabricated metal-oxide-semiconductor field effect transistors and theoretical calculations", *J. Appl. Phys.* **109**, 064312 (2011).

[99] I. S. Zevenbergen, T. Gregorkiewicz, C. A. J. Ammerlaan, "Electron-paramagnetic-resonance identification of hydrogen-passivated sulfur centers in silicon", *Phys. Rev. B* **51**, 16746–16749 (1995).

[100] P. T. Huy, C. A. J. Ammerlaan, T. Gregorkiewicz, D. T. Don, "Hydrogen passivation of the selenium double donor in silicon: A study by magnetic resonance", *Phys. Rev. B* **61**, 7448–7458 (2000).

[101] R. Peale, K. Muro, A. Sievers, presented at the Materials Science Forum, vol. 65, pp. 151–156.

[102] G. Roos, G. Pensl, N. M. Johnson, C. Holm, "Hydrogen neutralization and reactivation of chalcogen double-donor centers in silicon", *J. Appl. Phys.* **67**, 1897 –1902 (1990).

[103] Z. N. Liang, L. Niesen, "Evidence for the formation of tellurium-hydrogen complexes in crystalline silicon", *Phys. Rev. B* **51**, 11120–11123 (1995).

[104] J. Coutinho, V. Torres, R. Jones, A. Resende, P. Briddon, "Shallow donor activity of S–H, Se–H, and Te–H complexes in silicon", *phys. stat. sol. (b)* **235**, 107–110 (2003).

[105] J. Coutinho, V. J. B. Torres, R. Jones, P. R. Briddon, "Electrical activity of chalcogen-hydrogen defects in silicon", *Phys. Rev. B* **67**, 035205 (2003).

[106] S. B. Zhang, J. E. Northrup, "Chemical potential dependence of defect formation energies in GaAs: Application to Ga self-diffusion", *Phys. Rev. Lett.* **67**, 2339–2342 (1991).

[107] H. Overhof, M. Scheffler, C. M. Weinert, "Formation energies, electronic structure, and hyperfine fields of chalcogen point defects and defect pairs in silicon", *Phys. Rev. B* **43**, 12494–12506 (1991).

[108] Y. M. Niquet, L. Genovese, C. Delerue, T. Deutsch, "*Ab initio* calculation of the binding energy of impurities in semiconductors: Application to Si nanowires", *Phys. Rev. B* **81**, 161301 (2010).

[109] J. Spaeth, H. Overhof, *Point defects in semiconductors and insulators: determination of atomic and electronic structure from paramagnetic hyperfine interactions* (Springer, 2003).

[110] F. Schwabl, *Quantum mechanics* (Springer, 2007).

[111] S. Blügel, H. Akai, R. Zeller, P. H. Dederichs, "Hyperfine fields of $3d$ and $4d$ impurities in nickel", *Phys. Rev. B* **35**, 3271–3283 (1987).

[112] P. E. Blöchl, "First-principles calculations of defects in oxygen-deficient silica exposed to hydrogen", *Phys. Rev. B* **62**, 6158–6179 (2000).

[113] M. Nielsen, I. Chuang, *Quantum computation and quantum information* (Cambridge University Press, 2000).

[114] D. P. DiVincenzo, "The Physical Implementation of Quantum Computation", *Fortschr. Phys.* **48**, 771–783 (2000).

[115] T. D. Ladd *et al.*, "Quantum computers", *Nature* **464**, 45–53 (2010).

[116] B. E. Kane, "A silicon-based nuclear spin quantum computer", *Nature* **393**, 133–137 (1998).

[117] G. P. Berman, G. D. Doolen, P. C. Hammel, V. I. Tsifrinovich, "Solid-state nuclear-spin quantum computer based on magnetic resonance force microscopy", *Phys. Rev. B* **61**, 14694–14699 (2000).

[118] G. P. Berman, G. D. Doolen, P. C. Hammel, V. I. Tsifrinovich, "Magnetic Resonance Force Microscopy Quantum Computer with Tellurium Donors in Silicon", *Phys. Rev. Lett.* **86**, 2894–2896 (2001).

[119] G. W. Ludwig, "Paramagnetic Resonance Study of a Deep Donor in Silicon", *Phys. Rev.* **137**, A1520–A1530 (1965).

[120] S Gruelich-Weber, J. R. Niklas, J. M. Spaeth, "ENDOR investigation of Se^+ in silicon", *J. Phys. C* **17**, L911 (1984).

[121] G. Feher, "Electron Spin Resonance Experiments on Donors in Silicon. I. Electronic Structure of Donors by the Electron Nuclear Double Resonance Technique", *Phys. Rev.* **114**, 1219–1244 (1959).

[122] M. Belli, M. Fanciulli, N. V. Abrosimov, "Pulse electron spin resonance investigation of bismuth-doped silicon: Relaxation and electron spin echo envelope modulation", *Phys. Rev. B* **83**, 235204 (2011).

[123] J. Song, S. Y. Ren, J. D. Dow, "Size effect on chalcogen deep levels in Si quantum dots", *Phys. Rev. B* **59**, 2045–2049 (1999).

[124] R. Rurali, B. Aradi, T. Frauenheim, A. Gali, "Donor levels in Si nanowires determined by hybrid-functional calculations", *Phys. Rev. B* **79**, 115303 (2009).

[125] D. V. Melnikov, J. R. Chelikowsky, "Quantum Confinement in Phosphorus-Doped Silicon Nanocrystals", *Phys. Rev. Lett.* **92**, 046802 (2004).

[126] A. Debernardi, M. Fanciulli, "Confinement effect in P doped spherical Si nanocrystals", *Solid State Sci.* **11**, E-MRS symposium N and R, 961 –964 (2009).

[127] A. Debernardi, M. Fanciulli, "Stark effect of confined shallow levels in phosphorus-doped silicon nanocrystals", *Phys. Rev. B* **81**, 195302 (2010).

[128] P. W. Leu, A. Svizhenko, K. Cho, "*Ab initio* calculations of the mechanical and electronic properties of strained Si nanowires", *Phys. Rev. B* **77**, 235305 (2008).

[129] K.-H. Hong, J. Kim, S.-H. Lee, J. K. Shin, "Strain-Driven Electronic Band Structure Modulation of Si Nanowires", *Nano Lett.* **8**, 1335–1340 (2008).

[130] D. K. Wilson, G. Feher, "Electron Spin Resonance Experiments on Donors in Silicon. III. Investigation of Excited States by the Application of Uniaxial Stress and Their Importance in Relaxation Processes", *Phys. Rev.* **124**, 1068–1083 (1961).

[131] H. Huebl *et al.*, "Phosphorus Donors in Highly Strained Silicon", *Phys. Rev. Lett.* **97**, 166402 (2006).

[132] L. Dreher *et al.*, "Electroelastic Hyperfine Tuning of Phosphorus Donors in Silicon", *Phys. Rev. Lett.* **106**, 037601 (2011).

[133] M Leslie, N. J. Gillan, "The energy and elastic dipole tensor of defects in ionic crystals calculated by the supercell method", *J. Phys. C* **18**, 973 (1985).

[134] M. Amato, S. Ossicini, R. Rurali, "Band-Offset Driven Efficiency of the Doping of SiGe Core–Shell Nanowires", *Nano Lett.* **11**, 594–598 (2011).

List of publications derived from the Ph.D. work

1. G. Petretto, A. Debernardi, M. Fanciulli "Confinement Effects and Hyperfine Structure in Se Doped Silicon Nanowires", *Nano Letters*, **11**, *4509*, doi 10.1021/nl202803n

2. G. Petretto, A. Debernardi, M. Fanciulli "Electronic properties of pristine and Se doped [001] silicon nanowires: an ab initio study", *Journal of nanoscience and nanotechnology*, in press

Acknowledgements

I would like to express my gratitude to all the people who have contributed to the completion of this thesis in different ways.

I am heartily thankful to Prof. Marco Fanciulli and Alberto Debernardi for giving me the opportunity to work on this project. They have introduced me to this field of research and they have supported and guided me in my PhD activities.

Working at the MDM laboratory has been a stimulating experience and for this I have to thank all the present and former members of the group. In particular I am grateful to Enrico Prati, Matteo Belli and Marco Demichielis for their collaboration and for letting me use their PC every time they could. A special thanks goes to Antonio Vellei for giving me a small taste of laboratory life.

Last, but not least, I would like to thank my family and all my friends that have helped me in the choice of undertaking the PhD experience and for being a constant support during these years. I won't name them one by one, in order not to miss any.

Milano, January 26th 2012 Guido Petretto